Progress in Materials Science 132 (2023) 101046

Contents lists available at ScienceDirect

Progress in Materials Science

journal homepage: www.elsevier.com/locate/pmatsci

Are lead-free relaxor ferroelectric materials the most promising candidates for energy storage capacitors?

A.R. Jayakrishnan [a,b], J.P.B. Silva [c,d,*], K. Kamakshi [e], D. Dastan [f], V. Annapureddy [g,h], M. Pereira [c,d], K.C. Sekhar [a,*]

[a] Department of Physics, School of Basic and Applied Science, Central University of Tamil Nadu, Thiruvarur 610 005, India
[b] Center for Nanoscience and Engineering, Indian Institute of Science, Bangalore, Karnataka 560012, India
[c] Physics Center of Minho and Porto Universities (CF-UM-UP), University of Minho, Campus de Gualtar, 4710-057 Braga, Portugal
[d] Laboratory of Physics for Materials and Emergent Technologies, LapMET, University of Minho, 4710-057 Braga, Portugal
[e] Department of Science and Humanities, Indian Institute of Information Technology Tiruchirappalli, Tiruchirappalli 620 015, Tamil Nadu, India
[f] Department of Materials Science and Engineering, Cornell University, Ithaca, NY 14850, USA
[g] Department of Physics, National Institute of Technology Tiruchirappalli, Tiruchirappalli 620 015 Tamil Nadu, India
[h] Center for Energy Harvesting and Storage Technology, National Institute of Technology, Tiruchirappalli, Tiruchirappalli, Tamil Nadu 620015, India

ARTICLE INFO

Keywords:
Relaxor ferroelectrics
Energy storage capacitors
Pulsed power technology
Lead-free ferroelectrics
Recoverable energy density

ABSTRACT

Dielectric capacitors offer high-power density and ultrafast discharging times as compared to electrochemical capacitors and batteries, making them potential candidates for pulsed power technologies (PPT). However, low energy density in different dielectric materials such as linear dielectrics (LDs), ferroelectrics (FEs), and anti-ferroelectric (AFEs) owing to their low polarization, large hysteresis loss and low breakdown strength, respectively, limits their real time applications. Thus, achieving a material with high dielectric constant, large dielectric breakdown strength and slim hysteresis is imperative to obtain superior energy performance. In this context, relaxor ferroelectrics (RFEs) emerged as the most promising solution for energy storage capacitors. This review starts with a brief introduction of different energy storage devices and current advances of dielectric capacitors in PPT. The latest developments on lead-free RFEs including bismuth alkali titanate based, barium titanate based, alkaline niobite based perovskites both in ceramics and thin films are comprehensively discussed. Further, we highlight the different strategies used to enhance their energy storage performance to meet the requirements of the energy storage world. We also provide future guidelines in this field and therefore, this article opens a window for the current advancement in the energy storage properties of RFEs in a systematic way.

1. Introduction

Many researchers pay special attention on the sustainable energy, electrification of vehicles, and military systems in order to reduce the energy deficiency and global air pollutions. This led to the necessity of developing various energy generation and storage technologies [1–3]. However, the usage of electricity from the renewable energy paved the evolution of different energy storage devices. This includes dielectric capacitors, electrochemical capacitors, and batteries. Based on the energy storage mechanism and the

* Corresponding authors.
E-mail addresses: josesilva@fisica.uminho.pt (J.P.B. Silva), koppolechandrasekhar@cutn.ac.in (K.C. Sekhar).

https://doi.org/10.1016/j.pmatsci.2022.101046
Received 5 June 2020; Received in revised form 26 April 2022; Accepted 9 November 2022
Available online 21 November 2022

movement of charges, there is a significant difference in the energy storage density, power density and the charge–discharge time in these devices. The Ragone plot shown in Fig. 1 displays the energy storage density versus power density of these energy storage devices [4]. Due to the slow movement of charges, batteries have a high energy density but a poor power density. Hence, they are implemented for long-term applications [4]. On the other hand, the capacitors are considered as short-term devices with a low energy density and a high-power density. Capacitors have fast charging/discharging capability than the batteries [5,6]. The batteries and the electrochemical capacitors work on the principle of liquid electrolyte and chemical reactions, respectively. Despite, the batteries are mainly used for the long-term and stable energy supplies [4,7,8], they cannot be considered for high voltage applications (maximum voltage up to 5 V) due to the decomposition of electrolyte at higher voltages [8]. Even though, the electrochemical capacitors possess moderate energy density together with an improved power density, they are hampered by a slow charge–discharge process (range of seconds) and a low operating voltage (<3 V) [9,10]. On the other hand, the dielectric capacitor is a simple passive component consisting of an insulating material placed between two parallel conducting plates. The electric field induces an electrostatic displacement and it can be stored as electrical energy in the dielectric capacitor. Thus, capacitors are receiving greater attention owing to their low cost and high operating voltages, which make them suitable candidates for large-scale applications starting from basic consumer electronic devices to advanced pulsed power technology (PPT). Moreover, the PPT demands higher operating voltages, typically in the order of 100 kV, in space shuttle power systems, advanced aeroplanes, electromagnetic armor, etc [11]. Unlike the batteries and electrochemical capacitors, the dielectric capacitors can be operated for longer duration under higher voltages (MV range). In fact, the dielectric capacitors exhibit superior thermal stability (up to 250 ^{0}C), which is essential for electric vehicles, drilling head machineries in oil well, and aircraft engines for delivering power at high temperatures [12–14]. Most importantly, the inherent ability of the dielectric capacitors to intake energy quickly and deliver it within a short period of time (micro to nano second range) make them promising contender for energy storage applications in PPTs [15].

Currently, the dielectric capacitors have been expanded their role in many power conditioning and pulsed-discharge electronic applications, as shown in Fig. 2. For instance, the dielectric capacitors are critical components in hybrid electric vehicles (HEVs). In HEVs, a power electronic circuit is used to convert the DC input from the battery to an AC output for operating the electric motor as shown in the Fig. 3 [16,17]. Here, the DC bus capacitor (C_E) is responsible for storing energy, discharging and voltage smoothing. The snubber capacitor (C_C) reduces the power dissipation in a solid-state inverter and the filter capacitor (C_R and C_F) removes undesirable frequencies and harmonics from the output AC signal [17]. The present dielectric capacitors used in commercial applications are based on bulky biaxially oriented polypropylene (BOPP) [18–20]. It has a low energy storage density (ESD) < 7 J/cm^3 and a large volume [20]. Moreover, the power circuit of HEV requires an additional cooling system due to the low operating temperature of BOPP. For example, the working temperature of the power system in Toyota PriusR HEV is ~140 ^{0}C [19]. However, the maximum operating temperature of the BOPP used in Toyota PriusR HEV is ~ 90 ^{0}C. Such a mismatch in the temperature demands a secondary cooling system in addition to the engine radiator. This secondary cooling system working at ~ 65 ^{0}C compensate the working temperature and provide a stable operation of the inverter. As a consequence, the power system design becomes more complicated with an extra weight and volume. This is unfavorable in terms of performance-wise as well as financial-wise for the production of the HEVs [19,20]. Therefore, it has become a necessity to look for alternative materials that comprise high energy storage density, good temperature stability and less volume occupancy [17].

The dielectric capacitors are being also used in combat hybrid power systems (CHPS) for advanced armored vehicles. The CHPS comprise two energy sources: (i) a prime power source such as heat engine for driving an AC generator and (ii) an energy storage system consisting of advanced batteries, capacitors, and flywheels or a combination of all of them [21–23]. Fig. 4 displays the power flow diagram of the CHPS developed by the Defense Advanced Research Projects Agency (DARPA) in the year of 1997 for the advanced combat vehicles [23].

Generally, the capacitors play a key role in the pulse forming network (PFN) of the CHPS for generating an exceptionally high-

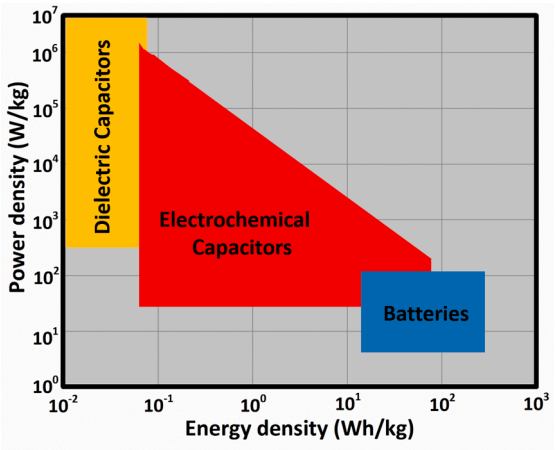

Fig. 1. Comparison of power density as a function of energy storage density in various energy storage devices [4].

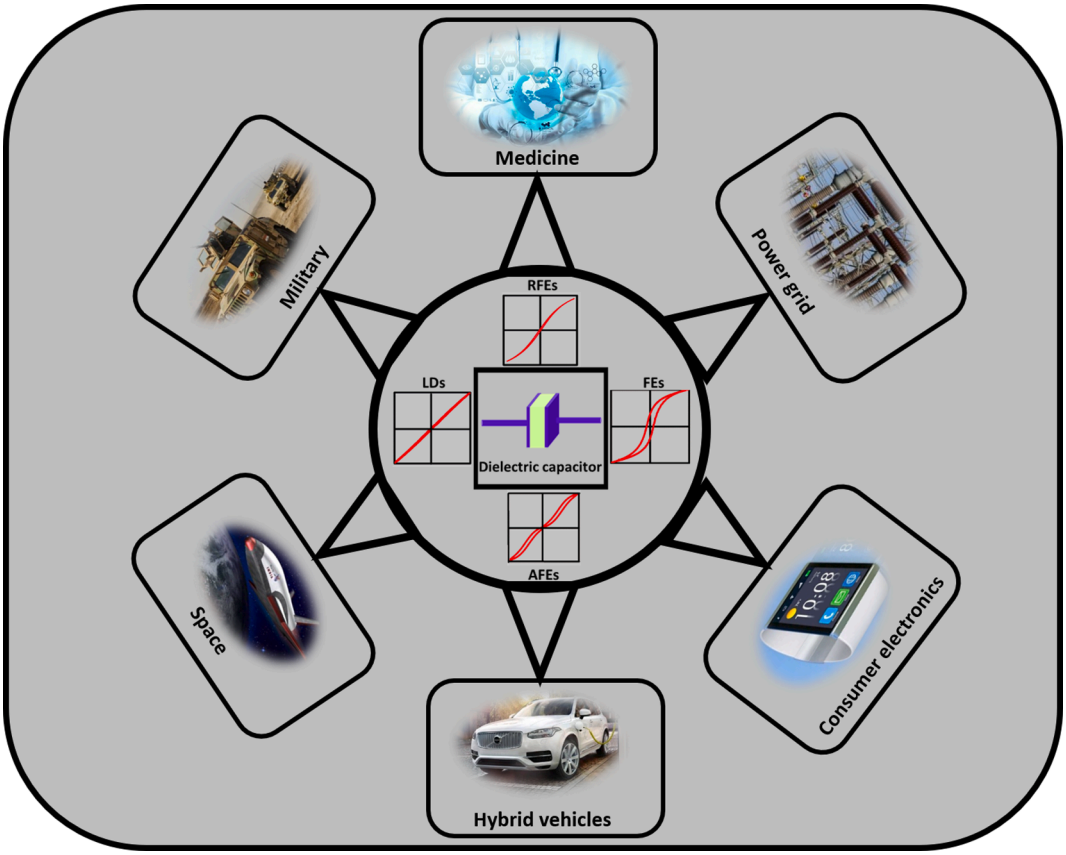

Fig. 2. Applications of dielectric capacitors in various pulsed power technologies.

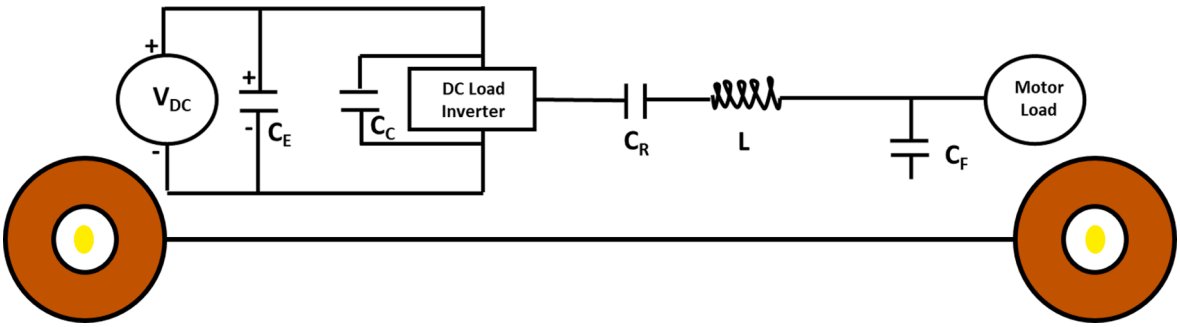

Fig. 3. Schematics of a power electronic system used in a hybrid electric vehicle. [17].

power density for their smooth operations. For instance, the US Army aimed at developing BOPP capacitors for combat vehicles for better service, higher power, and lower mass of the equipment that ground troops carry [20]. Further, the BOPP capacitors used in the PFN have an energy density of 1.2 J/cm^3 [21]. Currently, the US Army was able to improve the energy storage density of BOPP to 3 J/cm^3. Instead, the PPT demand materials that can provide a good thermal stability in the range from 125 to 180 ^{0}C [22]. However, the commercially available BOPP capacitor possesses an energy storage density of 6.2 J/cm^3 and a maximum working temperature of 90 ^{0}C [22]. Beyond that temperature, the lifetime of the BOPP capacitors degrades rapidly due to decrease in the ripple current handing capability [20].

The dielectric materials used in capacitors can be classified into linear dielectrics (LDs), ferroelectric (FEs), anti-ferroelectric (AFEs), and relaxor ferroelectric (RFEs) materials. These materials are categorized based on their electric field dependent polarization behavior and dielectric permittivity. Fig. 5 (a)-(d) illustrate the schematics of the polarization–electric field (*P-E*) loop and the ferroelectric domain structure with dipole orientation for the different dielectric materials.

In linear dielectrics, the dielectric permittivity is almost constant and, as a consequence, the polarization obeys a linear relation

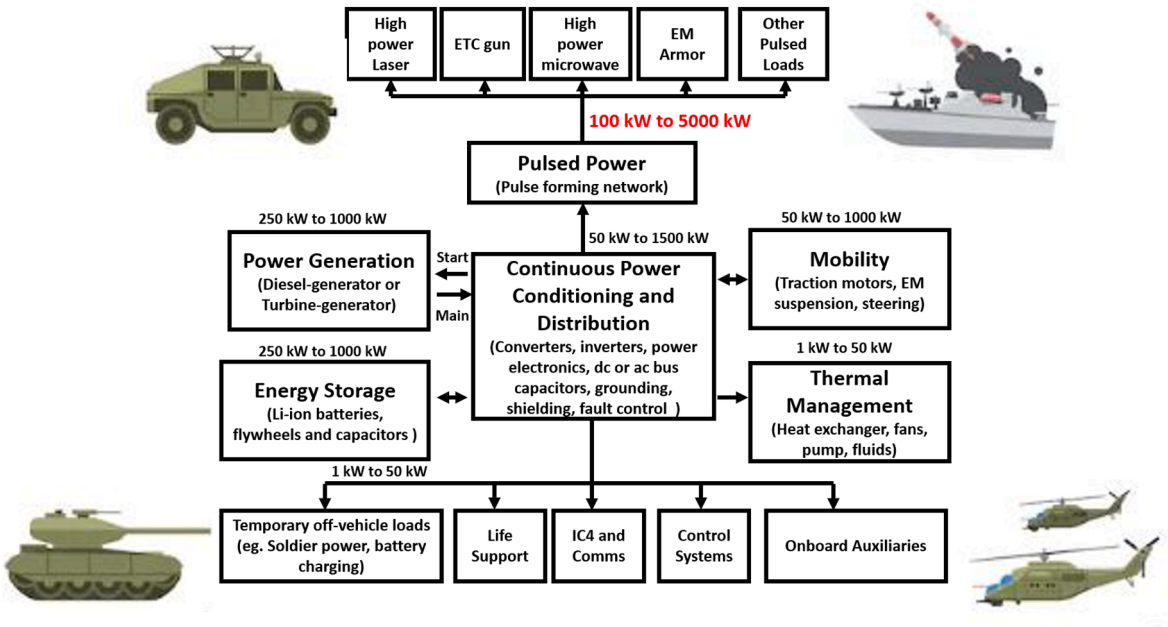

Fig. 4. Power flow diagrams of the combat hybrid power systems in advanced combat vehicles. [21,23].

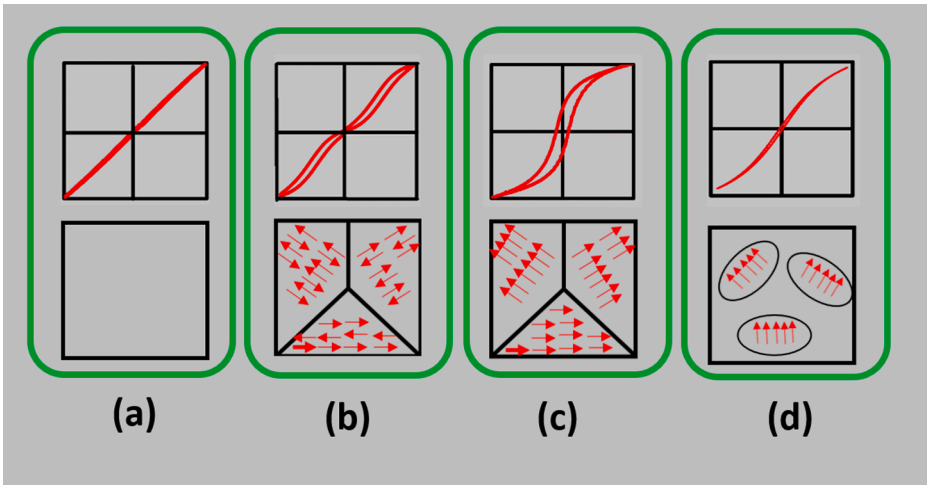

Fig. 5. Schematic representation of typical polarization behavior (top panel) and the ferroelectric domain structure with dipole orientation (bottom panel) in (a) LDs, (b) AFEs, (c) FEs, and RFEs.

with respect to the applied electric field, which is attributed to the lack of permanent dipole moment. Even though the linear dielectric materials own higher breakdown strength and low energy loss, their low value of polarization makes them inappropriate for the energy storage capacitors [24–28]. The use of anti-ferroelectric materials in energy storage capacitors is tremendously explored. However, the AFEs suffer from large hysteresis loss and smaller energy storage density caused by the anti-ferroelectric-ferroelectric phase transitions. Moreover, the anti-ferroelectric materials are mostly lead-based, which cause serious harm to both environment and human beings. Hence, the anti-ferroelectric materials are limited in practical applications [25–28]. Ferroelectric materials exhibit superior polarization values even without an external electric field. This is attributed to the presence of a net dipole moment. Therefore, the dielectric permittivity is expected to have a nonlinear relation with the applied electric field. Still, the FEs suffer a low dielectric breakdown strength followed by a smaller energy storage density owing to their large remnant polarization, hysteresis loss, and high dielectric loss [28–31]. On the other hand, the relaxor ferroelectric (RFEs) materials are receiving greater attention in the energy storage field of research owing to their suitable dielectric properties and ferroelectric properties. RFEs exhibit a large dielectric permittivity and saturation polarization, and are characterized by low remnant polarization and slim *P-E* loops [32]. These features are essential for accomplishing excellent energy storage performance. Therefore, it is necessary to explore and systematize the energy

storage properties of RFEs since they are becoming a hot topic among the researchers in the current scenario.

Most of the review articles discuss the different dielectric materials, such as LDs, AFEs, FEs, and RFEs, as energy storage capacitors and their applications in pulsed power technology, without detailing the different strategies implemented to enhance the energy storage performance of each of them [4,33–38]. In this context, we aim to present a comprehensive and detailed summary on the investigations developed in RFE based energy storage systems, since, as discussed above, they have unique advantages. We focused on the different Pb-free RFE bulk ceramics, as well as thin films. This review started with a brief introduction about the different energy storage devices and the current advances of dielectric capacitors in the pulsed power applications. Then, the different methods used for assessing the energy storage performance of the capacitors and the key factors determining their performance are summarized. The origin of RFEs and the different RFE systems, both in the bulk and thin film form, are then discussed. This review covers the newly introduced most promising Pb-free RFE systems and presents a discussion on the different RFE based dielectric ceramic systems. Further, recent strategies adopted for tailoring and enhancing the energy storage properties of the RFEs systems are highlighted.

2. Energy storage performance assessment

The energy storage density of a dielectric capacitor can be evaluated by two different methods such as dynamic and static methods as described below.

2.1. Dynamic method

The performance of energy storage in a dielectric capacitor is determined using the parameters such as the dielectric permittivity (ε_r), polarization (P), and applied electric field (E).

The energy storage density of a LD with insignificant energy loss is given by [39]:

$$W = \frac{1}{2}\varepsilon_0\varepsilon_r E^2 \tag{1}$$

where ε_0 is the permittivity of free space. On the other hand, the nonlinear dielectric materials like FEs, AFEs, and RFEs possess certain energy losses during a hysteresis loop. Therefore, the recoverable energy density for such materials is evaluated from the polarization–electric field (P-E) loops obtained using Sawyer Tower circuit (Fig. 6 (a)) as follows [40–43]:

$$W = \int_0^{P_m} EdP(\text{Charging})$$

$$W_r = \int_{P_r}^{P_m} EdP(\text{Discharging})$$

where the terms W, W_r, P_r, and P_m represents the charge energy density, recoverable energy density, remnant polarization, and maximum polarization, respectively. However, during the depolarization process some portion of the energy in these materials is dissipated in the form of hysteresis loss. Therefore, the energy storage efficiency (η) of LDs, FEs, AFEs, and RFEs is a function of both discharge energy density and the energy loss (W_l):

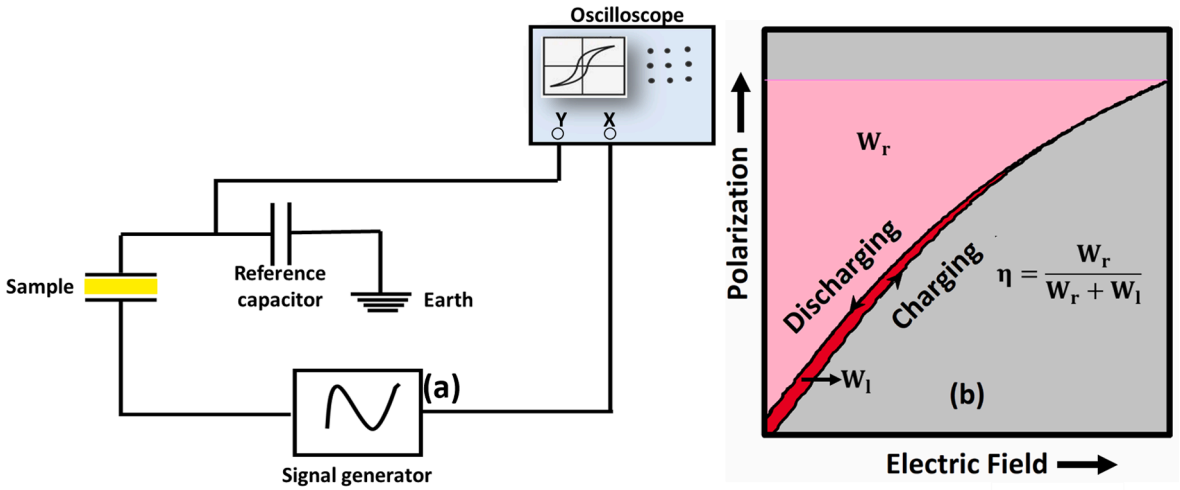

Fig. 6. (a) Schematic circuit of the Sawyer-Tower circuit for measuring the P-E characteristics; (b) diagram showing the evaluation of energy storage properties.

$$\eta = \frac{W_r}{W_r + W_l} \tag{4}$$

The schematic representation of the energy storage calculation from the *P-E* loop is illustrated in Fig. 6 (b).

2.2. Static method

The schematic diagram of the static method is shown in Fig. 7. It consists of an external bias, load resistance (R_L), high voltage charge–discharge pulse switch, and the sample capacitor to determine the energy storage density. The charge–discharge switch plays switching role to complete the circuit. At first, the sample capacitor is charged by the external bias. Then, a part of energy is discharged through the load resistance R_L, followed by the transient current developed in the circuit. This current wave form is recorded using an oscilloscope and W_r as a function of time can be evaluated using the formula [4,44]:

$$W_r = \int i^2 R_L dt \tag{5}$$

where R_L and t represents the load resistance and discharge time, respectively. The ratio between the amount of stored energy to the volume of the capacitor gives the recoverable energy (W_r). Usually, the W_r value obtained using the static method is lower than the value estimated using the dynamic method from the *P-E* loops [36,45] because the frequencies used in both methods are different. In general, the static method uses an ultrahigh frequency (MHz) whereas the *P-E* loop is measured at lower frequency (few hundred Hz) [36].

3. Key factors determining the energy storage performance

From the equations (1)-(4) and the Fig. 6(b), it is evident that the dielectric permittivity, the $\Delta P = (P_m - P_r)$ value, and the dielectric breakdown strength (E_B) plays the crucial part in determining the dielectric capacitor's energy storage performance. This section discusses the impact of each parameter in the energy storage performance.

3.1. Polarization change ($\Delta P = P_m - P_r$) factor

The energy storage performance of a dielectric capacitor is intrinsically linked to the *P-E* loop shape, since the area under the graph give the recoverable energy density (Fig. 6). Therefore, the energy storage density is strongly reliant on the ΔP value, which is equal to the P_m and P_r difference, as the W_r is directly proportional to the ΔP value [43,46]. However, the energy loss in a dielectric material is directly related to the overall performance of the dielectric capacitor [47,48]. The energy dissipated in the form of hysteresis loss leads to the heat generation in the capacitor and consequently, deteriorates the thermal stability and the life-time of the capacitor. Besides, the polarization hysteresis loss is mainly attributed to two factors namely the dielectric loss ($tan\delta$) and the corresponding temperature

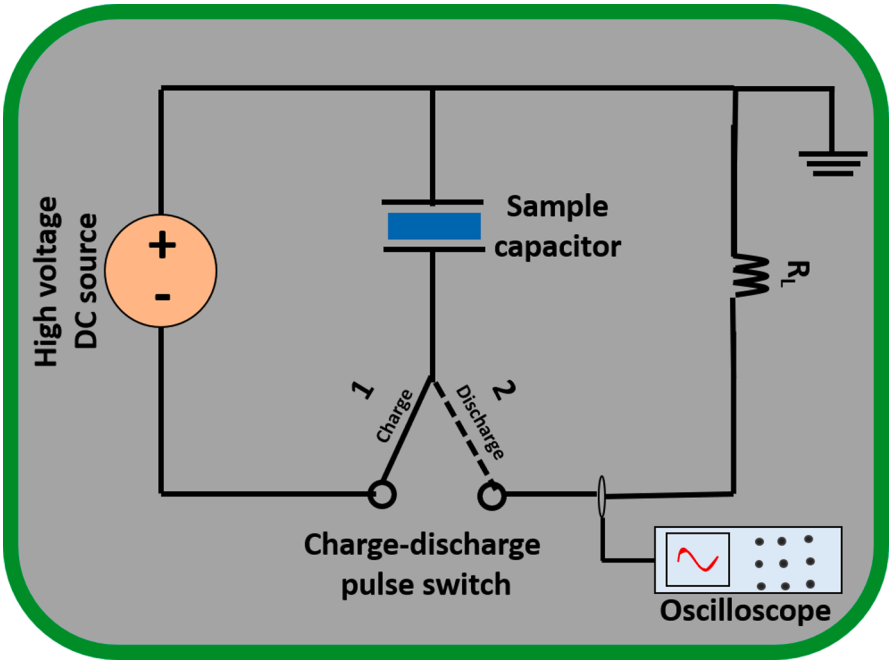

Fig. 7. Circuit for measuring the energy storage density [4].

rise (ΔT). This can be expressed as [47,48]:

$$W_l = \frac{1}{2}\varepsilon_0\varepsilon_r E^2 tan\delta \tag{6}$$

$$\Delta T = \frac{fV_e}{hA}W_l \tag{7}$$

here, f, V_e, A, and h denotes the driving frequency, effective area corresponding to the applied electric field, sample surface area, and heat transfer coefficient, respectively [48]. Therefore, it is essential for a dielectric material to have low $tan\delta$ value, low P_r, and high P_m for achieving superior energy storage efficiency. Furthermore, the real-world applications require the capacitors having high energy storage efficiency with less wastage of heat, better reliability, and longer life-time.

3.2. Dielectric breakdown strength (E_B)

The dielectric breakdown strength (E_B) is another factor that impacts on the energy storage performance, since W_r is proportional to E as per the equations (1–3) [49]. The maximum electric field above which the electrical resistance of a dielectric material drastically reduced is termed as the dielectric breakdown strength. There are several intrinsic and extrinsic factors which strongly affect the dielectric breakdown strength. The intrinsic factors include the grain size, crystal structure, defect chemistry, microstructural uniformity, porosity, etc. whereas the various extrinsic factors are electrode configuration, working parameters and environmental conditions [50–54]. Therefore, the fabrication of a high-quality energy storage capacitor is influenced by the dense microstructures for achieving a superior capacitance under a very high electric field. However, the weak points in a dielectric that are responsible for the dielectric breakdown are pores, cracks and even compositional inhomogeneity [53–55]. For instance, the porosity appears to be a dominant factor that affects the E_B of a dielectric material. These pores can create overheat and thermal stress in the ceramics and a consequent electric breakdown of the ceramics occurred at higher electric fields [53,54].

More importantly, the E_B of a dielectric material can be closely related to the mechanical strength of the material. The failure happens at the frail points of the material being tested, in both situations [17]. For this reason, it is possible to explain both electrical and mechanical failure using a statistical distribution of flaws. Several researchers established that there exist some similarities in the statistical distribution of both electrical and mechanical failure [17] and the Weibull distribution was commonly used to estimate the E_B for a dielectric capacitor [56,57]. This distribution makes use of a Weibull plot with an average number of samples (minimum 8–10), which are used for breakdown calculations [57]. The following equations can be used to describe the Weibull distribution:

$$X_i = \ln(E_i) \tag{8}$$

$$Y_i = \ln(-\ln\left(1 - \frac{i}{n}\right)) \tag{9}$$

Here, X_i and Y_i are the parameters of the Weibull distribution function, E_i is the breakdown voltage of the i^{th} sample, n is the total number of samples, and i is the rank of samples. The x-intercept from the linear relationship between X_i and Y_i gives the magnitude of E_B. Further, there are two empirical parameters (α, β) known as the Weibull function that determine the probability of dielectric failure and are calculated using the relations [58]:

$$F(E) = 1 - \exp[1 - \frac{E}{\alpha}]^{\beta} \tag{10}$$

where $F(E)$ represents the cumulative probability of failure for field up to E, α is the scale parameter and β is the Weibull modulus (the slope from Weibull plots) [57,58]. The parameter α determines the magnitude of the E_B and the shape parameter β determines the range of E_B [58].

3.3. Discharge time ($\tau_{0.90}$)

The discharge time is an important parameter to access the performance of capacitors in PPTs. The PPTs require capacitors that can store energy for relatively long period of time and release it as a high-power pulse over a short period of time in the form of high voltage and current. An RC circuit as shown in Fig. 7 is used to measure the $\tau_{0.90}$ and W_r. The W_r is determined through a load resistor (R_L) connected directly with the dielectric capacitor as shown in Fig. 7. Firstly, the charge–discharge pulse switch is turned "1″ to make the ceramic capacitor get charged. Afterwards, the switch is turned "2" and the ceramic capacitor will discharge. Then, a coil connected to an oscilloscope is used to obtain the voltage that can be converted into discharge current waves. Lastly, the electric current (i) as a function of time (t) is obtained. Thus, the W_r can be calculated as [59,60]:

$$W_r(t) = \frac{R_L \int i^2(t)dt}{v} \tag{11}$$

where $i(t)$, R_L, and v are the current, load resistance, and the volume of the ceramic sample, respectively. The equation (11) can be rewritten in terms of $V(t)$ and i(t) as:

$$W_r(t) = \frac{1}{v}\int_0^t V(t)i(t)dt \tag{12}$$

During the discharging, the voltage $V(t)$ on a capacitor is being discharged through the load resistor R_L, which follows an exponential decay (universal time constant formula) and is found to be:

$$V(t) = V_0 e^{\frac{-t}{\tau}} \tag{13}$$

where V_0 is the maximum applied voltage and $\tau = R_L C$ is the relaxation time.
On substitution of equation (13) in equation (12), followed by the integration and solving gives:

$$W_r(t) = \frac{\tau V_0^2}{2vR_L}[1 - e^{\frac{-2t}{\tau}}]$$

The experimental discharge time $\tau_{0.9}$ determines the discharging speed of a capacitor and is defined as the time required to discharge 90 % of stored energy in a capacitor. The value of $\tau_{0.9}$ is 0.15 μs at an infinite long time (as $t \to \infty$) [59,60]. The discharging time of a capacitor is influenced by the dielectric permittivity of the materials, thickness ($V = E/d$) of the capacitor, the load resistance and applied voltage [33]. Also, the application of energy storage capacitors in pulsed power technology requires a very short discharge time with an excellent W_r.

4. Relaxor ferroelectric systems (RFEs)

In recent years, most of the researchers on the energy storage capacitors are particularly concentrated in developing devices for PPT. The PPT demands capacitors that can provide immense energy in a short period of time. This requires a material that possesses excellent energy storage density, superior energy storage efficiency, high breakdown strength and an ultrafast discharging speed. From this point of view, the RFE materials are receiving greater attention in the energy storage capacitor fabrications owing to their excellent dielectric and ferroelectric properties. Besides, the RFEs are characterized by lower remnant polarization, slim *P-E* loops and faster discharging capability. Hence, these RFEs can be considered as an ideal candidate for the energy storage capacitor applications.

4.1. Brief history and mechanism of relaxor ferroelectricity

The RFE are considered as separate class of materials due to their abnormal behavior in dielectric, piezoelectric and ferroelectric properties compared to FE materials. The first relaxor behavior was observed in the FE ABO_3 perovskite systems developed by G. S. Smolenskii et al., namely $Pb(Mg_{1/3}Nb_{2/3})O_3$ (PMN) and $Pb(Sc_{1/2}Ta_{1/2})O_3$ (PST) systems [61]. The relaxor behavior was successfully introduced in most fascinating FE material such as $PbZr_{0.52}Ti_{0.48}$ by doping with different elements in both A and B-sites. The modified PZT materials are considered as a special group of FE materials, the so-called RFE after name was made familiar by L. E. Cross in 1987 [62]. He suggested that a material can be considered as RFE if it satisfies three important features such as (i) broad temperature-dependent dielectric permittivity i. e a diffused phase transition from ferroelectric to paraelectric state (ii) frequency dependence of dielectric maximum temperature (T_m) i. e the occurrence of dielectric relaxation and (iii) absence of macroscopic symmetry breaking in the vicinity of T_m.

RFEs are widely investigated for various applications, but its mechanism is scarcely understood so far. Several models based on the concept of polar nano regions (PNR) were proposed to explain the origin of relaxor behavior. First, Smolenskii proposed a 'compositional heterogeneity model', in which compositional fluctuations exists up to a nanometer scale and are responsible for diffused phase transitions. N. Setter et al., experimentally verified the compositional heterogeneity model by studying B-site cation disorder on diffused phase transitions in PST systems [63]. Further, L.E. Cross extended the Smolenskii's theory to a 'super paraelectric' model, where the relaxor behavior is attributed to thermally activated ensemble of super paraelectric clusters [62] and the PNRs are highly dynamic in vicinity of T_m. On the other hand, Viehland et al., proposed the 'dipolar glass model' in which coupling between super paraelectric clusters in relaxors leads to freezing behavior like in polar glass systems and freezes polarization fluctuations [64]. Later, H. Qian and L.A. Bursill et al., proposed a 'random field Potts model' by taken into the account of nanoscale distribution of charged chemical defects and nano-domain textures on formation and dynamics of nano scale polar clusters [65]. A. E. Glazounova and A. K. Tagantsev in 1999, proposed a 'breathing model' to explain the relaxor behavior in terms of PNR's interface boundary and nonpolar matrix [66]. The more details, merits and limitations of different models to predict the relaxor behavior can be found in different reviews on RFE [67–75].

The understanding of PNRs microstructure and their dynamics is crucial to enhance the relaxor behavior. The long-range dipole–dipole interaction based FE theories failed to explain nucleation of PNRs and origin of short-range polarization typically from zero to few nanometers [74–76]. The temperature dependent dielectric permittivity plays a crucial role in exploring the dynamics of PNR. At a certain temperature below Curie temperature (T_c), known as Burns' temperature (T_D), the temperature-dependent dielectric maximum deviates from the Curie-Weiss law. At this temperature, the nucleation of PNRs situated throughout the grains get stimulated and thereby, uplift the broad dispersive behavior of the T_m. Further, decline of temperature below T_D initiates more PNR interaction leading to a freezing process resulting in a non-ergodic FE state. This temperature at which the ergodic behavior vanishes or the freezing of PNRs takes place is known as freezing temperature (T_f). i. e above T_f the behavior is ergodic, while below T_f, a non-ergodic relaxor behavior [75,76]. Polinger *et al.*, further elucidated the existence of the non-ergodic ferroelectric state in ABO_3 perovskites using pseudo-Jahn-Teller (PJT) theory [77]. In non-ergodic state, the relaxation times of PNRs diverge and moreover, a permanent

long-range order can be induced in non-ergodic relaxors by application of electric field. Thus, they are similar to conventional ferroelectrics polarization and strain as a function of electric field. Further, the electric field induced long-range order is distrusted when they are heated to a temperature above T_f and thus it is transformed to the state of ergodic accompanied by anomaly in complex dielectric permittivity. Besides, the presence of a depolarization temperature (T_d) is also well-reflected in the thermal evolution of polarization hysteresis loops. The T_f and T_d are considered as same so far in canonical relaxors such as $Pb_{1-x}La_x)(Zr_{1-y}Ty)_{1-x/4}O_3$ (PLZT) and $(Mg_{1/3}Nb_{2/3})O_3$ (PMN) [78–80]. However, recent experimental studies suggest that T_f and T_d are not the same [75]. Therefore, the study of switching dynamics of PNRs under the electric field and temperature are important for the complete understanding of the materials properties.

In addition to theoretical studies on RFEs, great attention has been paid by experimental/application-oriented community due to large dielectric permittivity and high piezoelectric coefficients. Recently, relaxor materials are extensively considered for energy storage capacitors since they possess a sufficiently large P-E loop with relatively low hysteresis loss as compared to FEs [32–34]. This is due to the fact that the PNRs can be oriented with the applied electric field resulting in a large polarization. But once the field is removed, the PNRs swiftly reacquire their random orientation resulting in a low Pr. Subsequently; a slimmer P-E loop with large saturation polarization is expected [34]. A more detailed understanding of the properties of RFEs that differentiate them from the FEs is shown in Fig. 8. Due to the aforementioned differences between RFEs and FEs and its potential advantages for different applications especially for PPT, the RFEs systems are being tremendously studied in the last 30 years. Fig. 9 reveals that from 90′s, the research on RFEs increases exponentially until the beginning of the 21st century and then, the number of publications per year remained almost constant up to 2010. After that, again these materials have been the subject of renewed interest. For comparison, the number of publications per year related to RFEs based energy storage capacitors is also included. It is evident that the exponential increase in the number of publications per year in the last decade in RFEs is due to the potential application of these materials as energy storage systems.

4.2. Different Pb-free relaxor ferroelectric ceramics for energy storage capacitor fabrication

Even though the first relaxor ferroelectric material reported 40 years ago, RFEs received a revival in the beginning of 2000 as energy storage capacitor in sustainable energy storage technology [81]. The first RFE based energy storage capacitor was a Pb based ceramic powder $(Pb(Mg_{1/3}Nb_{2/3})O_3$-$PbTiO_3)$-copolymer (poly(vinylidene fluoride-trifluoroethylene) (P(VDF-TrFE)) composites film developed by Bai *et al.,* in 2000 at Pennsylvania State University [82], while the first Pb-free RFE as energy storage capacitor was the copolymer P(VDF-TrFE) reported in 2003 [82]. Currently, different Pb-free dielectric materials starting from the ferroelectric materials to anti-ferroelectric materials and their combinations have been engineered to achieve superior energy storage performance. However, the underlying mechanism relating the dynamics of PNRs to the dielectric relaxation remained hidden. Very recently, Randall et al., observed the disappearance of the frequency dispersion in poled Pb-free $(Bi_{1/2}Na_{1/2})TiO_3$ (BNT) ceramics below T_m and thereby, resulting a shoulder like temperature (T_s) [83]. A similar shoulder like feature could be seen in PMN at the ageing temperature, however this will fade after re-annealing. Further, a critical temperature called T_d revealed a peculiar behavior in poled BNT, exhibiting a ferroelectric to relaxor phase transition, as well as a change in crystal structure from *R*3*c* or *P*4*mm* to *P*4*bm* as in PMN ceramics. It doesn't mean that T_s in BNT is equivalent to T_m in PMN, because the permittivity in PMN experience a decline and come to an end at T_D. However, the permittivity in BNT rises from T_s to T_m and then, freezes at the frequency independent T_m. At this stage, PMN and BNT have a similar behavior. However, a "breathing model" is used to explain the anomaly in the permittivity arises from T_s to T_m in BNT ceramics. According to this model, the temperature region (T_s to T_m) corresponding to the permittivity rise is dominated

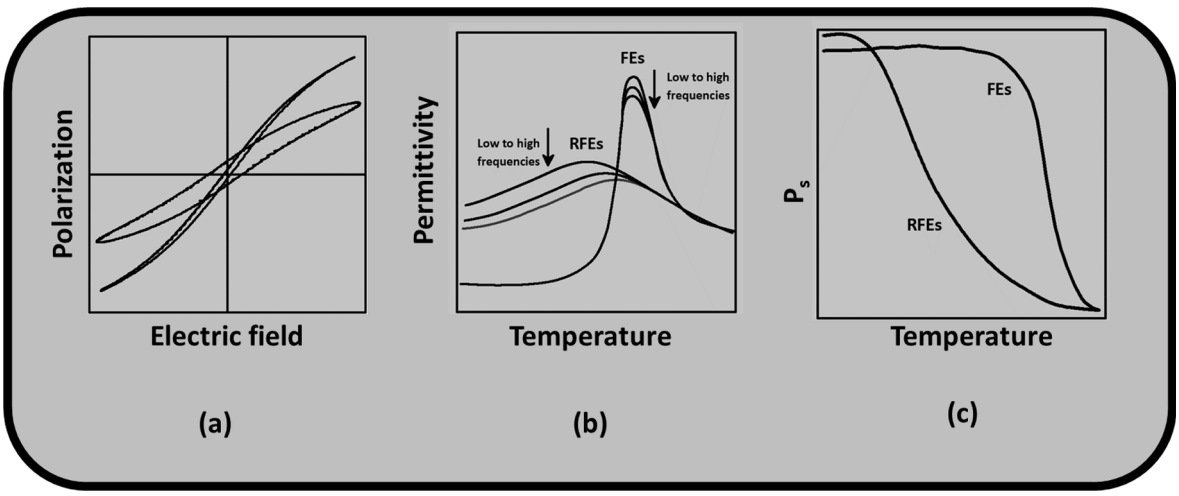

Fig. 8. Schematic representation of the difference between FEs and RFEs: (a) P-E loop behavior; (b) permittivity as a function of temperature; (c) spontaneous polarization as a function of temperature.

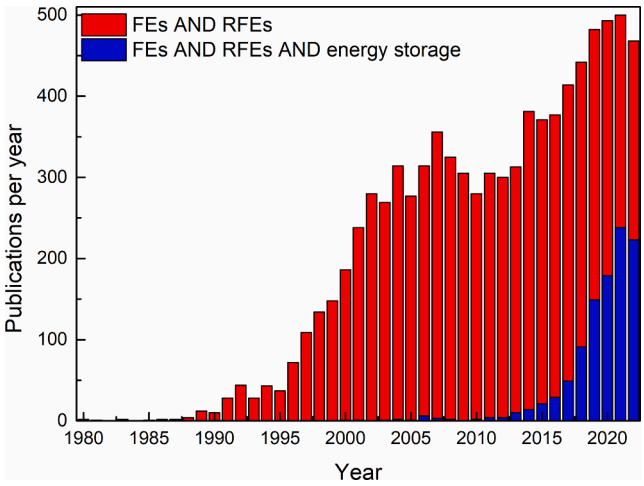

Fig. 9. Publication per year from 1980 to 2022 (Source: Web of science data base (http://apps.webofknowledge.com/); keyword search: topic = (relaxor and ferroelectrics) or topic = (relaxor and ferroelectrics and energy storage)). *represents in 2022 we collect the data up to month of November.

by the size of the PNRs. Within this temperature range, the PNRs expand in size and the number density rises. Consequently, an increased permittivity. This model points out the fact that the PNR dynamics in BNT can be controlled via different methods of cooling (rapid, bias, and compressed cooling) by creating a perturbation and thereby, engineering the size of the PNR. Therefore, the study of switching dynamics of PNRs are important for the complete understanding of the materials properties.

This section covers almost all the Pb-free RFE based ceramic systems investigated for energy storage capacitor applications. In order to facilitate reading, we group these materials in the large families of most used materials.

4.2.1. Bismuth sodium titanate (BNT) based RFE ceramic systems

Lead-free (Bi,Na)TiO_3 (BNT)-based ceramics developed by Smolenskii *et al.*, continued to receive attention owing to their excellent long-range ferroelectric ordering and several structural phase transitions within room temperature up to 800 K [84,85]. Usually, the BNT exhibits a rhombohedral ferroelectric structure at room temperature and a weak tetragonal structure (either RFE or AFE phase) in the range 594–813 K [85]. In 2014, Wang *et al.*, first investigated energy storage properties of bismuth sodium titanate (BNT) based systems [86]. However, the RFE based BNT systems attained their full swing as energy storage ceramics after the work reported by Luo *et al.,* [87]. They reported a simple binary solid solution of (1 - x)[$Bi_{0.5}Na_{0.5}$]TiO_3 (BNT)–x$KNbO_3$ (KN) (x = 0 – 0.12) prepared by the conventional sold state reaction method and achieved a W_r of 1.17 J/cm^3, at 104 kV/cm, in BNT–0.1KN. Furthermore, the BNT–0.1KN demonstrated good temperature stability and fatigue-free performance throughout the temperature range 20–100 ^{0}C. The better energy storage characteristics in BNT–0.1KN ceramics arise from their enhanced relaxor behavior. Likewise, different additives like MgO, $CaZrO_3$ and $SrZrO_3$ were used to improve the energy storage performance of BNT systems through enhancing the relaxor behavior [88–90]. In addition to KN, $NaBiNbO_3$ (NBN), $BaTiO_3$, $SrTiO_3$ (STO), $AgNbO_3$, $NaTaO_3$ (NT), $BaZrTiO_3$ (BZT), etc were also considered as additives in BNT for enhancing the energy storing [91–110]. Following this trend, in early 2016, Tang *et al.*, optimized the ternary composition 0.6$Bi_{0.5}Na_{0.5}TiO_3$–0.2$NaNbO_3$–0.2$Ba(Zr_{0.2}Ti_{0.8})O_3$ (BNT-NN-BZT) for investigating the energy storage properties [102]. The studies revealed that the introduction of BZT into the BNT-NN system changed the crystal structure from tetragonal to pseudocubic phase, at room temperature (RT) [102]. Further, Zr substitution at the B-site of BNT induces the disorder and thus, enhances the dielectric maximum and also causes an ergodic relaxor phase transition [102]. Besides, the BNT-NN modified with BZT improved the dielectric constant, temperature stability, and achieved a high energy storage property. In fact, the W_r showed an increase from 0.71 J/cm^3 (BNT-NN) to 1.69 J/cm^3 (BNT-NN-BZT) [102]. Bai *et al.,* reported a BNT-BCZT based relaxor ceramic which delivered a W_r of 0.95 J/cm^3 and η of 69 %, at 110 kV/cm. Through the incorporation of BCZT into the BNT matrix, a phase transition from non-ergodic to ergodic relaxor state and the formation of dynamic polar nanoregions (PNRs) is observed. The PNRs thus generated offer high strain and thereby an enhanced energy storage performance [111]. Huang *et al.*, fabricated BNT-BZT based RFE which simultaneously achieved a very good W_r = 3.1 J/cm^3 with an η = 91 % at 280 kV/cm. The excellent energy storage performance in BNT-BZT is ascribed to the dense microstructure with minimal pores, pseudocubic symmetry and the strong relaxor characteristic [112]. In the next work, Hu *et al.,* described the BNT-NBN systems, which showed a W_r of 2.41 J/cm^3, at an applied electric field of 280 kV/cm, with an η of 81.6 %. The introduction of NBN in BNT significantly improved the breakdown strength, as well as, the energy storage density through the reduction of grain size and by the reduction of oxygen vacancies [113]. In the latter work, the NT addition in BNT resulted in a slim *P-E* loop with an excellent energy storage density 4.21 J/cm^3, under 380 kV/cm [114]. Such a high energy storage performance in BNT-NT system arose from the ergotic relaxor behavior due to the co-existence of *R3c* nanodomains and *P4bm* polar nanoregions. This induced a large P_m and sufficiently low P_r, which is a consequence of the domain size reduction and the domains dynamics enhancement with the introduction of NT. However, the large-sized ferroelectric domains will absorb a considerable amount of energy for domain aligning, switching, and even stored as remanence. In contrast, the small sized domains or

microdomains respond very fast to tiny external electric field and activate the PNRs. As a consequence, a nearly hysteresis-free polarization response was observed in PNRs based systems [114]. To further improve the W_r of BNT ceramics by inducing relaxor behavior, new types of dopants and binary/ternary solutions strategies were introduced [115–131]. Zannen *et al.*, studied the energy storage properties of $Na_{1/2}(Bi_{0.98}Gd_{0.02})_{1/2}TiO_3$ and reported an W_r of 0.85 J/cm^3, at 60 kV/cm, with an η 90 %. The incorporation of the nonvolatile Gd^{3+} compensate the ferroelectric hysteresis loss and improved the relaxor behavior by reducing the number of oxygen vacancies, which are eventually created due to the highly volatile Bi and/or Na elements [115]. Besides, different dopants like Ba, Sr, or Sn, were introduced to improve the energy storage performance through enhancing the relaxor behavior [116–118]. On the other hand, (1-x)$Na_{0.5}Bi_{0.5}TiO_3$-x$BaSnO_3$ (BNT-BSN) binary solution exhibited a W_r 1.91 J/cm^3 at 190 kV/cm. With increasing BSN content, a slimmer *P-E* loops and a gradual decrease in the energy loss is observed. The increased breakdown strength of BNT-BSN ceramics is attributed to the suppression of the leakage current density whereas the slim behavior of the *P-E* loops arises from the large amount of weakly polar phase by addition of excessive content of BSN [119]. Further, different combinations of binary solutions like (1-x)[$(Na_{0.5}Bi_{0.5})_{0.95}Ba_{0.05}$]$_{0.98}La_{0.02}TiO_3$-x$K_{0.5}Na_{0.5}NbO_3$, (1-x)$Na_{0.5}Bi_{0.5}TiO_3$-x$LaAlO_3$, (1-x)[$(Na_{0.5}Bi_{0.5})_{0.4}Sr_{0.6}TiO_3$]-x$K_{0.73}Bi_{0.09}NbO_3$, and 0.85$(Na_{0.5}Bi_{0.5})_{0.7}Sr_{0.3}TiO_3-0.15Bi(Mg_{2/3}Nb_{1/3})O_3$ were investigated[120–123]. Furthermore, recently reported BNT based ternary RFE systems include (1-x)[0.76$Na_{1/2}Bi_{1/2}TiO_3$-0.24$SrTiO_3$]-x$AgNbO_3$ and (1-x)[0.94$Na_{0.5}Bi_{0.5}TiO_3$–0.06$BaTiO_3$]–x$Na_{0.73}Bi_{0.09}NbO_3$ [124,125]. It is reported that the incorporation of acceptor induced defect dipoles, such as introducing Mn^{2+}, Mg^{2+} in BNT-based systems, can result in higher P_{max} and lower P_r. As a result, the substitution of Mn^{2+} or Mg^{2+} in B-site adjusts the relaxation characteristic and enhances energy storage performance of BNT matrix [126,127]. For instance, the MgO doping in BNT based ceramics improved the W_r to 2.06 J/cm^3 at 200 kV/cm. The addition of MgO forms a disordered microdomains or nanodomains characterized by the small and irregular regions (PNRs), which enhances the relaxor behavior. The PNRs make the domain reorientation much easier and a subsequent decrease in P_r led to enhanced energy storage performance [127].

4.2.2. Barium titanate (BTO) based RFE ceramic systems

$BaTiO_3$ (BTO) is a promising Pb-free FE material and marked its signature as a capacitor material in the electronic industry due to its excellent dielectric and ferroelectric features. The BTO ceramics can be engineered to fabricate energy storage capacitors by using several additives such as Al_2O_3, SiO_2, and MgO that can improve the electric breakdown strength of $BaTiO_3$-based FE ceramics [132–134]. Still, the energy storage performance was not that much satisfactory due to the large hysteresis loss owing to the depolarization process. From this point of view, the logic of enlarging the difference between P_m and P_r to enhance the energy storage density came up. This can be achieved through the formation of a $BaTiO_3$-based RFEs with a broadened T_c and a peak's shifting that can serve as a good energy storage material. This put forwarded the idea of choosing ideal candidates as dopants in BTO to not only enhance the relaxor behavior but also to show a stable dielectric property and a high energy storage density up to higher temperature range (300 ^{0}C). This paved the development of BTO-$BiMeO_3$ [(Me represents single trivalent metallic ion or averagely trivalent metallic ions)] binary systems [34,35]. The purpose of forming solid solutions of $BiMeO_3$ with BTO ceramics is to utilize the Bi ion as a sintering aid and a donor dopant on A-site of the perovskite ABO_3 lattice. Ecofriendly bismuth (Bi) which is situated behind the lead (Pb) in the periodical table has attracted tremendous attention. Due to their comparable lone pair electronic 6 s^2 structure, Bi^{3+} ion is a viable alternative to Pb^{2+} ion. Further, the Bi_2O_3 has been traditionally serving as a sintering aid to improve the microstructure or as a dopant to tune the electrical properties of ceramics. Furthermore, the doping of BTO with the $BiMeO_3$ showed the shifting of the dielectric maxima toward lower temperature and exhibited better thermal stability compared to pure BTO. In this way, different RFE binary systems have been investigated. In 2015, three works were reported namely, (1 − x)BTO-x$BiYbO_3$ (BTO-BY), (1 − x)BTO-xBi$(Mg_{2/3}Nb_{1/3})O_3$ (BTO-BMN), and (1-x)BTO-xBi$(Mg_{1/2}Ti_{1/2})O_3$ (BTO-BMT) by conventional solid state route iby Li *et al.*, Hu *et al.*, and Wei *et al.*, separately [135–137]. These works show an enhanced dielectric permittivity ascribing to the T_c peak's shifting and a relaxor-like behavior. Most importantly, a temperature stable energy storage performance is achieved due to broad dielectric maximum [135–137]. The energy storage densities obtained in these works are 0.71 J/cm^3 (BTO-BY), 1.13 J/cm^3 (BTO-BMT), and 1.81 J/cm^3 (BTO-BMN) at 93 kV/cm, 143.5 kV/cm, and 224 kV/cm, respectively. This created more interest among the researchers and exploring more BTO-$BiMeO_3$ for energy storage properties. Different solid solutions with BTO includes $Bi(Li_{0.5}Nb_{0.5})O_3$, $Bi(Zn_{0.5}Zr_{0.5})O_3$, $Bi(Mg_{0.5}Zr_{0.5})O_3$, $Bi(Zn_{1/2}Sn_{1/2})O_3$, $Bi(Zn_{2/3}Nb_{1/3})O_3$, $BiNbO_4$, $Bi(Li_{0.5}Ta_{0.5})O_3$, $Bi(Ni_{1/2}Sn_{1/2})O_3$, $Bi(Mg_{2/3}Ta_{1/3})O_3$, $Bi(Mg_{1/2}Sn_{1/2})O_3$, $Bi(Li_{1/3}Zr_{2/3})O_3$, $Bi(Ni_{0.5}Zr_{0.5})O_3$, $Bi(Mg_{1/2}Ti_{1/2})O_3$, etc. were investigated [59,138–149]. Recently, Hu *et al.*, reported a high W_r equal to 4.49 J/cm^3 with a superior η of 93 % in the 0.6$BaTiO_3$-0.4$Bi(Mg_{1/2}Ti_{1/2})O_3$ (0.6BTO-0.4BMT) ceramics [149]. The enhanced energy storage density is attributed to the polarization mismatch created by the $Bi(Mg_{1/2}Ti_{1/2})O_3$ in the A-site and B-site of $BaTiO_3$. Usually, the ferroelectricity in BTO occurs as a consequence of A-site and B-site cations displacements, namely A-O and B-O coupling, respectively. The introduction of BMT in BTO reduces the remnant polarization through interrupting the macroscopic polarization by suppressing the A-O coupling and B-O coupling. This develops a nano-scale polarization mismatch and consequently, enhanced the energy storage density [149]. In addition, several other dopants like $YNbO_4$, $K_{0.73}Bi_{0.09}NbO_3$, $CaSnO_3$, $KNbO_3$, etc. were introduced in the BTO systems to improve the relaxor characteristics [150–156]. For instance, fine-grained (1-x) $BaTiO_3$-x$KNbO_3$ ceramics fabricated by Huang *et al.,* achieved a recoverable energy density of 2.03 J/cm^3 with a relatively high efficiency of 94.5 %, at 300 kV/cm [153]. According to them, the grain size under a given electric field affects the distribution of the local electric field. A large electric field concentrates on the grain boundary region, which is much higher than that on the grains and is considered as one of the main reasons for the dielectric breakdown. However, the introduction of $KNbO_3$ in BTO drives the grain size to submicron scale. As a consequence, the heterogeneity of the local electric field on the grain boundary region is weakened. This contributes to the higher dielectric strength [153]. Moreover, the slim *P-E* loops are ascribed to the smaller grain size which constitutes the relaxor behavior through the formation of PNRs. At present, the search for new-type RFE based ferroelectrics with better energy storage performances by inducing relaxor phase transition has been a hot spot and BTO based RFEs elevated the energy storage ceramics to a higher level.

4.2.3. Potassium sodium niobate (KNN) based RFE ceramic systems

Though potassium sodium niobate (KNN) belongs to the family of ferroelectric materials, it attracted special attention for the application in the transparent electronic devices such as touch panels and smart phones [157,158] due to high transparency. However, the large hysteresis loss (due to large P_r) and the low dielectric breakdown strength make these materials unsuitable for practical applications. It is possible to overcome these barriers through compositionally controlled grain size and porosity reduction [5,55,159–166]. In 2016, Qu *et al.,* fabricated a transparent KNN based $(1-x)$KNN-xSr$(Sc_{0.5}Nb_{0.5})O_3$ (KNN-SSN) RFE system by the conventional solid-state reaction route [158]. The introduction of SNN not only improved the transparency (~ 60 % at 0.7 μm thickness), but also enhanced energy storage performance through grain size reduction (4–8 μm to 0.4 μm) and increased density. The relaxor behavior in KNN-SSN system is attributed to the B-site (Nb^{5+}) substitution of KNN by the Sc^{3+} whose ionic radii is comparatively smaller than Nb^{5+}. The difference in the ionic radii and valence states of host and doping elements creates an imbalance in the charge as well as induces local elastic field. This in turn develops a local electric field. This led to structural distortion and forms PNR by disrupting the long-range dipole alignment, which is responsible for the formation of the pseudocubic phase. It is observed that the inclusion of SNN reduces grain size and thus, the optical transparency in KNN-SSN system aroused due to low scattering at the grain boundaries. All these properties contributed to the energy storage performance of KNN-SSN and showed a W_r of 2.08 J/cm^3, at 294 kV/cm [158]. Further, to improve the energy storage density of KNN-SSN RFEs through enhancing the breakdown strength, Qu *et al.*, also introduced ZnO into KNN-SNN. As a consequence, an increase in the dielectric breakdown strength up to 400 kV/cm followed by an increased in the energy storage density up to 2.6 J/cm^3 was achieved [5]. In KNN perovskite structure, the doping of Zn^{2+} is governed by Pauling's rules and ionic size. The Zn^{2+}could replace Nb^{5+}or Sc^{3+} (B-site) in octahedral sites and play a major role in the 'hardening" effect in KNN-SSN ceramics. Consequently, an enhanced breakdown strength was successfully obtained. In addition, different dopants like $Bi_{0.60}(Mg_{1/3}Nb_{2/3})O_3$, $Sr(Zn_{1/3}Nb_{2/3})O_3$, $(K_{0.7}Bi_{0.3})NbO_3$, $Ba(Zn_{1/3}Nb_{2/3})O_3$ where hosted to induce relaxor behavior in the KNN and successfully gained the energy storage density values as 1.30, 3.00, 3.39, and 4.87 J/cm^3, respectively [162–165]. Therefore, KNN based RFE systems can be considered as ideal candidates for both optical and energy storage materials. Moreover, their translucency-based energy storage characteristics make them useful for multifunctional material applications, especially in military field.

4.2.4. Strontium titanate (STO) based RFE ceramic systems

Strontium titanate ($SrTiO_3$, STO) are linear dielectrics with exceptionally good physical properties such as moderate dielectric constant (~ 290), relatively high BDS (~ 200 kV/cm) and low dielectric loss (<0.01). Therefore, the STO-based ceramics are receiving greater interest and have been extensively studied [24,26,167–179]. However, as mentioned before for the LDs, the STO ceramics suffer low W_r owing to the low P_{max} value, which arises from the inherent linear behavior and are too small to meet the practical application. Therefore, several candidates where successfully utilized as dopants to enhance both ferroelectric as well as the relaxor behavior in the STO systems. In 2017, Yang *et al.*, showed an enhanced energy storage performance in STO based ceramics through the introduction of different dopants such as [$BaTiO_3$-$Bi_{0.5}Na_{0.5}TiO_3$], [$Bi_{0.5}Na_{0.5}TiO_3-BaAl_{0.5}Nb_{0.5}O_3$], [$Bi_{0.5}(Na_{0.82}K_{0.18})_{0.5}$-$Ti_{0.96}Zr_{0.02}Sn_{0.02}O_3$], [$Bi_{0.5}Na_{0.5}TiO_3$-$Ba_{0.94}La_{0.04}Zr_{0.02}Ti_{0.98}O_3$], [$Bi_{0.48}La_{0.02}Na_{0.48}Li_{0.02}Ti_{0.98}Zr_{0.02}O_3$] and reported a W_r of 1.40, 1.89, 1.45, 2.83, and 2.59 J/cm^3, respectively. The enhanced energy storage performance is ascribed to the improved relaxor behavior and decreased grain size to submicron range. Moreover, the addition of these dopants improved the saturation polarization [168–172]. In the same year, Cui *et al.*, reported an enhanced energy storage performance in the [$(Na_{0.5}Bi_{0.5})TiO_3$] doped STO system by the conventional solid state reaction method. They achieved a discharge energy density = 1.18 J/cm^3 at 210 kV/cm. The broad relaxor behavior due to the increased lattice disorder and the thermal evolution of PNRs are the key factors that are responsible for the enhanced energy storage performance in (1-x)$SrTiO_3$-x$(Na_{0.5}Bi_{0.5})TiO_3$ ceramics [173]. After words, Jan *et al.*, realized a high W_r = 1.93 J/cm^3 with an exceptionally good dielectric breakdown strength of 420 kV/cm in (1-x)STO-x$(0.93Bi_{0.5}Na_{0.5}TiO_3$-$0.07Ba_{0.94}Sm_{0.04}Zr_{0.02}Ti_{0.98}O_3$) (STO-BNT-BSZT)[174]. The increased breakdown strength is ascribed to the high insulation behavior due to the introduction of BNT-BSZT. This insulation behavior rises from the low conductivity. This is due to the fact that the degree of stability in the valence state of Zr^{4+} is much higher than that of the Ti^{4+}. So Zr^{4+} acts as a blockage for the suppression of Ti^{4+} and Ti^{3+}. Consequently, the hopping distance effectively increases and this reduces the leakage current with minimum energy loss [19]. Further, the substitution of Zr^{4+} in Ti^{4+} site would increase the band energy and the grain boundary density. Both these effects might have limited the conduction and causes an enhancement in breakdown strength [174]. Moreover, STO is modified as $Sr_{0.8}(Na_{0.5}Bi_{0.5})_{0.2}$-$TiO_3$, and $Sr_{0.7}Bi_{0.2}Ca_{0.1}TiO_3$ to improve the energy storage performance [175,176]. The substitution of Bi^{3+} in Sr^{2+} site improves the relaxor behavior and a diffused dielectric maximum in a wide range of temperatures. Further, the SBT shows a high dielectric constant which is derived from the dipole polarization associated with dipole fluctuation of PNRs. Moreover, a high energy storage efficiency was obtained in SBT owing to the low remnant polarization and coercive field.

4.2.5. Bismuth ferrite (BFO) based RFE ceramic systems

$BiFeO_3$ (BFO) are promising Pb-free ferroelectric material due to its outstanding inherent polarization ($P > 100$ μC/cm^2) and the Bi^{3+} has a lone 6 s^2 electron configuration alike to Pb^{2+} ions [180,181]. This increases the scope of BFO based ceramics in enhancing energy-storage properties. Unfortunately, the undoped BFO is not suitable for the energy-storage application owing to its relatively large P_r and a high electrical leakage current. To tackle such issues for achieving high W_r and η, most of the studies concentrated on BFO based ternary solid solutions [182–191]. For instance, the $Ba(Zn_{1/3}Ta_{2/3})O_3$ (BZT)-modified BFO-BTO ceramic showed a pinched-hysteresis loops, which is greatly beneficial to enhance energy-storage performance. The BFO-BT-BZT exhibited a recoverable energy density (2.56 J/cm^3) under low electric field (160 kV/cm) [182]. The Zn^{2+} (1.297 Å^3) ions develop a stronger ionic bond than Fe^{3+} (2.14 Å^3) owing to its lower polarizability when compared with Fe. This in turn contributes to the appearance of short-range-ordered

polar clusters or PNRs. Furthermore, the substitution of Ta^{5+} in Fe^{3+}retains the PNRs as the polarizability of Ta^{5+} (2.82 $Å^3$) is higher than Fe^{3+} (2.14 $Å^3$). Moreover, the incorporation of these non-isovalent ions into the host lattice derive a local random field due to the local charge imbalance and mismatch strain. Further, the charge imbalance created due to Ta^{5+} substitution develops a weakly coupled polar structure and thereby, enhances the relaxor nature. Consequently, an improved energy storage performance was obtained. On the other hand, a $W_r \approx 1.56$ J/cm^3, at 125 kV/cm, was reported by Zuo *et al.*, for $Ba(Mg_{1/3}Nb_{2/3})O_3$ doped BFO-BTO ceramics [183]. Followed by a similar work with $La(Mg_{1/2}Ti_{1/2})O_3$ modified BFO-BTO ceramics displayed a W_r of 1.66 J/cm^3, at 130 kV/cm [184]. More recently, BFO-BTO ceramics modified with different dopants have been severely studied and this modifications include BFO-BTO with $Sr(Al_{0.5}Nb_{0.5})O_3$, $Nd(Zn_{0.5}Zr_{0.5})O_3$, $(Sr_{0.7}Bi_{0.2})TiO_3$, and $AgNbO_3$[185–188]. However, there are a few reports on BFO-BTO binary systems modified using several dopants [189,190]. For instance, Dabas *et al.*, reported an Mn based (1-x) $BiFe_{0.95}Mn_{0.05}O_3$-x$BaTiO_3$ RFE system exhibiting a W_r 1.97 J/cm^3 with an efficiency of 81.7 %. The higher valence state dopant such as Mn^{4+} in the B- site suppresses the structural defects such as oxygen vacancies and thereby, increasing the polarization, followed by an enhanced energy storage density [190].

4.2.6. Other RFE ceramic systems

This section deals with the recently investigated Pb-free RFE ceramic systems that do not fall into the previous categories [104,155,166,192–200]. Here, we will discuss some of the selected RFE systems and it includes $NaNbO_3$ (NNO), $Ba_{0.9}Sr_{0.1}TiO_3$ (BST), and (1-x)$Ba(Zr_{0.2}Ti_{0.8})O_3$-x$(Ba_{0.7}Ca_{0.3})TiO_3$ (BZCT). Generally, NNO is anti-ferroelectric in nature. However, the pure NNO ceramic exhibited a saturated *P-E* loop with large P_r and hysteresis loss. To reduce the large P_r caused by ferroelectric macrodomains and to further improve the energy storage behavior, the strategy of doping with $BMeO_3$ was implemented. Recently, several investigations were carried out in NNO-$BMeO_3$ systems [192,193]. Fan *et al.*, reported a W_r 2.20 J/cm^3 at 250 kV/cm in 0.91$NaNbO_3$-0.09Bi$(Zn_{0.5}Ti_{0.5})O_3$ (NNO-BZT) [192]. The improved P_{max} is attributed to the hybridization between Bi^{3+} 6p orbital and O^{2-} 2p orbital. Further, the introduction of B-site ions with larger ionic radii (Zn^{2+}+Ti^{4+}, $r_{effective}$ (0.673 Å) substitute the r_{Nb5+} (0.64 Å) and induces a larger polarization of the polar clusters. Moreover, the heterovalent Zn^{2+} and Ti^{4+} in B-site reduces the P_r through lowering the average electronegativity and promotes the random local field which inhibits the long-range ferroelectric order. This enhances the ionic bonding and the relaxor behavior, which improves the energy storage properties. Liu *et al.*, introduced (1-x) $Ba_{0.9}Sr_{0.1}TiO_3$-x$Bi(Zn_{0.5}Zr_{0.5})O_3$ (BST-BZZ) RFEs by the conventional solid-state reaction method. This work displayed a W_r 1.11 J/cm^3, at 170 kV/cm [193]. The increase of the BZZ content not only shifts the T_c toward lower temperature, but also induces strong relaxor behaviors with diffused phase transition characteristics along with an increased energy storage performance. Further, a highly dense microstructure with a pseudocubic perovskite phases in BST-BZZ also promoted the energy density.

On the other hand, the Pb-free (1-x)$Ba(Zr_{0.2}Ti_{0.8})O_3$-x$(Ba_{0.7}Ca_{0.3})TiO_3$ [BZCT] based RFEs solid solutions are very new in the energy storage density studies [7]. These morphotropic phase boundary owned ceramic systems have superior piezoelectric properties comparable with the one found in lead based ceramic systems [199]. Further, these ceramics show good relaxor behavior in the range $\times$ = 0.4–0.6 [7]. For instance, it is possible to increase W_r and E_B of BZCT through the formation of RFE-paraelectric BZCT-STO solid solution and reported a W_r 0.987 J/cm^3, at 108 kV/cm [200]. The incorporation of STO disrupts the long-range ferroelectric order of BZCT and causes a weakly coupled structure to improve the relaxor behavior. Further, the bond length calculation suggested a shorter bond length for d_{Sr-O} (2.35 Å) as compared to d_{Ba-O} (2.40 Å). Thus, the Sr–O bond is more stable than the Ba–O bond. As a result, the dielectric loss is found to be decreased when compared to BZCT and an enhanced breakdown strength through STO doping [200].

Table 1
Energy storage properties reported in various RFEs based ceramic systems via different strategies.

Material	Strategies	W_r (J/cm^3)	E_B (kV/cm)	η (%)	Year	Ref no
$Sr_{0.7}Bi_{0.2}Ca_{0.1}TiO_3$	Doping	2.1	290	97.6	2020	[176]
0.9$(Sr_{0.7}Bi_{0.2})TiO_3$-0.1$Bi(Mg_{0.5}Hf_{0.5})O_3$	Doping	3.1	360	93	2020	[178]
0.55$Bi_{0.5}Na_{0.5}TiO_3$-0.45$Sr_{0.7}La_{0.2}TiO_3$	Doping	4.14	3.15	92.2	2020	[108]
0.6$BaTiO_3$-0.4$Bi(Mg_{1/2}T_{1/2})O_3$	Doping	4.49	340	93	2020	[155]
0.75$Bi_{(0.5+x)}Na_{(0.5-x)}TiO_3-0.25SrTiO_3$	Doping	5.63	535	94	2020	[110]
0.80$Bi_{0.5}Na_{0.5}TiO_3$-0.20$SrNb_{0.5}Al_{0.5}O_3$	Doping	6.64	520	96.5	2020	[202]
BTO-KN	Doping	2.03	300	94.3	2020	[203]
0.95SBKT-0.05NNO	Doping	2.45	220	93.1	2021	[204]
0.98BZCT-0.02BZ	Microstructure tailoring	2.61	150	91	2020	[207]
$Na_{0.7}Bi_{0.1}NbO_3$	Microstructure tailoring	3.41	280	90.8	2019	[193]
$(Bi_{0.32}Sr_{0.42}Na_{0.20})TiO_3$/MgO	0–3 type composite	2.09	200	84	2019	[213]
BZCT/ZnO	0–3 type composite	2.61	282	74	2020	[214]
0.78$NaNbO_3$-0.22$Bi(Mg_{2/3}Ta_{1/3})O_3$	Local random field	5.01	627	86.1	2019	[215]
$BiFeO_3$-$BaTiO_3$-$NaNbO_3$	Nano domain engineering	8.12	700	90	2020	[217]
BTAS-BTBZNT	Layer by layer engineering	5.04	790	68	2019	[218]
BF-BT-NZZ	MLCCs	10.5	700	87	2019	[220]
BT-BZNT	MLCCs	8.13	750	95	2019	[224]
BTBZNT	MLCCs	10.5	1000	93.7	2020	[225]
BNT-SBT-0.08BMN	MLCCs	18	1013	93	2021	[226]

5. Different strategies adopted for high quality relaxor ferroelectric fabrication

In this section, we discuss the most promising strategies adopted to improve the energy storage performance of RFEs ceramics systems, such as doping, microstructure tailoring, semiconductor/relaxor 0–3 type composites, local random field strategy, nano domain engineering, layer-by-layer engineering, and multi-layer ceramic capacitors (MLCCs). Further, in each strategy, we briefly discuss the energy storage performance of the recently published works and in Table 1 we summarized the most efficient energy storage materials obtained from each strategy adoption.

5.1. Doping

Doping is considered as one of the best options to modify the relaxor properties of a material by doping with a single element, multiple elements and even by the formation of binary or ternary solid solution [73,201,202]. Recently, Zhao *et al.*, fabricated the relaxor $Sr_{0.7}Bi_{0.2}Ca_xTiO_3$ (SBT-xC, x = 0 ~ 0.15) via the conventional solid-state reaction method and reported a high W_r 2.1 J/cm^3 with a very high η 97.6 %, at 290 kV/cm [176]. The introduction of Ca in SBT matrix formed a pseudo-cubic structure with an increment in the relaxor behavior as well as an increase in the dielectric constant. Further, the addition of Ca inhibits the grain growth and significantly reduced the grain size of SBT from 2.47 μm to 1.43 μm. Moreover, the incorporation of Ca in the SBT ceramics significantly reduced the leakage current density and thereby a decreased electrical conductivity. This arises from the small grain size due to Ca doping, which contribute to the removal of oxygen vacancies and consequently, enhances the breakdown strength. Therefore, the enhanced W_r in SBT is attributed to the improved pseudocubic nature, smaller grain size, improved dielectric constant and superior breakdown strength as shown in the Fig. 10. As a result, the SBT-0.1C showed an enhancement in the *EB* to 480.2 kV/cm. Moreover, SBT-0.1C exhibited an excellent temperature stability with the variation of W_r<9 % in the temperature ranging from −20 ^{0}C to 120 ^{0}C with a high η of ~ 98 % at 180 kV/cm. Besides, outstanding frequency stability over the range of 10–250 Hz is achieved. In addition, SBT-0.1C exhibits a very good discharging performance with a short $\tau_{0.90}$ 0.124 μs and a power density of 50.1 MW/cm^3 at 300 kV/cm. In addition, different dopants such as Sn, Cu, Mg, etc. were recently used as dopants for improving the energy storage performance of SBT [127,166,177].

Very recently, Yan *et al.,* developed a high performance Pb-free (1-x)$Bi_{0.5}Na_{0.5}TiO_3$-x$SrNb_{0.5}Al_{0.5}O_3$ ((1-x)BNT-xSNA) solid solution for energy storage [202]. Here, the introduction of SNA in BNT not only displayed a strong relaxor behavior but also exhibited a dense microstructure, and a decreased grain size. With the increasing SNA content, a frequency dispersion behavior (broad dielectric peak) with an increased dielectric constant at room temperature is observed; which is a typical characteristic of the RFEs. Further, the incorporation of SNA suppressed the grain size from 1.94 μm to 0.54 μm, which is beneficial for achieving high *EB* [55]. Besides, the BNT-SNA ceramics exhibited a slimmer *P-E* loop with a high P_m and low P_r value. This is ascribed to the induced PNR by the Sr^{2+} ion and $(Al_{0.5}Nb_{0.5})^{4+}$ complex-ion into BNT matrix. Moreover, the bright field transmission electron microscopy (BF-TEM) analysis revealed a speckled domain morphology corresponding to PNRs in 0.80BNT-0.20SNA ceramic (Fig. 11(a)-(b)). As a result, 0.80BNT-0.20SNA attained an ultra-high W_r of 6.64 J/cm^3 accompanying with an excellent η of 96.5 % and an *EB* of 520 kV/cm (Fig. 12(c)). Moreover, the Weibull distribution function exhibited a linear fit for all the samples with the Weibull modulus β higher than 5 for each composition and showed less dispersion in the data (Fig. 11(d)) [33,57]. Further, the higher β value suggested an increase in *EB* from 372 kV/cm to 577 kV/cm with × varied from 0.10 to 0.30 (inset in Fig. 11(d)). Thus, the enhanced energy storage performance in BNT-SNA ceramics is attributed to the induced PNRs and decreased grain size to submicron scale (Fig. 11(e)). Huang *et al.,* reported a W_r of 2.03 J/cm^3 at 300 kV/cm with a superior η of 94.3 % in 0.96$BaTiO_3$ − 0.04$KNbO_3$ [BTO-KN] solid solution [203]. The high energy

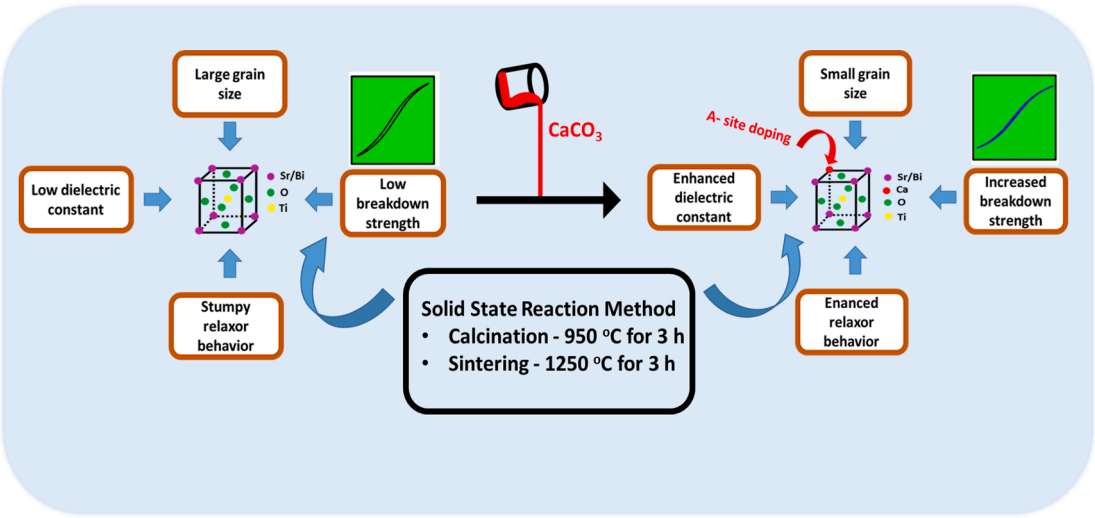

Fig. 10. Schematic representation of the effect of Ca doping in $Sr_{0.7}Bi_{0.2}TiO_3$ based on the procedure adopted in ref. [176].

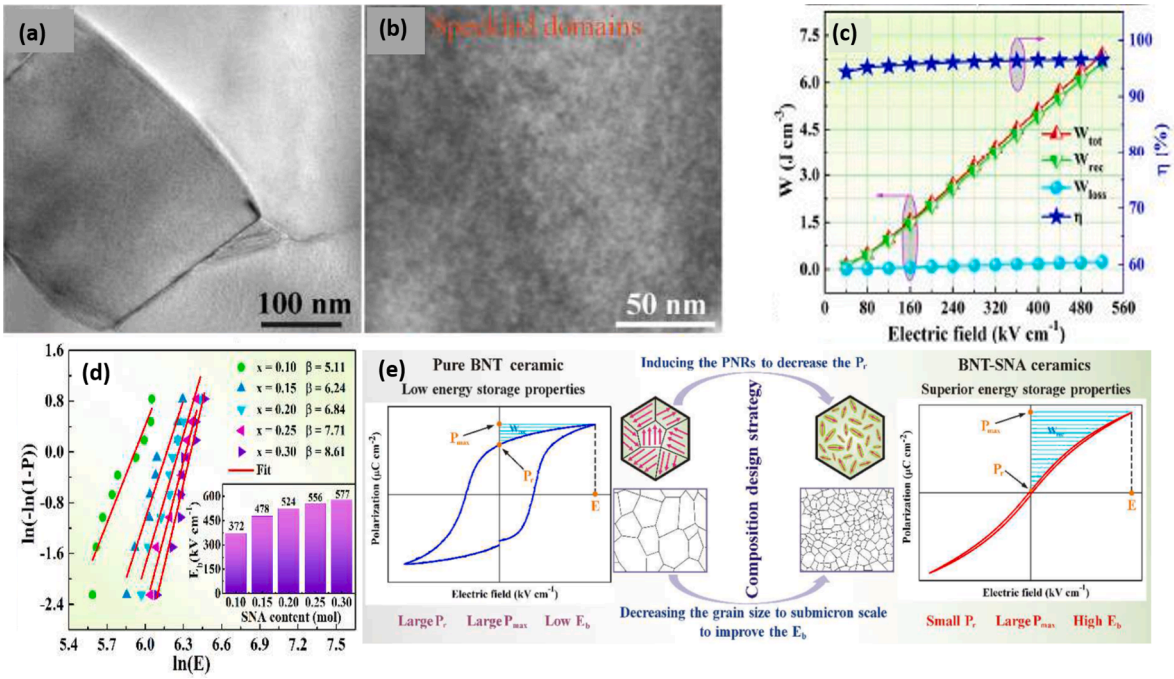

Fig. 11. (a)-(b) BF-TEM images of 0.80BNT-0.20SNA; (c) variation of W and η with applied electric fields; (d) Weibull distribution and the inset show the electric breakdown strength with increase in SNA content (e) diagrammatic representation of achieving high energy storage performance via composition design strategy. Reprinted with permission from Yan *et al.*, Superior energy storage properties and excellent stability achieved in environment-friendly ferroelectrics via composition design strategy, nano energy (2020). Copyright (2020) by the Elsevier ltd. [https://doi.org/10.1016/j.nanoen.2020.105012] [202].

storage performance in BTO-KN is the manifestation of PNR dynamics. Such a high energy storage performance is an exhibition of the dielectric relaxation w. r. t. to the doping and is attributed to the behavior of PNR dynamics arising from the aliovalent cation substitutions (K^+ and Nb^{5+}) at A-site and B-site of BTO. This in turn create a crossover region between T_D and T_m, where the PNR dynamics will be very high. Consequently, an enhanced dielectric permittivity and a large P_m with slim P-E loop. Furthermore, the relaxation time in the BTO-KN was tested and compared with pure BTO. The poling behaviours of BTO and BTO-KN were conducted at different poling voltages. After poling, BTO remained un affected even after 120 min, while the BTO-KN showed a decrease suggesting the presence of PNRs. This pointed out the fact that the preponderance of nanodomains in the domain structure corresponds to a faster relaxation time. At this crossover region, a superior thermal stability is observed and subsequently, a stable energy storage performance in BTO-KN solid solutions. Another work by Zhao et al., in 2021 reported enhanced energy storage performance in aliovalent cation (K^+) doped (1-x) $Sr_{0.35}Bi_{0.35}K_{0.25}TiO_3$ – xNNO (SBKT-NNO) ceramics [204]. The doping decreased the domain size and elevated the PNR dynamics with a broad dielectric maximum. Further, a slight increase in the current density and power density near the dielectric maxima are observed due to the highly dynamical PNRs. The 0.95SBKT − 0.05NNO solid solutions exhibited a $W_r \sim 2.45$ J/cm^3 with an $\eta \sim 93.1$ % at 220 kV/cm.

5.2. *Microstructure tailoring*

In addition to the doping, another important factor that controls the material characteristics is the sintering temperature [42,205]. Through sintering effect, it is possible to introduce the relaxor behaviour in a ceramic by controlling the grain size as well as the density of the ceramics [206,207]. However, the effect of grain size on relaxor behaviour and the energy storage performance was scarcely investigated [5]. Most of the studies on RFEs are particularly concentrated on energy storage properties especially through doping. In 2020, our research group proposed a new strategy by tuning the microstructure of 0.98BZCT-0.02Bi$Zn_{1/2}Ti_{1/2}O_3$ [BZCT-BZ] via sintering time to enhance the energy storage properties [207]. This is ascribed to the formation of the pseudocubic phase in the crystal structure and a significantly reduced grain size in the sub-micrometre range ((Fig. 12(a) - (b)) [208]. The variation in grain size with sintering time is explained based on Ostwald Ripening mechanism [209]. The grain size is found to be minimum in the samples sintered at 11hrs. The decrease in grain size of the sample sintered at 11 hrs disrupted the long-range ferroelectric by disturbing the translational symmetry through increasing grain boundaries and behaves like relaxor ferroelectrics [210]. Further, the crystal structure changes from tetragonal to a complete pseudocubic phase at 11 hrs, which is a typhical phase of the RFEs. Besides, it is reported that the domain size is proportional to square of the grain size. Therefore, the decrease in grain size promotes the formation of single domain rather than multi-domains. This diminutive the contribution of domains walls and domain switching due to pinning/clamping by grain boundaries and thereby a low P_r. As a consequence, a slimmer *P-E* loop with a nearly hysteresis loss free behavior is

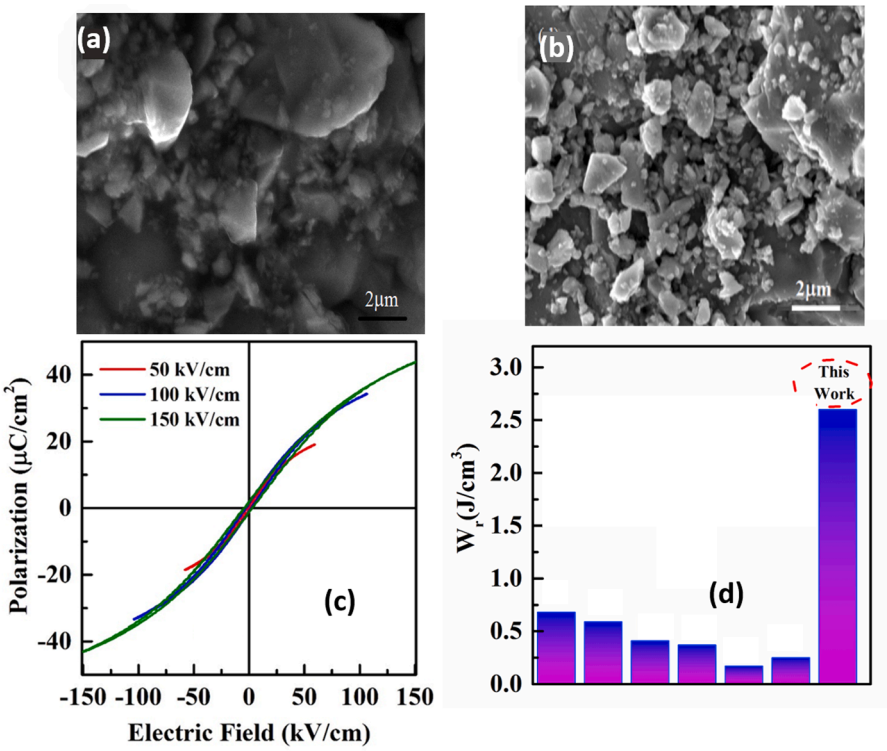

Fig. 12. (a)-(b) High resolution SEM images of BZCT-BZ ceramics sintered at 3hrs and 11hrs, respectively; (c) P-E loops of sample sintered at 11hrs as a function of electric field and (d) comparison of this work with other BZCT ceramics. Reprinted with permission from A. R. Jayakrishnan *et al.*, Microstructure tailoring for enhancing the energy storage performance of $0.98[0.6Ba(Zr_{0.2}Ti_{0.8})O_3\text{-}0.4(Ba_{0.7}Ca_{0.3})TiO_3]\text{-}0.02BiZn_{1/2}Ti_{1/2}O_3$ ceramic capacitors, Journal of Science: Advanced Materials and Devices, Copyright (2020) by the Elsevier ltd. [https://doi.org/10.1016/j.jsamd.2019.12.001] [207].

expected due to the smallest grain size. This work recovered a $W_r = 2.61$ J/cm^3 with an η 91 %, at 150 kV/cm, in BZCT-BZ RFE sintered at 11 hrs (Fig. 12(c)). Moreover, a comparitive study showed that the W_r of BZCT-BZ ceramics sintered at 11 hrs is 3–13 times higher than the reported values of other BZCT based ceramic capacitors and is shown in Fig. 12(d). Thus, this work not only provide a promising candidate for the energy storage capacitor fabrications, but also open the door for the BZCT based RFEs for real world energy storage capacitor applications.

5.3. Semiconductor/relaxor 0–3 composite formation

Dielectric breakdown strength (*EB*) is considered as one of the key parameter that contribute to the energy storage performance of a ceramic capacitor. However, most of the ceramics suffer from low *EB* due to unavoiadable pores formed during the high temperature sintering process. Therefore, it is mandatory to inhibit the breakdown by reducing the number of pores. This can be achieved through the formation of 0–3 semiconductor/relaxor composite formation [211]. The idea of designing a 0–3 type semiconductor/relaxor composite for energy storage capacitor fabrication started in the late 2018 by Tao *et al.*, They studied the energy storage performance of $0.82[0.94BNT\text{-}0.06BTO]\text{-}0.18$KNN:xZnO (BNT-BT-KNN:xZnO, with $\times$ varying from 0 to 0.40) semiconductor/relaxor composites and reported an increase in W_r from 0.74 J/cm^3 to 1.03 J/cm^3 with an increase in the breakdown electric field from 90 kV/cm and 140 kV/cm [211]. This is attributted to the enhanced bulk resistivity and the ZnO induced local electric field by the formation of isolated ZnO particles at the grain boundaries of the BNT-BT-KNN matrix which suppresses the evoltion of PNRs [211–213]. Here, the polar semiconductor ZnO provides the charges to form a local electric field to tune the ferroelectric properties and enhances the breakdown strength by decreasing the leakage current. Followed by his work, in 2019Li *et al.*, studied the energy storage performance $(Bi_{0.32}Sr_{0.42}Na_{0.20})TiO_3$ [BNST] by forming a 0–3 type composite with MgO [213]. All the BNST/MgO exhibited a pseudocubic nature and the negligible peak shifting suggests the low diffusion of Mg element into the BNST lattice. Besides, the formation of 0–3 type structure with MgO at the grain boundaries of BNST was confirmed using the elemental mapping [Fig. 13]. The presence of two dielectric anomalies in the BNST/MgO is attributed to the mutual transition between tetragonal-rhombohedral PNRs. Further, the pores and cracks were absent in the BNST/MgO composites. This arises from the lower sintering temperature, which minimize the chances of Mg diffusion. Therefore, a combined effect such as the presence of pseudocubic structure, formation of PNRs, and a pore free microstructure contributed to the enhanced energy storage performance of BNST/MgO composite. Thus, the BNST/MgO 0–3 type composite exhibited a very good energy storage execution with $W_r = 2.09$ J/cm^3, $\eta = 84$ %, and $EB = 200$ kV/cm [213]. Very recently,

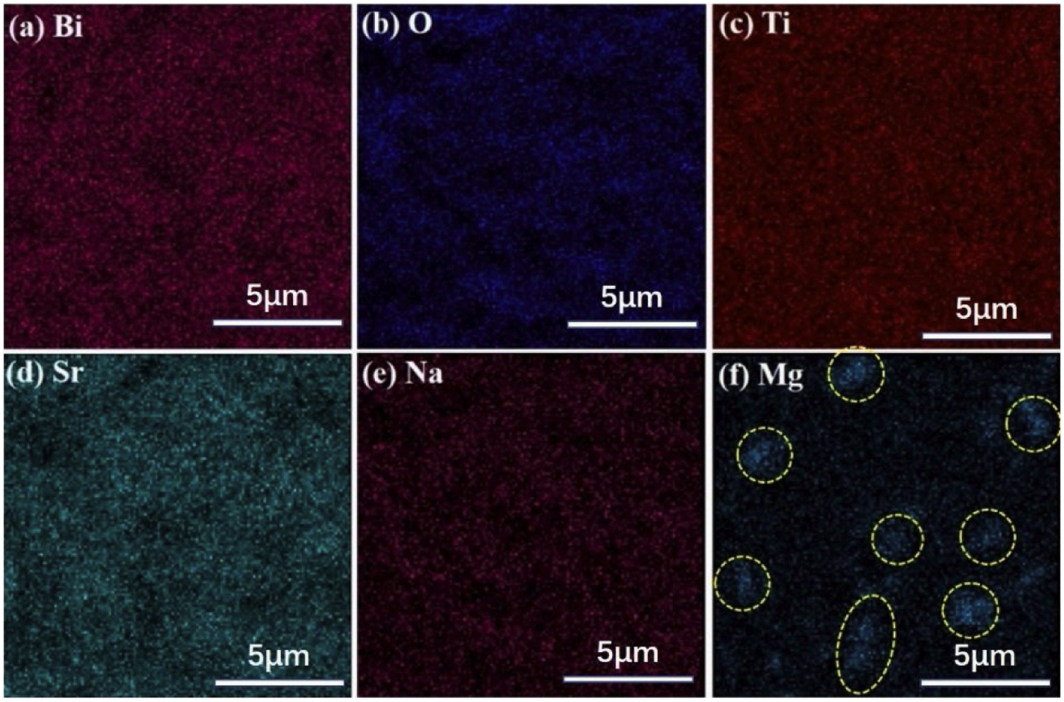

Fig. 13. Elemental mapping in BNST/MgO 0–3 type composite. Reprinted with permission from Li *et al*. Structure-design strategy of 0–3 type $(Bi_{0.32}Sr_{0.42}Na_{0.20})TiO_3$/MgO composite to boost energy storage density, efficiency and charge–discharge performance, J. Eur. Ceram. Copyright (2019) by the Elsevier ltd. [https://doi.org/10.1016/j.jeurceramsoc.2019.03.047] [213].

our research group reported a high energy storage density in BZCT/ZnO 0–3 type composite [214]. The presence of small ZnO particles at the grain boundaries of the BZCT grains suggested the formation of BZCT/ZnO 0–3 composites. The BZCT/ZnO composite showed a discharge energy density = 2.61 J/cm^3 and an efficiency = 74.2 %, at 282 kV/cm. The BZCT/ZnO composite achieved an enhancement of 166 % in the *EB* and 220 % in W_r when compared to the BZCT ceramics.

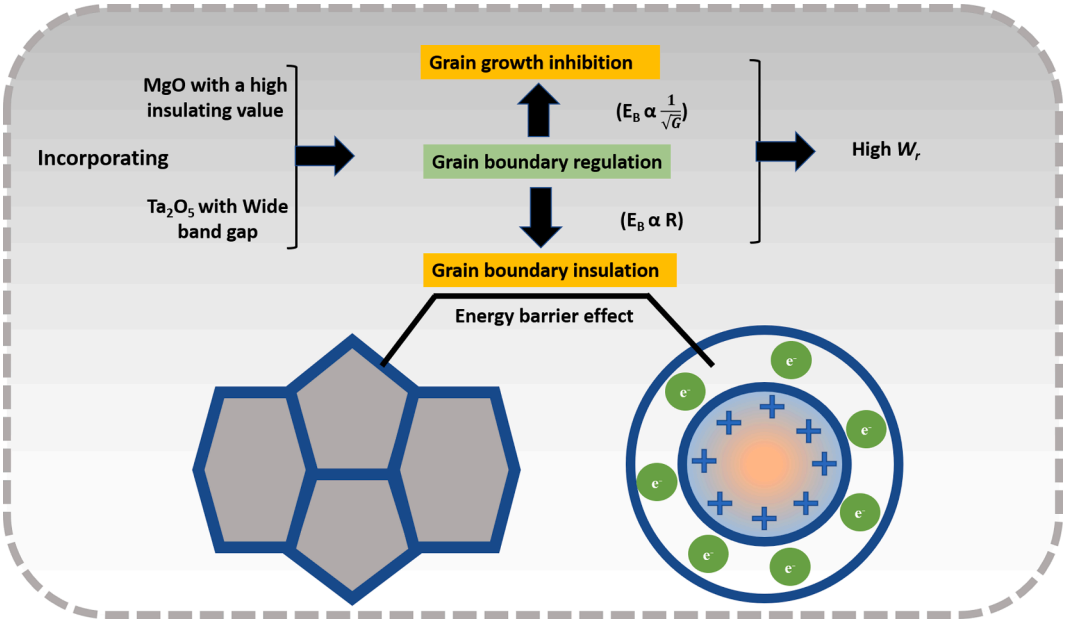

Fig. 14. Mechanism for superior energy storage properties using local random field theory [215].

5.4. Local random field strategy

Shi *et al.,* developed a new linear-like Pb-free 0.78$NaNbO_3$-0.22$Bi(Mg_{2/3}Ta_{1/3})O_3$ [NNO-BMT] RFE with ultrahigh recoverable energy density and efficiency via a local random field strategy [215]. Generally, a local random field is created to enhance the energy storage performance of a capacitor. The idea of this work was to improve the energy storage performance of NNO by the introduction of BMT through controlling the grain size and dielectric properties and the mechanism is shown in Fig. 14. The substitution of larger ionic radii $(Mg_{2/3}Ta_{1/3})^{3+}$ (0.68 Å) in the B-site of NNO [Nb^{5+} (0.64 Å)] led to hybridization between the Bi^{3+} 6p orbital and the O^{2-} 2p orbital, and consequently strengthens the polarization. Moreover, the low electronegativity at the B-site created by Mg^{5+} and Ta^{5+} promote the ionic bonding by generating a local electric field. This destroys the long-range ferroelectric order and a consequent decrease in the remnant polarization (P_r) [216]. Furthermore, a large dielectric breakdown strength, which is ascribed to the compact microstructure, small average grain size, increased grain boundary resistance, reduced leakage loss, interface polarization inhibition, and the presence of high dielectric insulator such as Ta_2O_5. Owing to the high insulation developed due to BMT, the grain boundary interferes the conduction mechanism. The small grain size promotes the accumulation of electrons at the grain boundaries, as the grain boundary density increases. Consequently, the moving charges under an external electric field get obstructed at the grain boundaries. This barrier effect offered by the grain boundary enhances *EB*. Furthermore, the wider band gap (E_g) of BMT prohibits the possibility of intrinsic breakdown. In summary, with this approach an ultrahigh W_r (~ 5.01 J/cm^3), η (~ 86.1 %) and an *EB* (~ 627 kV/cm) are obtained in the NNO-BMT ceramics. Moreover, the present NNO-BMT ceramic possess an ultrafast discharge rate ($\tau_{0.90}$ ~ 23 ns) and excellent fatigue stability even after 10^4 fatigue cycles.

5.5. Nano domain engineering

Nano domain engineering has recently attracted the attention of researchers in the development of quality energy storage capacitors [217]. In this regard, Qi *et al.*, developed a new type of RFE ceramic capacitor through nano domain engineering that exhibited a record-high energy storage performance. The fabrication technique involves the formation of $BiFeO_3$-$BaTiO_3$-$NaNbO_3$ [BFO-BTO-NNO] RFEs by integrating a high-spontaneous-polarization gene (BFO), a heterogeneous nano domain structure (BTO), and wide band gaps (NNO). The idea of manufacturing (0.67-x)BFO-0.33BTO-xNNO came up due to the drawback faced by the BFO-based solid solutions. Even though $BiFeO_3$ display giant $P_s \approx 100$ μC/cm^3 as compared to other Bi-based perovskites such as $(Bi_{0.5}Na_{0.5})TiO_3$ (BNT) and $Bi(Mg_{0.5}Ti_{0.5})O_3$ (<50 μC/cm^3), they exhibited a low dielectric breakdown strength. This is attributed to a relatively low band gap, large dielectric loss and high conductivity owing to the presence of volatile elements such as Bi and Fe during the sintering. On the other hand, the introduction of multivalent elements and liquid phases as sintering aids significantly improved the energy storage

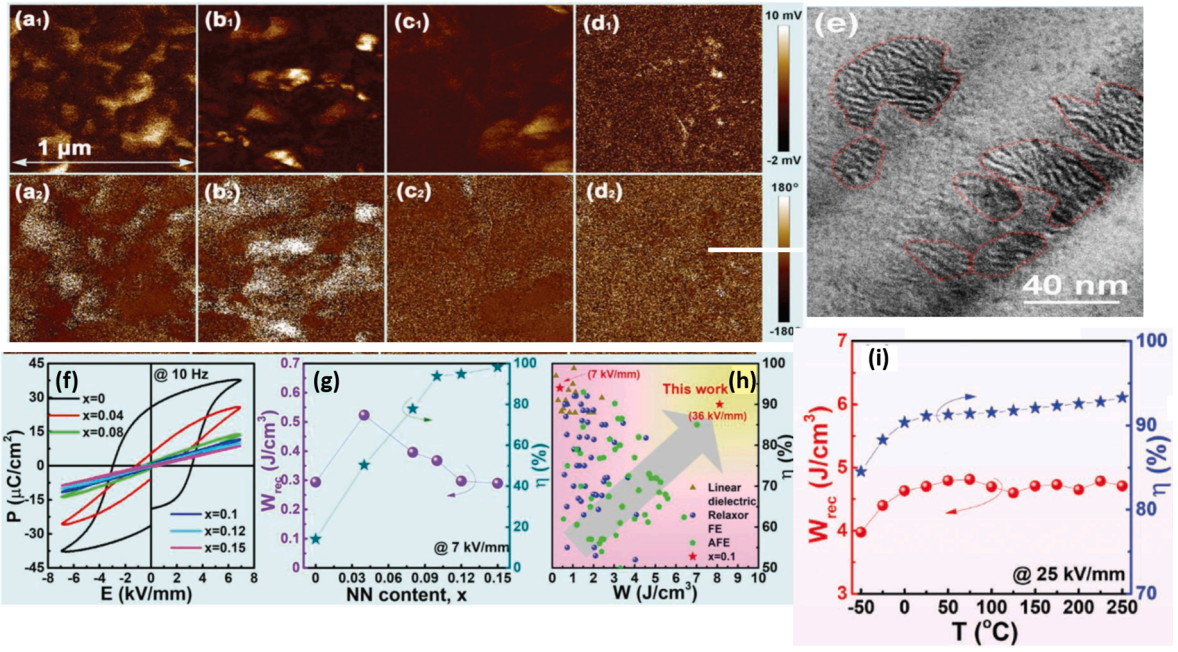

Fig. 15. Out-of-plane PFM amplitude (subscript 1) and phase (subscript 2) images of (0.67 – x)BFO-0.33BTO-xNNO ceramics; (e) HR-TEM image of randomly distributed PNRs in the BF matrix;, (f) room-temperature *P-E* loops; (g) W_r and η values measured under 7 kV mm^{-1} for (0.67 – x)BFO-0.33BTO-xNNO ceramics; (h) energy storage performance and its comparison with other bulk ceramics; (i) W_r and η values corresponding to the temperature ranging from −50 to 250 ^{0}C. Reprinted with permission from Qi *et al.*, Superior energy-storage capacitors with simultaneously giant energy density and efficiency using nanodomain engineered $BiFeO_3$-$BaTiO_3$-$NaNbO_3$ lead-free bulk ferroelectrics, Adv. Energy Mater. 1,903,338 (2019). Copyright (2019) by the Wiley-VCH. [https://doi.org/10.1002/aenm.201903338] [217].

density of BFO-based dielectric capacitors by enhancing their *EB*. From this point of view, Qi *et al.*, designed (0.67-x)BF-0.33BT-xNN ($0.1 \leq x \leq 0.15$) solid solutions by presuming that BTO having a stable phase structure and a high resistivity, and NNO with a larger band gap (E_g) could favor the energy storage performance of BF. Simultaneously, 0.1 wt% MnO_2 and 2 wt% $BaCu(B_2O_5)$ (BCB) were added into BF-BT-NN ceramics for inhibiting the $Fe^{3+} \rightarrow Fe^{2+}$ reaction and to optimize the sintering behavior.

Interestingly, an appreciable room temperature dielectric permittivity and a good thermal stability were obtained with the increase of NNO content. This is ascribed to the low temperature coefficient of permittivity and a nearly flat permittivity versus temperature curve. Furthermore, a dielectric relaxation behavior owing to a change in domain morphology as the × content is varied between $0.1 \leq x \leq 0.15$. This is further confirmed from the piezo force microscopy (PFM) image, since the amplitude of the PFM image give the strength of the piezoelectric response (Fig. 15(a)-(d)). The observed change from a long-range ordered FE domain with strong and clear contrast ($x = 0$) to an unclear contrast ($x \geq 0.1$) suggested a gradual decrease in the piezo response due to the interaction with local random field. This is attributed to the formation of PNRs and resulted an enhanced dielectric relaxation behavior. The *P-E* hysteresis loops exhibited a slimmer *P-E* loop with an increase in NNO content, which suggested a typical characteristic of an ergodic RFE ceramic (Fig. 15(e)). However, a nearly zero remnant polarization (P_r) ($x \geq 0.1$) is attributed to the low-hysteresis dielectric response as well as a quick reorientation capability due to the presence of PNRs. Furthermore, the BFO-BTO-NNO RFEs owns a fast-discharging speed under 200 kV/cm with a short discharge time of $\tau_{0.9} \approx 97$ ns. This fast-discharging speed is corroborated to the linear and a nearly hysteresis-free polarization response, which mainly arises from the ionic displacement. Moreover, the large E_B is ascribed to the decrease in grain size, increased band gap (E_g), and enhanced resistivity with increase in NNO content. In fact, the introduction of Ba (BTO) and Na (NNO) in BFO offers relatively smaller contribution to the polarization due to lack of orbital hybridization when compared with BFO. Consequently, the BTO - and NNO -rich regions in BFO disrupt the long-range ferroelectric order due to the formation of indistinguishable nano scale regions (PNRs). Further, a structural heterogeneity is created owing to the compositional inhomogeneity by BTO and NNO in the BFO matrix. Subsequently, the formation of a heterogeneous nanodomain structure, which are highly polarization sensitive to the applied electric field. Besides, the HR-TEM image of × = 0.1 showed a weak contrasted domain pattern suggesting the formation of randomly distributed stripe- like PNRs in the matrix [(Fig. 15(e))] [37]. Thus, the structure heterogeneity together with PNRs constituted the enhanced energy storage performance in BFO-BTO-NNO ceramics. In this way, Qi *et al.*, developed the BFO-BTO-NNO RFEs exhibiting a room temperature giant $W_r \approx 8.12$ J/cm^3, $\eta \approx 90$ % and an outstanding energy discharge speed at $x = 0.1$ compared to other Pb-free ceramics (Fig. 15(f)-(h)). Furthermore, a desirable W_r ($\approx 4.40 \pm 0.44$ J/cm^3) and η (>85 %) is achieved in the temperature ranging from − 50 to 250 ^{0}C (Fig. 15(i)). These results demonstrate that the BFO–BTO–NNO RFE solid-solution ceramics can be considered as potential lead-free dielectrics for next-generation pulsed power capacitors.

5.6. Layer by layer engineering

Layer-by-layer engineering is a new strategy implemented to develop energy storage capacitors via coupling a FE with RFEs for achieving very good energy storage density through enhancing the dielectric breakdown strength of the capacitors (Fig. 16(a)) [218]. In this work developed by Cai *et al.*, a layer by layer structure comprising $BaTiO_3$ doped with Al_2O_3 (3 wt%) and SiO_2 (1 wt%) (BTAS) as FE and $0.87BTO–0.13Bi(Zn_{2/3}(Nb_{0.85}Ta_{0.15})_{1/3})O_3$ (BTBZNT) as RFE were designed. This work reported a very good W_r 5.04 J/cm^3

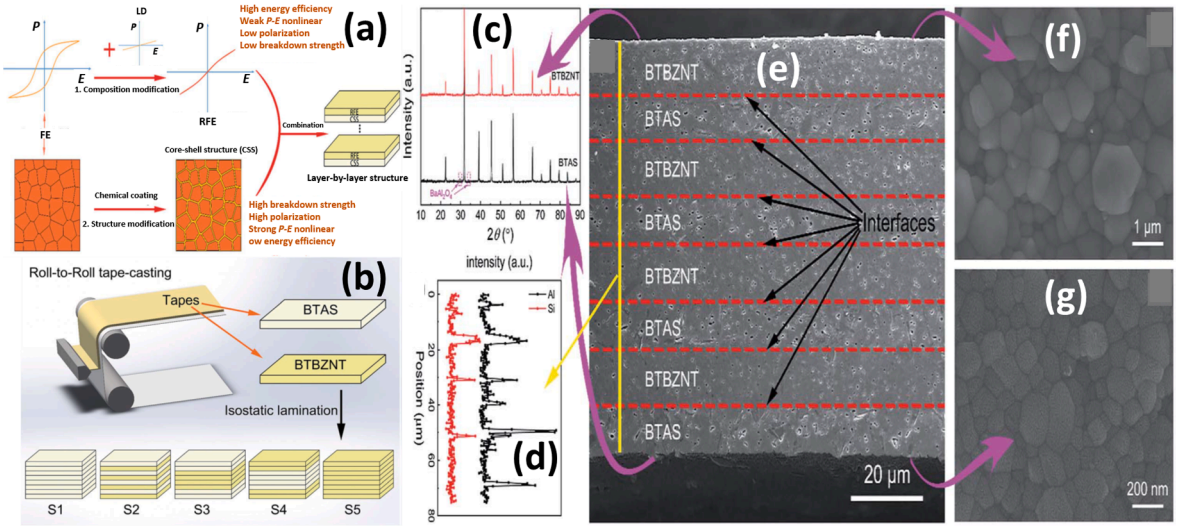

Fig. 16. Schematic representation of (a) layer by layer structured ceramics and (b) roll-to-roll tape-casting method; (c)-(d) XRD of sample S2; (e)-(g) shows the SEM image of sample 2 confirming the alternative parallel arrangement of four BTBZNT layers and four BTAS layers Reprinted with permission from Cai *et al.*, Giant dielectric breakdown strength together with ultrahigh energy density in ferroelectric bulk ceramics via layer-by-layer engineering, J. Mater. Chem. A 7, 17283–17291 (2019). Copyright (2019) by the Royal Society of Chemistry. [https://doi.org/10.1039/C9TA05182A] [218].

and a η 68 %, with an exceptionally good E_B 790 kV/cm. An advanced roll-to-roll tape-casting method as depicted in Fig. 17(b) is used to prepare the BTAS layer with thickness of 13 mm and BTBZNT layer with thickness of 17 mm. Then, these layers were arranged to form a layered structure via isostatic lamination to form different ceramic layers denoted in Fig. 16(b). A two-step sintering approach is followed to increase the density as well as the fusing between the BTAS and BTBZNT layers. The microstructure characterization of S2 shows a typical layer-by-layer structure BTBZNT layer and BTAS layer can be clearly identified (Fig. 16(c)-(g)). The capacitor designed in this way showed an excellent E_B, as the layer-by-layer structure promotes the redistribution of local electric field. A high E_B is achieved due to the low permittivity of BTAS layer, which enhances the breakdown strength via slowing down the fast propagation of the breakdown path. Furthermore, the interfaces between the two layers act as a branching for the breakdown paths by dissipating more energy. Consequently, an enhancement in the E_B with an improved energy storage density is obtained.

5.7. Multilayer ceramic capacitors

In recent years, the RFEs based multi-layered ceramic capacitors (MLCC) are receiving greater attention in the field of energy storage capacitor applications due to their impeccable energy storage density and fast discharging speed [32,219–221]. The fabrication of MLCCs consists of four stages, which includes the ball milling, slurry formation, tape casting, and lamination [222,223]. The schematic representation of the MLCC capacitor fabrication process is shown in Fig. 17. At first, the calcined powder is mixed with ethyl methyl ketone solvent and then, ball-milled in the presence of a binder (poly(propylene carbonate)) and a plasticizer (butyl benzyl phthalate). Using a tape caster with a single doctor blade, the slurry was poured onto a silicon coated polyethylene terephthalate (PET) carrier film (substrate). The cast slurry was then dried for 1 h at room temperature to get the ceramic tapes. After drying, platinum (Pt) was printed on each ceramic tape as electrode. Finally, the ceramics tapes are coated with Pt internal electrodes and sintered at desired temperatures (in order to burn out organic ingredients) for the subsequent formation of the MLCCs. Using this method, Wang *et al.*, developed a 0.75($Bi_{0.85}Nd_{0.15}$)FeO_3-0.25$BaTiO_3$ MLCC consisting of 9 active layers with a total thickness of the multilayers 0.78 mm (each sintered layer possess a thickness 32 mm) and is shown as inset in Fig. 18(a) [220]. The energy storage calculation of the multilayers from the *P-E* loops showed a high W_r 6.74 J/cm^3 with an efficiency 77 % at 647 kV/cm and were stable up to 125 ^{0}C (Fig. 18(b)-(d)). Moreover, these MLCCs showed a discharging time<4 μs ($\tau_{0.9}$).

Further, the combination of different strategies like controlled chemical homogeneity and two-step sintering in a MLCCs were also implemented in achieving high energy storage performance. In 2019, Wang *et al.*, designed (0.7-x)BFO-0.3BTO-xNd($Zn_{0.5}Zr_{0.5}$)O_3 (BFO-BTO-NZZ) based MLCCs through multilayers by controlled electrical homogeneity [221]. The authors fabricated multilayer ceramic capacitor as shown in Fig. 19(a)-(c). The electrical homogeneity plays a critical role in optimizing the breakdown strength. This is due to the fact that the electrically homogenous insulators dodge the possibility of breakdown at high field through an increased resistivity, reduced grain size and low porosity. As a result, the BFO-BTO-NZZ multilayers exhibited a higher $W_r = 10.5$ J/cm^3, $\eta = 87$ % and a superior $E_B = 700$ kV/cm (Fig. 19(d)-(e)). In fact, the BF-BT-NZZ MLCCs exhibited an exceptional temperature withstanding capability (variation of 15 %) in the range 25 to 150 ^{0}C (Fig. 19(f)-(g)), making them appropriate for real-time applications.

On the other hand, Cai *et al.*, fabricated a high performance Pb-free 0.87BTO–0.13Bi($Zn_{2/3}$($Nb_{0.85}Ta_{0.15}$)$_{1/3}$)O_3 (BTO–BZNT) RFE

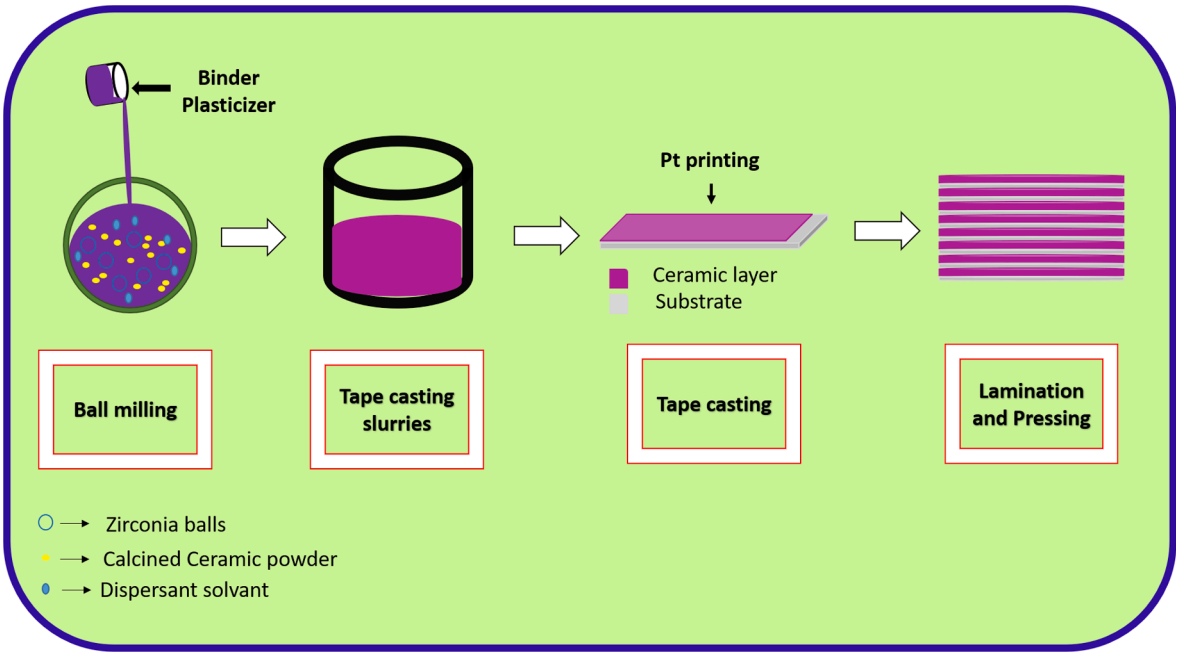

Fig. 17. Schematic representation of the fabrication of MLCCs.

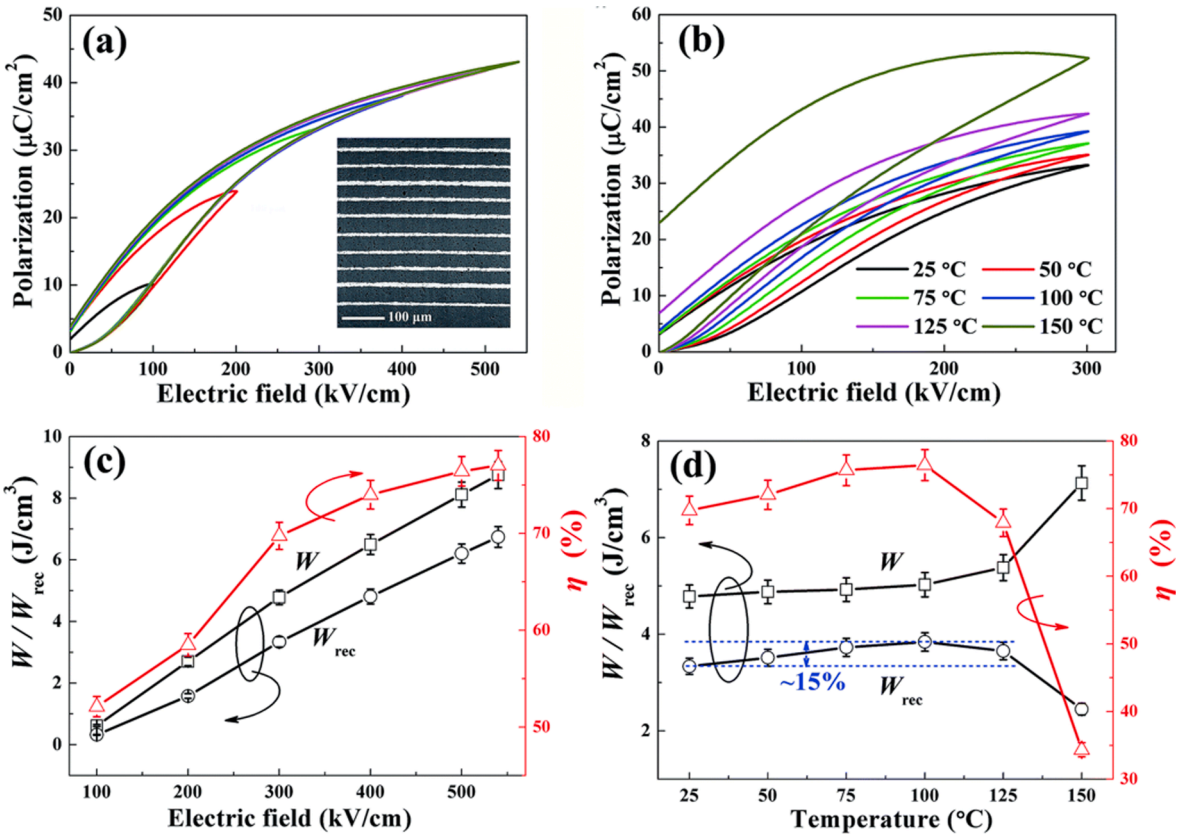

Fig. 18. Unipolar P-E loops of multilayers at (a) room temperature (RT) with varying electric fields and (b) different temperatures at a constant electric field of 300 kV/ cm; energy storage performance at (c) RT with different electric field and (d) various temperatures at 300 kV/ cm; the inset in (a) shows the SEM image of the multilayers. Reprinted with permission from Wang *et al.*, Bismuth ferrite-based lead-free ceramics and multilayers with high recoverable energy density, J. Mater. Chem. A 6, 4133–4144 (2018). Copyright (2018) by the Royal Society of Chemistry. [https://doi.org/10.1039/C7TA09857J] [220].

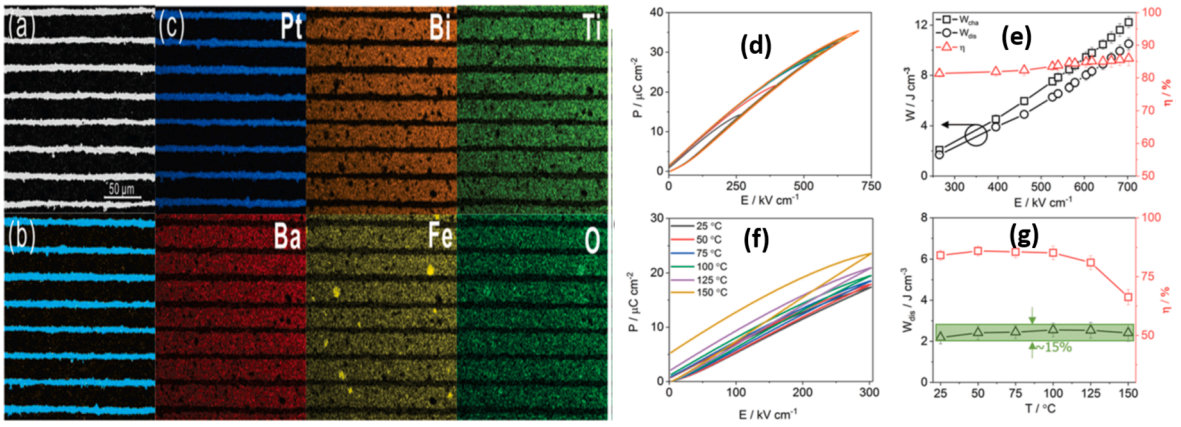

Fig. 19. (a) Cross sectional backscattered electron image, (b) EDX spectra showing overlapping of all elements, and (c) Elemental mapping in × = 0.08 multilayers; (d) unipolar *P-E* loops and (e) energy storage properties as a function of electric field at room temperature; (f) unipolar *P-E* loops and (g) energy storage performance at temperature ranging from 25 to 150 ^{0}C. Reprinted with permission from Wang *et al.*, Ultrahigh energy storage density lead-free multilayers by controlled electrical homogeneity, Energy Environ. Sci. 12, 582–588 (2019). Copyright (2019) by the Royal Society of Chemistry. [https://doi.org/10.1039/C8EE03287D] [221].

based MLCC [224]. Since Pt is very costly, Cai *et al.*, introduced a combination of both silver and palladium (60Ag/40Pb) as the internal electrodes to reduce the cost and for assuring the co-sintering of the dielectric ceramic and the metal electrodes. Thus, Cai *et al.*, designed the BT-BZNT MLCCs consisting of 10 ceramic layers. Each ceramic layer is 11 μm thick with electrodes having an effective area 2.7 mm × 3.2 mm. The MLCCs followed three heating rates namely, 4 ^{0}C/min (MLCC-4), 20 ^{0}C/min (MLCC-20), 40 ^{0}C/min (MLCC-40), and their corresponding SEM images are shown in Fig. 20(a)-(c). At the time of first-step sintering, the density of the dielectric layer (BT–BZNT) is improved by a significant reduction in the grain size. However, the dielectric layers of MLCC-40 sintered via the two-step heating rate i. e. 40 ^{0}C/min, showed no clear pores as shown in Fig. 20(d)-(f) due to the formation of low-melting liquid alloy layer at electrode interface under tension. Such an interfacial liquid alloy layer formed by the fast-heating rates offers better metal electrode continuity and consequently, an improvement in energy storage performance is obtained through enhanced *EB*. This work reported a $W_r = 8.13$ J/cm^3 with a dielectric breakdown strength of 750 kV/cm and an ultrahigh efficiency of 95 % (Fig. 20 (g)-(h)).

Recently in 2020, Wang *et al.*, studied the energy storage performance of $0.87BaTiO_3$-$0.13Bi(Zn_{2/3}(Nb_{0.85}Ta_{0.15})_{1/3})O_3$ (BTBZNT) MLCCs via two-step sintering by varying the thickness of the dielectric layers (*D*) from 26 to 5 μm [225]. This work reported a superior discharging energy storage proeprties with $W_r = 10.5$ J/cm^3, $\eta = 93.7$ % and an excellent $E_B = 1047$ kV/cm in BTBZNT MLCCs with $D \sim 9$ μm (Fig. 21(a)-(b)). Further, the MLCCs exhibited an excellent thermal stability with a discharge energy density variation $< \pm 5$ % over a wide range of temperature from − 50 to 175 ^{0}C under an electric field of 400 kV/cm (Fig. 21(c)). Very recently, Ji *et al.*, in 2021 reported a high W_r (~18 J/cm^3) and η (93) in $0.62Na_{0.5}Bi_{0.5}TiO_3$ $-0.3Sr_{0.7}Bi_{0.2}TiO_3$ $-0.08BiMg_{2/3}Nb_{1/3}O_3$ (BNT-SBT-0.08BMN) MLCCs, at an electric field of 1013 kV/cm [226]. Thus, MLCCs displays exceptional energy storage performance with a very good thermal stability suitable for high power-high temperature applications.

6. Energy storage performance in RFE based films

As we already discussed in the previous section, the Pb-free RFE based ceramic systems are receiving greater interest as energy storage capacitors owing to their excellent dielectric breakdown strength. However, the real world demands the miniaturization of electronic devices such as military artillery, hybrid electric automobiles, smart and wearable electronics, etc [227–229]. Therefore, the film-based capacitors are more attractive for the miniaturization of electronic devices than bulk ceramics [213–215]. Most importantly, the E_B of the film capacitors are exceptionally higher when compared to the bulk ceramics and thereby provide superior energy storage density [33]. Even though the breakdown strength of the RFE based ceramics capacitors is very much high compared to the normal dielectric capacitors like LD, FE, and AFE, yet the RFEs based ceramics face a limitation in providing a breakdown strength in the range of MV for high power applications [35]. On the other hand, the film (either thick or thin) based capacitors can be considered as ideal candidates for miniaturized device applications owing to their dense and pore free microstructure. Further, the thickness of the

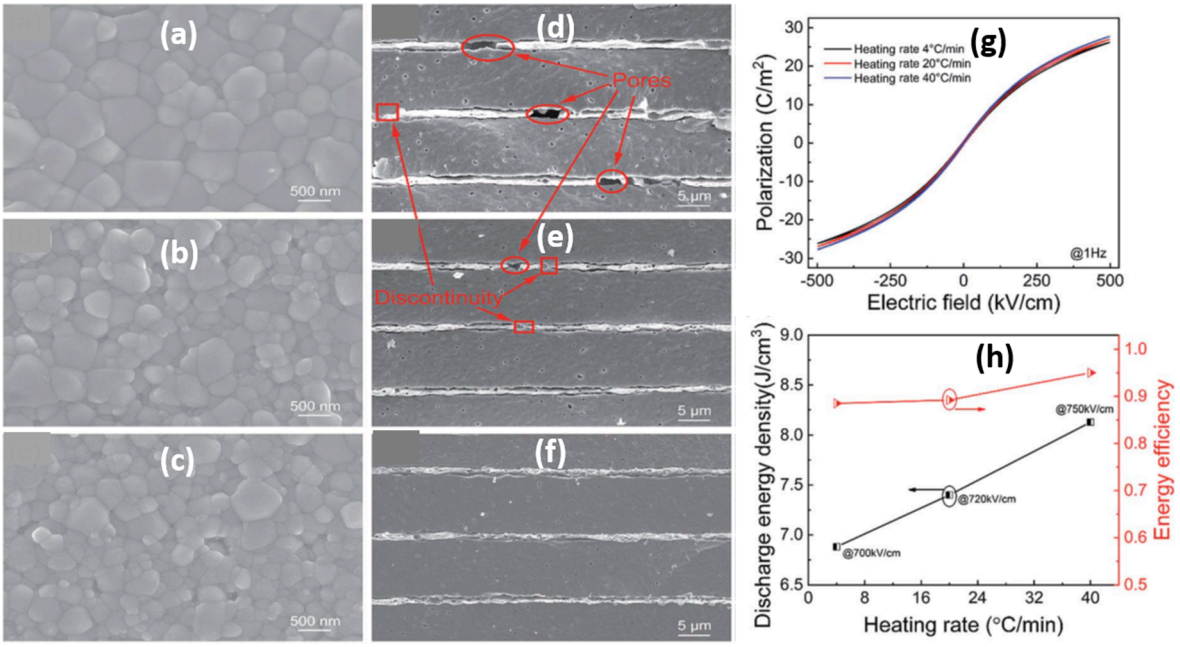

Fig. 20. (a)-(c) Surface SEM images of the MLCCs sintered at a rate of 4, 20, and 40 ^{0}C/ min respectively; (d)-(f) cross-sectional SEM images of 4, 20, and 40 ^{0}C/ min respectively; (g) P-E loops of MLCCs at an electric field of 500 kV/cm at 1 Hz; (h) energy storage performance at various heating rates. Reprinted with permission from Cai *et al.*, High-temperature lead-free multilayer ceramic capacitors with ultrahigh energy density and efficiency fabricated via two-step sintering, J. Mater. Chem. A 7, 14575–14582 (2019). Copyright (2019) by the Royal Society of Chemistry. [https://doi.org/10.1039/C9TA04317A] [224].

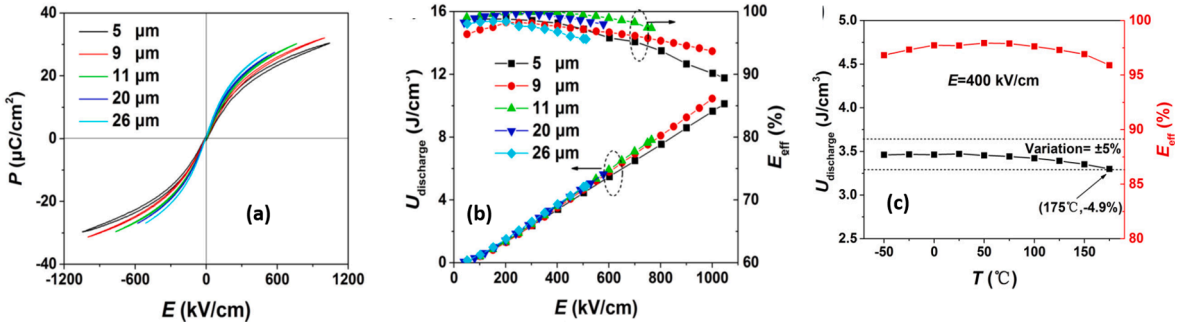

Fig. 21. (a)-(b) Hysteresis loops and discharge energy of the BTBZNT MLCCs with different D values; (c) temperature dependence of W_r and η of BTBZNT MLCC with $D \sim 9$ μm. Reprinted with permission from Wang *et al.*, Effects of dielectric thickness on energy storage properties of $0.87BaTiO_3$-$0.13Bi(Zn_{2/3}(Nb_{0.85}Ta_{0.15})_{1/3})O_3$ multilayer ceramic capacitors, J. Eur. Ceram. 40, 1902–1908 (2020), Copyright (2020) by the Elsevier ltd. [https://doi.org/10.1016/j.jeurceramsoc.2020.01.032] [225].

dielectric material is a key factor that determines the breakdown strength. This is due to the fact that the energy stored in a film capacitor is controlled by its thickness to volume ratio. As the thickness is reduced to a critical value, the dielectric films display an exceptionally high energy storage performance owing to their dielectric strength which becomes independent of dimension and acts as an inherent property. As a consequence, a superior energy storage performance ascribed to a very high breakdown strength. Moreover, such a superior E_B not only offers a wider range of safe operating voltages but also lower the probability of irreversible device failure in the dielectric capacitors [33,34].

Different deposition techniques such as sol–gel, spin coating, chemical solution deposition (CSD), pulsed laser deposition (PLD), ion-beam sputtering deposition, rf-sputtering, laser molecular epitaxy (LME), etc. have been employed to fabricate RFE based dielectric ceramic films on different substrates for the designing of energy storage capacitors [230–252]. Table 2 summarizes the best performing RFE based thin film capacitors. For instance, in 2019 Pan *et al.*, reported a new type of RFE based (0.55-x)BFO-xBTO-0.45STO (denoted by BFBSTO, x = 0.0 to 0.4) films [230]. However, in normal RFEs, the polarization is weakened either by rhombohedral (R) or tetragonal (T) nanodomains. Here, Pan *et al.*, introduced the polymorphic nanodomain (R and T nanodomains with cubic matrix) in RFEs to achieve high polarization and low loss (Fig. 22(a)). In this regard, the BFO and BTO were chosen to introduce R and T ferroelectric phases, while STO was incorporated to hinder the long-range FE order and to induce nanodomains. The high-angle annular dark field (HAADF) Z-contrast STEM studies revealed that all nanodomains for × = 0 was in R-phase (Fig. 22(b)-(d)), whereas BFBSTO films with × = 3 showed both R-phase and *T*-phase nanodomains (Fig. 22(e)-(h)). Usually, the fatigue in FE is ascribed to the domain wall pinning by the defects during repeated polarization switching caused by the macroscopic domains. However, these macroscopic domain walls are eliminated and form highly dynamic polymorphic nanodomains in RFE BFBSTO films. This will suppress the defect pinning and result in the good fatigue endurance in the RFE BFBSTO films ($> 10^8$ cycles). Further, the statistical Weibull distribution analysis suggested an increase in the β from 12 (x = 0.0) to 25 (x = 0.3) (Fig. 22(i)). Consequently, an improvement in the *EB* value from 3.2 MV/cm (x = 0.0) to 4.9 MV/cm (x = 0.3). Thus, the work reported a very high W_r of 112 J/cm^3, a high η of 80 % and an excellent *EB* of 4.9 MV/cm (Fig. 22(j)). This is attributed to the enhanced relaxor behavior by eliminating the macroscopic domain walls and the formation of polymorphic nanodomains. Further, the enhanced breakdown strength arises from the BTO content, which improves the insulator behavior by restricting the carrier emission, increasing the band gap, and providing high chemical stability. This obstructs the formation of defects such as oxygen vacancies and suppresses the leakage current and thus, a very high energy storage performance is obtained.

In the same year, a high energy storage performance was reported in the RFE BZCT by coupling it with a low permittivity HfO_2: Al_2O_3 (HAO) layer. As a result, an impressive energy storage performance with a $W_r = 99.8$ J/cm^3, $\eta = 71$ %, and EB = 750 kV/cm, was achieved [231]. This is attributed to the strong charge coupling caused by the HAO dielectric layer, which not only enhanced the polarization value but also led to a slim *P-E* loop. Recently, in 2020 Lv *et al.*, developed flexible RFE-based thin film dielectric capacitors with a multilayered structure consisting $(Na_{0.8}K_{0.2})_{0.5}Bi_{0.5}TiO_3$ and $Ba_{0.5}Sr_{0.5}(Ti_{0.97}Mn_{0.03})O_3$ (NKBT/BSMT) [232]. Lv *et al.*, synthesized the NKBT/BSMT multilayered films on a mica substrate through different stacking arrangements with a fixed total thickness (Fig. 23(a)-(d)). The NKBT/BSMT exhibited a very high W_r 91 J/cm^3 with a high *EB* 3.035 MV/cm (Fig. 23(e)-(f)). Moreover, the NKBT/BSMT showed a very good charging–discharging speed of 47.6 μs. Such features make them attractive for the development of flexible micro energy storage systems. This is ascribed to the relaxor-like characteristics with broadened dielectric peaks and strong frequency dispersion feature owing to the formation of nanodomains. Further, these nanodomains promotes a fast-reversible polarization switching and thereby a high energy storage density. Besides, a strong restoring capability by the nano-sized domains is very common in RFE films [232].

Further, Chen *et al.,* reported a record high energy storage density in the RFE heterostructure composed by P-type $Na_{0.5}Bi_{3.25}La_{1.25}Ti_4O_{15}$ (P-NBLT) and *N*-type $BaBi_{3.4}Pr_{0.6}Ti_4O_{15}$ (*N*-BBPT) layers fabricated through sol–gel method [244]. In this PNP-type heterostructure films, the W_r is enhanced through increasing the depletion layer width owing to the motion and recombination of majority charge carries in the applied electric field. As a consequence, the depletion regions experience a high resistance state. This increases the insulation characteristics and the EB. The PNP heterostructure exhibited a superior W_r of 159.7 J/cm^3 and an efficiency of

Table 2
Energy storage properties reported for various RFE films.

Material	Fabrication method	Substrate	Film thickness (nm)	W_r (J/cm^3)	E_B (MV/cm)	η (%)	Ref no
0.25BFO-0.30BTO-0.45STO	PLD	ST single-crystal	200–800	112	4.900	80	[230]
Mn:NBT-BT-BFO	CSD	Pt/F-Mica	350	81.9	2.285	64.4	[234]
Mn:NBT-BT-0.45ST	CSD	Pt/F-Mica	–	76.1	2.813	80	[235]
$Ba(Zr_{0.35}Ti_{0.65})O_3$	Sputtering	LSMO/STO/F-Mica	30	65.1	6.150	72.9	[236]
$(BiFeO_3)_{0.25}(BaTiO_3)_{0.75}$	PLD	ST single-crystal	350	80	3.100	78	[239]
BST–BMN	PLD	NbSTO	400	86	5.000	73	[241]
0.3BFO-0.7SBT		Pt/F-Mica		61.5	3.000	75.4	[240]
NKBT/NKBT-ST	DC sputtering	Pt/F-Mica	20	73.7	3.077	68.1	[243]
P-NBLT/*N*-BBPT	Sol-gel	–	500	159.7	3.450	70	[244]
NKBT/BSMT	DC sputtering	Pt/F-Mica	280	91	3.035	68	[232]
BST/BT-BMZ	RF sputtering	Nb/STO single crystal	230	87.26	7.900	61.05	[249]
$(Ba_{0.95}, Sr_{0.05})(Zr_{0.2},Ti_{0.8})O_3$	RF sputtering	$Pt/Ti/SiO_2/Si$	300	102	6.2	87	[253]
Sm-0.3BCZT-0.7BFO	PLD	Nb/STO single crystal	650	152	3.5	>90	[254]

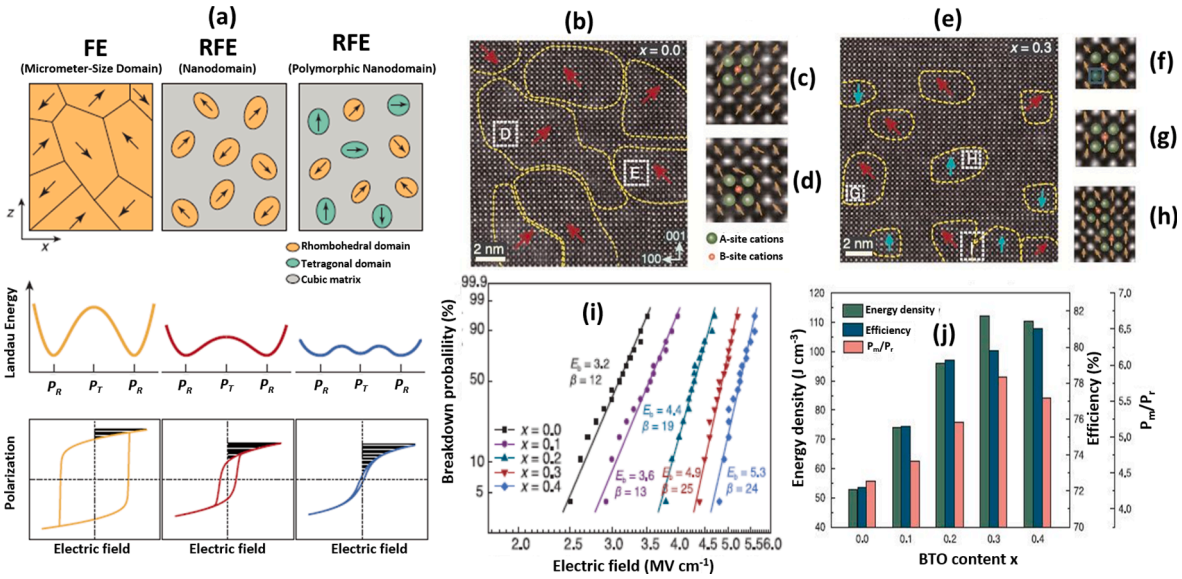

Fig. 22. (a) Diagrammatic representation of Landau energy profiles and P-E loops of different nanodomains. The polarization states along the rhombohedral (R) [111] and [111] directions are represented using P_R, while P_T along the intermediate tetragonal (T) [001] direction. The energy density is represented by the shaded region in the P-E loops; (b)-(h) HAADF STEM images for × = 0 and × = 0.3, respectively. The yellow dashed lines delineate the nanodomains, with the projected B-site cation displacements denoted by red (⟨111⟩ R) and cyan (⟨001⟩ T) arrows. (D and E) represents the magnified images of selected areas from (b) and (G to I) corresponds to the magnified images from (c) to show the cation displacements. The olive and pink spheres represent A-site and B-site cations, respectively. The dark yellow arrows show the B-site cation displacement vectors in each unit cell; (i) Weibull distribution and dielectric breakdown strength of BFBSTO films; (j) energy storage performance in various BFBSTO films. Reprinted from Pan *et al.*, Ultrahigh–energy density lead-free dielectric films via polymorphic nanodomain design, Science. 365, 578–582 (2019), Copyright (2019) by the Science [https://doi.org/10.1126/science.aaw8109] [230]. (For interpretation of the references to colour in this figure legend, the reader is referred to the web version of this article.)

70 %. Recently in 2020, Silva *et al.*, reported that Pb-free ZrO_2 binary oxide films are potential candidates for the fabrication of energy storage capacitors by coupling them with a low permittivity HfO_2:Al_2O_3 (HAO) layer of different thickness [250]. The insertion of HAO layer improved the interfacial polarization and consequently, amended the ferroelectric as well as discharging energy density of the ZrO_2 films. The XRD shows a decrease in intensity of the ZrO_2 peaks with increasing the HAO layer thickness (Fig. 24(a)), while the HRTEM studies confirm the orthorhombic phase of ZrO_2 (Fig. 24(b) – (f)). Further, the ferroelectric nature in ZrO_2 is attributed to the presence of orthorhombic phase. Moreover, the depolarization induced by the HAO layer in ZrO_2 resulted in a slim and slant *P-E* loops (Fig. 24(g)). Hence, the HAO (2 nm)/ZrO_2 film capacitor exhibited a higher W_r of 54.3 J/cm^3 when compared to 9.2 nm thick $Hf_{0.3}Zr_{0.7}O_2$ film capacitor and 2.0 % La-doped HfO_2-ZrO_2 (10 nm thickness) based film capacitors [229,230]. In addition, the HAO (2 nm)/ZrO_2 capacitor displayed a good fatigue free behavior > 10^9 cycles with just ~ 10 % degradation of energy storage performance (Fig. 25(h)).

Recently, designing superparaelectric (SPE) strates in RFEs emerges as a promising but scarcely explored approach. Usually,

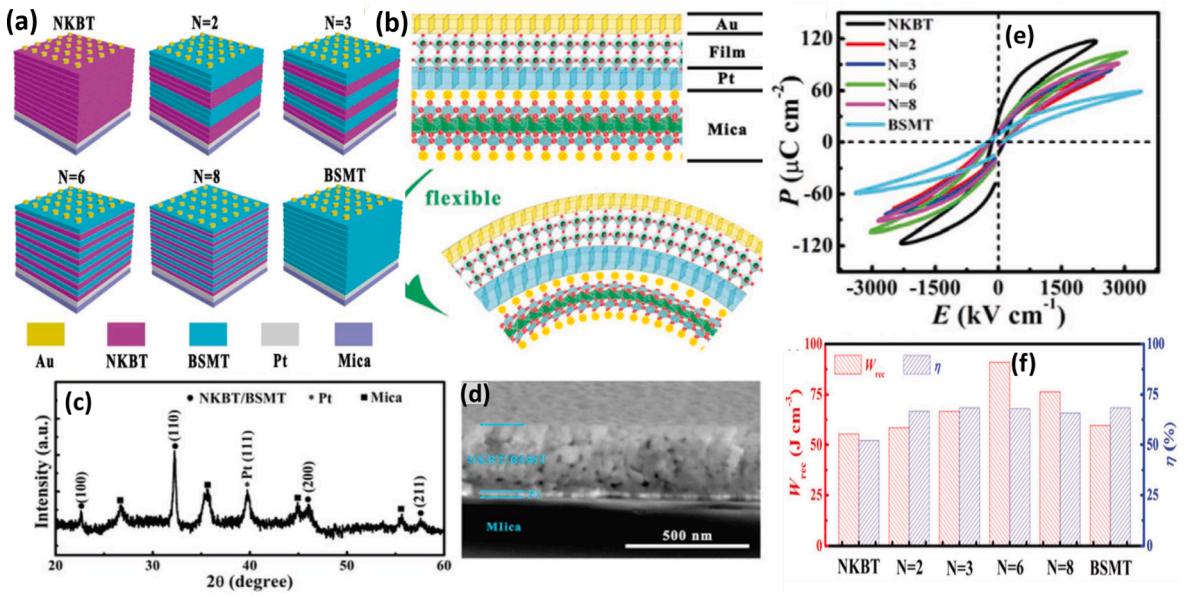

Fig. 23. (a) Diagrams of NKBT, BSMT, and NKBT/BSMT multilayer films of repeated periods, N = 2, 3, 6, and 8 with the same total thickness. (b) representation of heterostructure film under flat and bending states; (c) XRD pattern of N = 6 film on Pt/mica substrate and (d) depicts the cross-sectional SEM image; (e) room temperature *P-E* hysteresis loops; (f) W_r and η values of NKBT/BSMT films. Reprinted with permission from Lv *et al.*, Flexible lead-free perovskite oxide multilayer film capacitor based on $(Na_{0.8}K_{0.2})_{0.5}Bi_{0.5}TiO_3/Ba_{0.5}Sr_{0.5}(Ti_{0.97}Mn_{0.03})O_3$ for high-performance dielectric energy storage. Adv. Energy Mater. 2020, 1904229, Copyright (2019) by the Wiley-VCH. [https://doi.org/10.1002/aenm.201904229] [232].

superparaelectricity arises when the ferroic long-range order in nanoclusters is incomplete. The nanodomains in the SPEs are further scaled down and consequently domain inter-coupling is become weaker to a level that the energy required for domain switching is comparable with or below the thermal disturbance energy kT (k is the Boltzmann constant). Hence, the polarization of nanodomains can flip among energy equivalent directions with high dynamics, which makes it possible to realize $P_r \sim 0$ and a non-hysterical *P–E* curve [253,254]. Through the SPE approach, $(Ba_{0.95}, Sr_{0.05})(Zr_{0.2},Ti_{0.8})O_3$ thin films integrated on Si exhibit an W_r of 102 J/cm^3, an efficiency of 87 %, are fatigue-free after 2×10^9 cycles and can endure a harsh temperature environment [253]. More recently, Pan et al. achieved an ultrahigh W_r of 152 J/cm^3 with an efficiency > 90 % at an electric field of 3.5 MV/cm in SPE Sm-doped 0.3BCZT-0.7BFO, with Sm content of 0.45 [254].

7. Summary and future scopes

The energy storage components become an essential part of human world in day-to-day life to operate basic electronic gadgets to warfare technologies. Consequently, the development of new sustainable energy storage technologies for a healthier future is always essential. In this context, the dielectric capacitors mark their signature as a vital component in the energy storage devices starting from the basic mobile phone technology to the most modern advanced pulsed power technology. This article highlighted the recent advances in the development of RFE based systems for the application in energy storage devices. The review starts with a contextualization of RFEs materials in the dielectrics class of materials and highlights their main advantages. Then, the history of RFEs and the current progress in RFEs as energy storage capacitors are discussed in detail. We cover most of the Pb-free RFE based ceramic systems as well as thin films and, discussed some of the recently adopted strategies for enhancing the energy storage properties of RFEs. This includes doping, microstructure tailoring, semiconductor/relaxor 0–3 type composites, local random field strategy, layer-by-layer engineering, nano domain engineering, composition design, and multi-layer ceramic capacitors (MLCCs). Interestingly, it is possible to conclude that each individual strategy allows to obtain an energy storage density higher than the one obtained in the best commercial dielectric capacitor, the bulky biaxially oriented polypropylene (BOPP), which has a low energy storage density < 7 Jcm^{-3}. More specifically, by using the MLCC strategy an energy storage density > 10 J/cm^3 was already achieved with a reduced temperature effect up to 170 ^{0}C. Thus, the possible replacement of the BOPP by a RFEs is becoming a reality, which can help us to overcome most of the disadvantages presented by it in several applications. For instance, in a HEV its substitution allows removing the extra cooling system, which will reduce the weight, volume, and complexity in the design of the power systems, conferring to the HEV more autonomy making it even more attractive for the consumer. Further, the faster discharge time (in the ns range) of RFEs when compared to BOPP (in the μs range) make them very promising for PPT. Moreover, the PPT demand capacitors that can provide a stable operation condition in the range 125 ^{0}C – 180 ^{0}C [22]. Besides, there are other advanced areas of interest, which required the materials that can provide a good thermal stability and energy storage performance [22].

Still the BOPP cannot meet the requirement of high thermal stability. On the other hand, the RFE bulk ceramics are capable of

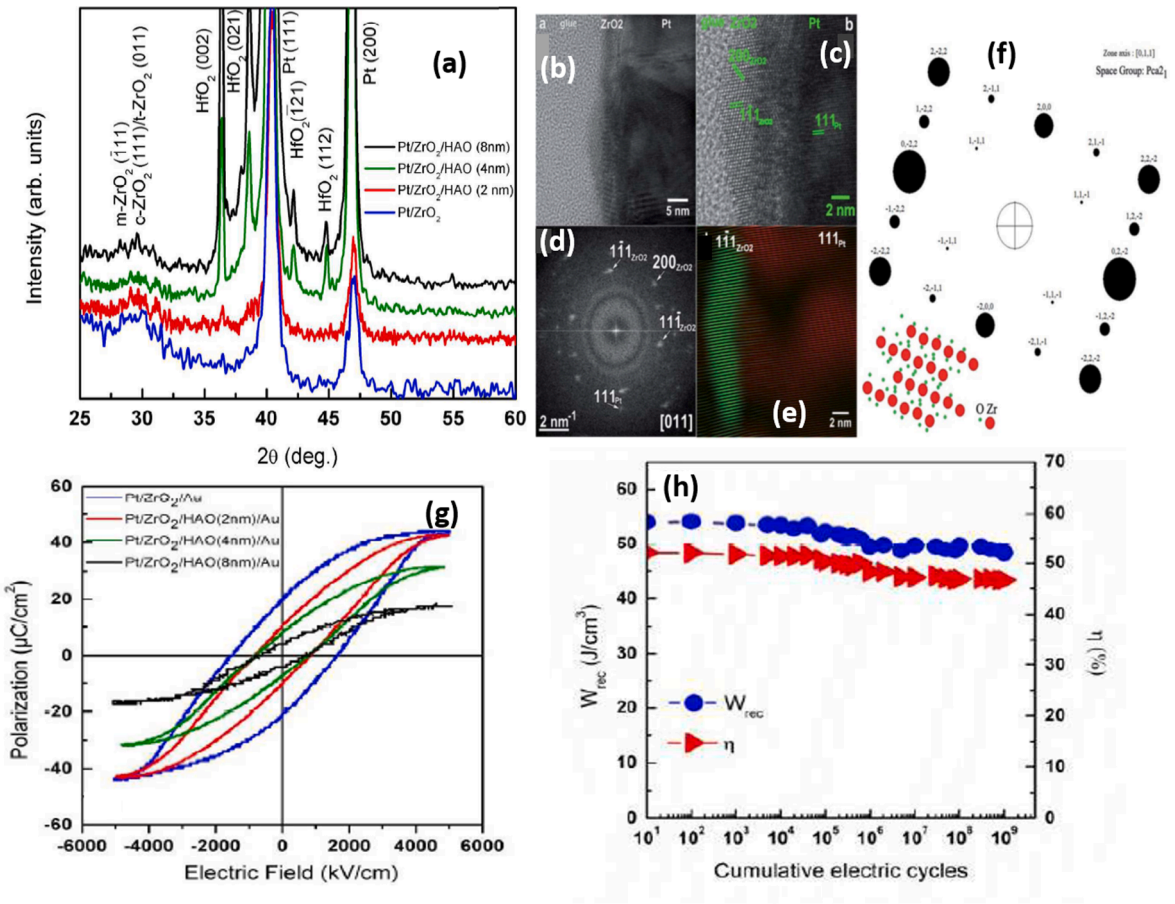

Fig. 24. (a) Structural analysis of Pt/ZrO_2 and Pt/ZrO_2/HAO films using XRD; (b)-(c) cross sectional HRTEM images of the Pt/ZrO_2 films; (d)-(e) represents the fast fourier transform (FFT) pattern image and (e) filtered FFT image, respectively of the HRTEM image; (f) simulated SAED pattern and atomic structural model of ZrO_2 films. (g) Hysteresis loops of ZrO_2 and HAO/ZrO_2 film capacitors; (e) W_r and η in HAO(2 nm)/ZrO_2 films as a function of cumulative electric field cycles. Reprinted with permission from Silva *et al.*, Energy storage performance of ferroelectric ZrO_2 film capacitors: effect of HfO_2:Al_2O_3 dielectric insert layer, J. Mater. Chem. A, 2020, **8**, 14171–14177, Copyright (2020) by the Royal Society of Chemistry [https://doi.org/10.1039/D0TA04984K] [250].

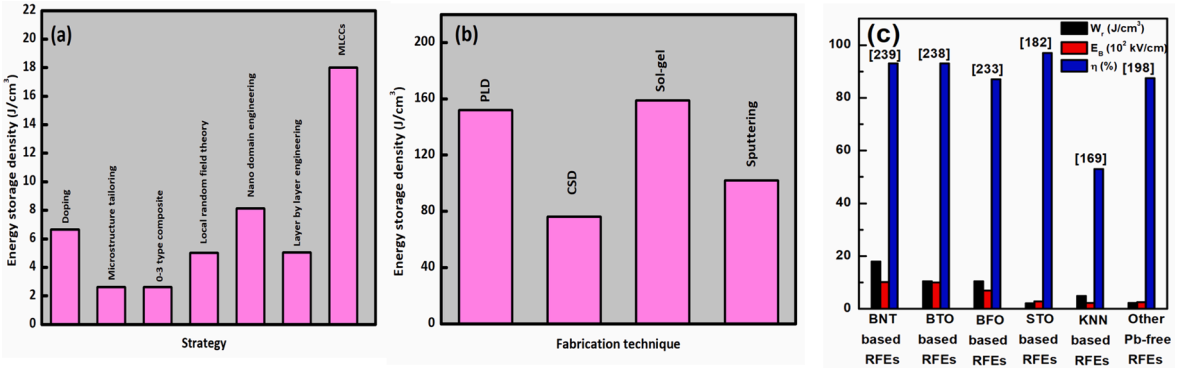

Fig. 25. Energy storage density (a) as a function of strategy for RFEs based bulk ceramic capacitors [110,155,176,178,193,202,207,213,217,218,226], (b) as a function of fabrication technique for RFEs based ceramic thin film capacitors [235,244,253,254], and (c) energy storage performance in different Pb-free RFE ceramics.

providing an energy storage density of the order of 8–18 J/cm^3 (Fig. 25(a)), an efficiency $\geq$ 90 %, and an excellent thermal stability (-50 to 250 ^{0}C) [220,224–226]. For instance, the nano domain engineered $BiFeO_3$-$BaTiO_3$-$NaNbO_3$ RFE bulk capacitors offers a giant $W_r \approx 8.12$ J/cm^3, a high $\eta \approx 90$ % and an excellent thermal stability (−50 to 250 °C). Furthermore, to compete with the super-capacitors, the advanced capacitors should offer high voltage in the kV range and an energy density of 15–30 J/cm^3 [35]. Currently, the RFE based films are capable of providing an energy storage density 80–159 J/cm^3 (Fig. 25(b)), an efficiency up to 90 %, and a very good thermal stability (-50 to 200 ^{0}C) [230,232,253,254]. Such a higher W_r and broader operating temperature range of RFE films are appropriate for practical application in large-sized equipment such as power converters, oil-well drilling, etc [22]. Further, the flexible RFE films can be used for the development of wearable modern electrical devices. In fact, conferring flexibility to the electronics can further enhance their applicability in the emerging internet of things fields. Thus, the fabrication of capacitors on flexible devices is essential for the next-generation energy storage devices development.

However, the electric breakdown strength of the RFE capacitors must be improved to meet the application requirements such as the operating voltage lies between 400 and 800 V [255,256]. In this context, we anticipate that by combining a MLCC approach with one that essentially improves the electric breakdown strength, such as 0–3 type composite, can be an effective way to achieve it. Furthermore, most of the studies on domain engineering and MLCCs are based on bismuth and barium-based material. It is necessary to widen the scope of the nano domain engineering and MLCC fabrications towards other materials. For instance, the fabrication techniques such as nano domain engineering and MLCC formation in KNN based RFEs might provide a new face for the development of transparent military technology. Although the RFE films possess good electric field endurance and a superior W_r, the efficiency of most of them is $<$ 76 %. To overcome such barrier, we believe instead of forming nano domains, the formation of polymorphic nano domains can be a better option to improve the efficiency as well as the energy storage density in RFE thin films. This is due to the fact that the polymorphic nano domain (optimizing the rhombohedral (R) and tetragonal (T) nano domain) structure leads to a flatter energy profile when compared to RFEs with only R or T nano domains [230]. As a result, it is possible to achieve a more flattened domain-switching pathway and thereby minimizing the hysteresis through maintaining a high polarization. In addition, we believe that by combining different strategies in a single capacitor structure, RFEs-based capacitors will be soon the best solution on the market.

Through a careful evaluation of the published works on the topic, we should also mention that most of the research works are mainly focused on the improvement of the energy storage performance of dielectric capacitors, but less attention has been paid to their PNR dynamics, charge and discharge speed, fatigue behavior, temperature stability and lifetime, which are essential from the applications point of view. Based on the sections IV-V, we made a graphical analysis of the best performed Pb-free RFE ceramics and are shown in Fig. 25(c). It is evident that there is a significant difference in the energy storage performance of these materials and this might be attributed to the PNR dynamics in these materials. Furthermore, the energy storage performance of BNT RFEs ceramics is higher compared to other Pb-free RFE ceramics. It is observed that the PNR dynamics as well as the relaxor mechanism in BNT is explored in a higher fashion compared to other Pb-free materials. Especially, the possibilities of PNR dynamics and the corresponding dielectric relaxation at various external stimuli (electric field cooling, compressed cooling) in BNT has been examined in a broader perspective than other Pb-free ceramic systems [83]. Therefore, we believe a more detailed investigation on the PNR dynamics as well as the dielectric relaxation can bring out the best energy storage performance in other Pb-free RFEs. Moreover, the energy storage density is usually obtained from dynamic method (*P-E* loops), which is usually higher than the one obtained from the static method. In fact, in the static method the frequencies used in the measurements are closer to the ones used in the applications, such as in DC bus capacitor in HEV [255,256], and therefore, we encourage the scientific community to consider the static methods for evaluating the energy storage performance, as well as the charge/discharge speed, fatigue behavior, temperature stability and lifetime, since they allow to obtain important information with a view to its application.

In conclusion, we strongly believe that RFEs are the next generation of dielectric capacitors and the most promising candidate as energy storage capacitors. We anticipate that future work on RFEs systems will consist of developing new strategies for improving energy storage and combining several ones into one single capacitor to synergistically enhance their energy storage characteristics. In this context, we strongly believe that the recently discovered ferroelectricity in binary oxide thin films may open the possibility of reducing the capacitor size to a thickness below 10 nm. In this context, the recent works about the energy storage properties of binary oxide thin films were thoroughly reviewed [257]. This is a value-added advantage for miniaturization of electronics devices, while keeping a high energy storage performance. In the end, we look forward that this article on RFEs will not only benefit the design of high-performance energy storage capacitors, but also shed light for bringing out the best RFEs for the real-world applications.

Declaration of Competing Interest

The authors declare that they have no known competing financial interests or personal relationships that could have appeared to influence the work reported in this paper.

Acknowledgement

This study has been partially supported by (i) DST-SERB, Govt. of India through Grant ECR/2017/000068 (KCS), (ii) UGC through grant nos. F.4-5(59-FRP)/ 2014(BSR) and (iii) Portuguese Foundation for Science and Technology (FCT) in the framework of the Strategic Funding UIDB/FIS/04650/2020 (JPBS). The author A. R. Jayakrishnan acknowledges the Central University of Tamil Nadu, India for his Ph. D fellowship. The authors acknowledge the CERIC-ERIC Consortium for access to experimental facilities and financial support under proposal 20192055.

References

[1] Li J, Shen Z, Chen X, Yang S, Zhou W, Wang M, et al. Grain-orientation-engineered multilayer ceramic capacitors for energy storage applications. Nat Mater 2020;19:999–1005.
[2] Gao J, Liu Y, Wang Y, Wang D, Zhong L, Ren X. High temperature-stability of $(Pb_{0.9}La_{0.1})(Zr_{0.65}Ti_{0.35})O_3$ ceramic for energy-storage applications at finite electric field strength. Scr Mater 2017;137:114–8.
[3] Yang Z, Du H, Qu S, Hou Y, Ma H, Wang J, et al. Significantly enhanced recoverable energy storage density in potassium–sodium niobate-based lead free ceramics. J Mater Chem A 2016;4:13778–85.
[4] Hao X. A review on the dielectric materials for high energy-storage application. J Adv Dielectr 2019;3:1330001.
[5] Qu B, Du H, Yang Z, Liu Q, Liu T. Enhanced dielectric breakdown strength and energy storage density in lead-free relaxor ferroelectric ceramics prepared using transition liquid phase sintering. RSC Adv 2016;6:34381–9.
[6] Jayakrishnan AR, Alex KV, Thomas A, Silva JPB, Kamakshi K, Dabra N, et al. Composition-dependent $xBa(Zr_{0.2}\ Ti_{0.8})O_3$-$(1–x)(Ba_{0.7}Ca_{0.3})TiO_3$ bulk ceramics for high energy storage applications. Ceram Int 2019;45:5808–18.
[7] Ren G, Ma G, Cong N. Review of electrical energy storage system for vehicular applications. Renew Sust Energ Rev 2015;41:225–36.
[8] Li Q, Chen J, Fan L, Kong X, Lu Y. Progress in electrolytes for rechargeable Li-based batteries and beyond. Green Energy Environ 2016;1:18–42.
[9] Kusko A, DeDad J. Stored energy-Short-term and long-term energy storage methods. IEEE Ind Appl Mag 2007;13:66–72.
[10] Yao K, Chen S, Rahimabady M, Mirshekarloo MS, Yu S, Tay FEH, et al. Nonlinear dielectric thin films for high-power electric storage with energy density comparable with electrochemical supercapacitors. IEEE Trans Ultrason Ferroelectr Freq Control 2011;58:1968–74.
[11] Sarjeant WJ, Zirnheld J, MacDougall FW. Capacitors. IEEE Trans Plasma Sci IEEE Nucl Plasma Sci Soc 1998;26:1368–92.
[12] Xu X, Gurav AS, Lessner PM, Radall CA. Robust BME class-I MLCCs for harsh-environment applications. IEEE Trans Ind Electron 2010;58:2636–43.
[13] Polotai AV, Maher SG, Wilson JM, Maher RG. Selection of dielectric materials for high temperature applications. In proceeding of CARTS USA 2010 conference, New Orleans, LA, USA 249-262.
[14] Känzig W. Ferroelectrics and antiferroeletrics. In Solid State Physics 1957;1957(4):1–197.
[15] Pan H, Ma J, Ma J, Zhang Q, Liu X, Guan B, et al. Giant energy density and high efficiency achieved in bismuth ferrite-based film capacitors via domain engineering. Nat Commun 2018;9:1–8.
[16] Mohan N, Undeland TM, Robbins WP. Power electronics: converters, applications, and design. John wiley & sons.
[17] William, J., Ultra-High Energy Density Capacitors through improved glass technology.
[18] Xu X, Liu W, Li Y, Wang Y, Yuan Q, Chen J, et al. Flexible mica films for high-temperature energy storage. J Materiomics 2018;4:173–8.
[19] Li Q, Yao FZ, Liu Y, Zhang G, Wang H, Wang Q. High-temperature dielectric materials for electrical energy storage. Annu Rev Mater Res 2018;48:219–43.
[20] Tan DQ. Review of polymer-based nanodielectric exploration and film scale-up for advanced capacitors. Adv Funct Mater 2019;1808567.
[21] Khalil G, Barshaw E, Danielson E, Chait M. Power supply and integration in future combat vehicles. Tacom research development and engineering center warren MI. 2004.
[22] Tan D, Zhang L, Chen Q, Irwin P. High-temperature capacitor polymer films. J Electron Mater 2014;43:4569–75.
[23] National Research Council. 2002. Combat hybrid power system component technologies: technical challenges and research priorities. Washington, DC: The National Academies Press. https://doi.org/10.17226/10595.
[24] Zhang GF, Liu H, Yao Z, Cao M, Hao H. Effects of Ca doping on the energy storage properties of (Sr, Ca)Ti$_O$3 paraelectric ceramics. J Mater Sci Mater Electron 2015;26:2726–32.
[25] Wang T, Jin L, Shu L, Hu Q, Wei X. Energy storage properties in $Ba_{0.4}\ Sr_{0.6}TiO_3$ ceramics with addition of semi-conductive $BaO–B_2O_3–SiO_2–Na_2CO_3–K_2CO_3$ glass. J Alloys Compd 2014;617:399–403.
[26] Wang Z, Cao M, Yao Z, Song Z, Li G, Hu W, et al. Dielectric relaxation behavior and energy storage properties in $SrTiO_3$ ceramics with trace amounts of ZrO_2 additives. Ceram Int 2014;40:14127–32.
[27] Wu J, Mahajan A, Riekehr L, Zhang H, Yang B, Meng N, et al. Perovskite $Sr_x(Bi_{1-\ x}Na_{0.\ 97\ -\ x}Li_{0.03})\ 0.5TiO_3$ ceramics with polar nano regions for high power energy storage. Nano Energy 2018;50:723–32.
[28] Zhou M, Liang R, Zhou Z, Dong X. Combining high energy efficiency and fast charge-discharge capability in novel $BaTiO_3$-based relaxor ferroelectric ceramic for energy-storage. Ceram Int 2019;45:3582–90.
[29] Liu X, Shi J, Zhu F, Du H, Li T, Liu X, et al. Ultrahigh energy density and improved discharged efficiency in bismuth sodium titanate based relaxor ferroelectrics with A-site vacancy. J Materiomics 2018;4:202–7.
[30] Wang W, Pu Y, Guo X, Shi R, Shi Y, Yang M, et al. Enhanced energy storage density and high efficiency of lead-free $Ca_{1-x}Sr_xTi_{1-y}Zr_yO_3$ linear dielectric ceramics. J Eur Ceram Soc 2019;39:5236–42.
[31] Yan F, Yang H, Ying L, Wang T. Enhanced energy storage properties of a novel lead-free ceramic with a multilayer structure. J Mater Chem C 2018;6:7905–12.
[32] Zhao P, Wang H, Wu L, Chen L, Cai Z, Li L, et al. High-performance relaxor ferroelectric materials for energy storage applications. Adv Energy Mater 2019;9:1803048.
[33] Palneedi H, Peddigari M, Hwang GT, Jeong DY, Ryu J. High-performance dielectric ceramic films for energy storage capacitors: progress and outlook. Adv Funct Mater 2018;28:1803665.
[34] Sun Z, Wang Z, Tian Y, Wang G, Wang W, Yang M, et al. Progress, outlook, and challenges in lead-free energy-storage ferroelectrics. Adv Electron Mater 2020;6:1900698.
[35] Yao Z, Song Z, Hao H, Yu Z, Cao M, Zhang S, et al. Homogeneous/inhomogeneous-structured dielectrics and their energy-storage performances. Adv Mater 2017;29:1601727.
[36] Li F, Zhai J, Shen B, Zeng H. Recent progress of ecofriendly perovskite-type dielectric ceramics for energy storage applications. J Adv Dielectr 2018;8:1830005.
[37] Yang L, Kong X, Li F, Hao H, Cheng Z, Liu H, et al. Perovskite lead-free dielectrics for energy storage applications. Prog Mater Sci 2019;102:72–108.
[38] Zou K, Dan Y, Xu H, Zhang Q, Lu Y, Huang H, et al. Recent advances in lead-free dielectric materials for energy storage. Mater Res Bull 2019;113:190–201.
[39] Chu B, Zhou X, Ren K, Neese B, Lin M, Wang Q, et al. A dielectric polymer with high electric energy density and fast discharge speed. Science 2006;313:334–6.
[40] Jain A, Panwar AK, Jha AK. Effect of ZnO doping on structural, dielectric, ferroelectric and piezoelectric properties of $BaZr_{0.1}Ti_{0.\ 9}O_3$ ceramics. Ceram Int 2017;43:1948–55.
[41] Peng B, Zhang Q, Li X, Sun T, Fan H, Ke S, et al. Giant electric energy density in epitaxial lead-free thin films with coexistence of ferroelectrics and antiferroelectrics. Adv Electron Mater 2015;1:1500052.
[42] Wang H, Liu Y, Yang T, Zhang S. Ultrahigh energy-storage density in antiferroelectric ceramics with field-induced multiphase transitions. Adv Funct Mater 2019;29:1807321.
[43] Zhang T, Li W, Zhao Y, Yu Y, Fei W. High energy storage performance of opposite double-heterojunction ferroelectricity–insulators. Adv Funct Mater 2018;28:1706211.
[44] Chen L, Sun N, Li Y, Zhang Q, Zhang L, Hao X. Multifunctional antiferroelectric MLCC with high-energy-storage properties and large field-induced strain. J Am Ceram Soc 2018;101:2313–20.
[45] Xu R, Xu Z, Feng Y, Wei X, Tian J, Huang D. Polarization of antiferroelectric ceramics for pulse capacitors under transient electric field. J Appl Phys 2016;119:224103.
[46] Zhao L, Liu Q, Gao J, Zhang S, Li JF. Lead-free antiferroelectric silver niobate tantalate with high energy storage performance. Adv Mater 2017;29:1701824.
[47] Uchino K, Zheng JH, Chen YH, Du XH, Ryu J, Gao Y, et al. Loss mechanisms and high power piezoelectrics. J Mater Sci 2006;41:217–28.
[48] Jiehui Z, Takahashi S, Yoshikawa S, Uchino K, de Vries JWC. Heat generation in multilayer piezoelectric actuators. J Am Ceram Soc 1996;9:3193–8.
[49] Liu F, Li Q, Cui J, Li Z, Yang G, Liu Y, et al. High-energy-density dielectric polymer nanocomposites with trilayered architecture. Adv Funct Mater 2017;27:1606292.

[50] Li J, Li F, Xu Z, Zhang S. Multilayer lead-free ceramic capacitors with ultrahigh energy density and efficiency. Adv Mater 2018;30:1802155.
[51] Song Z, Zhang S, Liu H, Hao H, Cao M, Li Q, et al. Improved Energy Storage Properties Accompanied by Enhanced interface polarization in annealed microwave-sintered BST. J Am Ceram Soc 2015;98:3212–22.
[52] Moulson AJ, Herbert JM, Electroceramics: Materials, Properties, Applications, 2nd Edition, Wiley publications.
[53] Liu B, Wang X, Zhang R, Li L. Grain size effect and microstructure influence on the energy storage properties of fine-grained $BaTiO_3$-based ceramics. J Am Ceram Soc 2017;100:3599–607.
[54] Dong G, Ma S, Du J, Cui J. Dielectric properties and energy storage density in ZnO-doped $Ba_{0.3}Sr_{0.7}TiO_3$ ceramics. Ceram Int 2009;35:2069–75.
[55] Yang Z, Gao F, Du H, Jin L, Yan L, Hu Q, et al. Grain size engineered lead-free ceramics with both large energy storage density and ultrahigh mechanical properties. Nano Energy 2019;58:768–77.
[56] Bian S, Yue Z, Zhang J, Li L. Enhancement of dielectric properties and energy storage performance in 3Y-TZP ceramics with $BaTiO_3$ additives. Int J Appl Ceram Technol 2020;17:1362–70.
[57] Puli VS, Pradhan DK, Chrisey DB, Tomozawa M, Sharma GL, Scott JF, et al. Structure, dielectric, ferroelectric, and energy density properties of (1–x) BZT–xBCT ceramic capacitors for energy storage applications. J Mater Sci 2013;48:2151–7.
[58] Han K, Li Q, Chanthad C, Gadinski MR, Zhang G, Wang Q. A hybrid material approach toward solution-processable dielectrics exhibiting enhanced breakdown strength and high energy density. Adv Funct Mater 2015;25:3505–13.
[59] Li WB, Zhou D, Pang LX, Xu R, Guo HH. Novel barium titanate based capacitors with high energy density and fast discharge performance. J Mater Chem A 2017;5:19607–12.
[60] Liu J, Zeng M, He Z, Li H, Yuan Y, Zhang S. High efficiency and power density relaxor ferroelectric $Sr_{0.875}Pb_{0.125}TiO_3$-$Bi(Mg_{0.5}Zr_{0.5})O_3$ ceramics for pulsed power capacitors. J Eur Ceram Soc 2020.
[61] Smolenskii GA, Isupov VA, Agranovskaya AI, Popov SN. Ferroelectrics with diffuse phase transitions. Soviet Physics-solid state 1961;2:2584–94.
[62] Cross LE. Relaxor ferroelectrics. Ferroelectrics 1987;76:241–76.
[63] Setter N, Cross LE. The role of B-site cation disorder in diffuse phase transition behavior of perovskite ferroelectrics. J Appl Phys 1980;1980(51):4356–60.
[64] Viehland D, Jang SJ, Cross LE, Wuttig M. Freezing of the polarization fluctuations in lead magnesium niobate relaxors. J Appl Phys 1990;68:2916–21.
[65] Quian H, Bursill LA. Phenomenological theory of the dielectric response of lead magnesium niobate and lead scandium tantalate. Int J Mod Phys B 1996;10:2007–25.
[66] Glazounov AE, Tagantsev AK. A "breathing" model for the polarization response of relaxor ferroelectrics. Ferroelectrics 1999;221:57–66.
[67] Cross LE. Ferroelectric materials for electromechanical transducer applications. Mater Chem Phys 1996;43:108–15.
[68] Damjanovic D. Ferroelectric, dielectric and piezoelectric properties of ferroelectric thin films and ceramics. Rep Prog Phys 1998;61:1267.
[69] Heywang W, Lubitz K, Wersing W. eds., 2008. Piezoelectricity: evolution and future of a technology (Vol. 114). Springer Science & Business Media.
[70] Bokov AA, Ye ZG. Dielectric relaxation in relaxor ferroelectrics. J Adv Dielectr 2012;2012(2):1241010.
[71] Sun E, Wenwu C. Relaxor-based ferroelectric single crystals: growth, domain engineering, characterization and applications. Prog Mater Sci 2014;65:124–210.
[72] Ahn CW, Hong CH, Choi BY, Kim HP, Han HS, Hwang Y, et al. A brief review on relaxor ferroelectrics and selected issues in lead-free relaxors. J Korean Phys Soc 2016;68:1481–94.
[73] Li F, Zhang S, Damjanovic D, Chen LQ, Shrout TR. Local structural heterogeneity and electromechanical responses of ferroelectrics: learning from relaxor ferroelectrics. Adv Funct Mater 2018;28:1801504.
[74] Bobic JD, Petrovic MMV, Stojanovic BD. Review of the most common relaxor ferroelectrics and their applications. In: Magnetic, Ferroelectric, and Multiferroic Metal Oxides. Elsevier; 2018. p. 233–49.
[75] Pradhan LK; Kar M. Relaxor Ferroelectric Oxides: Concept to Applications. *Multifunctional Ferroelectric Materials*, 2021; 49.
[76] Hong CH, Guo H, Tan X, Daniels JE, Jo W. Polarization reversal via a transient relaxor state in nonergodic relaxors near freezing temperature. J Materiomics 2019;5:634–40.
[77] Polinger V, Bersuker IB. Origin of polar nanoregions and relaxor properties of ferroelectrics. Phys Rev B 2018;98:214102.
[78] Jo W, Dittmer R, Acosta M, Zang J, Groh C, Sapper E, et al. Giant electric-field-induced strains in lead-free ceramics for actuator applications–status and perspective. J Electroceramics 2012;29:71–93.
[79] Farhi R, Marssi ME, Dellis JL, Picot JC, Morell A. On the nature of the glassy state in 9/65/35 PLZT ceramics. Ferroelectrics 1996;176:99–106.
[80] Schaab S, Granzow T. Temperature dependent switching mechanism of $(Pb_{0.92}La_{0.08})$ $(Zr_{0.65}Ti_{0.35})_O3$ investigated by small and large signal measurements. Appl Phys Lett 2010;97:132902.
[81] Bai Y, Cheng ZY, Bharti V, Xu HS, Zhang QM. High-dielectric-constant ceramic-powder polymer composites. Appl Phys Lett 2000;76:3804–6.
[82] Cheng ZY, Li Z, Ma Y, Zhang QM, Bateman FB. Evolution of property and microstructure of P (VDF-TrFE) copolymers modified by irradiation introduced defects. MRS Online Proceedings Library Archive. 2002; 734.
[83] Fan Z, Randall CA. Engineering the nature of polarization dynamics in lead-free relaxors based on $(Bi_{1/2}Na_{1/2})TiO_3$. Appl Phys Lett 2021;119:112904.
[84] Smolenskii GA, Isupov VA, Agranovskaya AI, Krainik NN. New materials of AIIBIVOVI type. Sov Phys Sol State 1960;2:2982–5.
[85] Jones GO, Thomas PA. Investigation of the structure and phase transitions in the novel A-site substituted distorted perovskite compound $Na_{0.5}Bi_{0.5}TiO_3$. Acta Crystallogr. B: Struct Sci Cryst Eng 2002;58:168–78.
[86] Wang B, Luo L, Jiang X, Li W, Chen H. Energy-storage properties of (1–x)Bi0.47Na0.47Ba0.06TiO3–xKNbO3 lead-free ceramics. J Alloys Compd 2014;585:14–8.
[87] Luo L, Wang B, Jiang X, Li W. Energy storage properties of (1–x) $(Bi_{0.5}Na_{0.5})TiO_{3-x}KNbO_3$ lead-free ceramics. J Mater Sci 2014;49:1659–65.
[88] Yao M, Pu Y, Zheng H, Zhang L, Chen M, Cui Y. Improved energy storage density in 0.475 BNT–0.525 BCTZ with MgO addition. Ceram Int 2016;42:8974–9.
[89] Li Q, Wang J, Ma Y, Ma L, Dong G, Fan H. Enhanced energy-storage performance and dielectric characterization of $0.94Bi_{0.5}Na_{0.5}TiO_3$–$0.06BaTiO_3$ modified by $CaZrO_3$. J Alloys Compd 2016;663:701–7.
[90] Zhou X, Yuan C, Li Q, Feng Q, Zhou C, Liu X, et al. Energy storage properties and electrical behavior of lead-free (1–x)$Ba_{0.04}Bi_{0.48}Na_{0.48}TiO_{3-x}SrZrO_3$ ceramics. J Mater Sci Mater Electron 2016;27:3948–56.
[91] Li QN, Zhou CR, Xu JW, Yang L, Zhang X, Zeng WD, et al. Ergodic relaxor state with high energy storage performance induced by doping $Sr_{0.85}Bi_{0.1}TiO_3$ in $Bi_{0.5}Na_{0.5}TiO_3$ Ceramics. J Electron Mater 2016;45:5146–51.
[92] Chen P, Chu B. Improvement of dielectric and energy storage properties in Bi $(Mg_{1/2}Ti_{1/2})$ O_3-modified $(Na_{1/2}Bi_{1/2})0.92Ba_{0.08}TiO_3$ ceramics. J Eur Ceram Soc 2016;36:81–8.
[93] Zhao Y, Xu J, Zhou C, Yuan C, Li Q, Chen G, et al. High energy storage properties and dielectric behavior of $(Bi_{0.5}$ $Na_{0.5})$ $_{0.9}4$ $B_{a0.0}6T_{i1-}$ x $(A_{l0.}5N_{b0.}5)x_O3$ lead-free ferroelectric ceramics. Ceram Int 2016;42:2221–6.
[94] Xu Q, Lanagan MT, Huang X, Xie J, Zhang L, Hao H, et al. Dielectric behavior and impedance spectroscopy in lead-free BNT–BT–NBN perovskite ceramics for energy storage. Ceram Int 2016;42:9728–36.
[95] Xu Q, Liu H, Zhang L, Xie J, Hao H, Cao M, et al. Structure and electrical properties of lead-free $Bi_{0.5}Na_{0.5}TiO_3$-based ceramics for energy-storage applications. RSC Adv 2016;6:59280–91.
[96] Li F, Zhai J, Shen B, Liu X, Yang K, Zhang Y, et al. Influence of structural evolution on energy storage properties in $Bi_{0.5}Na_{0.5}TiO_3$-$SrTiO_3$-$NaNbO_3$ lead-free ferroelectric ceramics. J Appl Phys 2017;121:054103.
[97] Liu Z, Ren P, Long C, Wang X, Wan Y, Zhao G. Enhanced energy storage properties of $NaNbO_3$ and $SrZrO_3$ modified $Bi_{0.5}Na_{0.5}TiO_3$ based ceramics. J Alloys Compd 2017;721:538–44.
[98] Tao CW, Geng XY, Zhang J, Wang RX, Gu ZB, Zhang ST. $Bi_{0.5}$ $Na_{0.5}TiO_3$–$BaTiO_3$–$K_{0.5}Na_{0.5}NbO_3$: ZnO relaxor ferroelectric composites with high breakdown electric field and large energy storage properties. J Eur Ceram Soc 2018;38:4946–52.
[99] Pu Y, Zhang L, Guo X, Yao M. Improved energy storage properties of $0.55Bi_{0.5}Na_{0.5}TiO_3$-$0.45Ba_{0.85}Ca_{0.15}Ti_{0.85}Zr_{0.1}Sn_{0.05}O_3$ ceramics by microwave sintering. Ceram Int 2018;44:242–5.

[100] Zhao N, Fan H, Ning L, Ma J, Zhou Y. Temperature-stable dielectric and energy storage properties of La ($Ti_{0.5}Mg_{0.5}$)O_3-doped ($Bi_{0.5}Na_{0.5}$)TiO_3-($Sr_{0.7}$ $Bi_{0.2}$)TiO_3 lead-free ceramics. J Am Ceram Soc 2018;101:5578–85.
[101] Ren P, Liu Z, Wang X, Duan Z, Wan Y, Yan F, et al. Dielectric and energy storage properties of $SrTiO_3$ and $SrZrO_3$ modified $Bi_{0.5}Na_{0.5}TiO_3$–$Sr_{0.8}Bi_{0.1}\square_{0.1}TiO_3$ based ceramics. J Alloys Compd 2018;742:683–9.
[102] Tang W, Xu Q, Liu H, Yao Z, Hao H, Cao M. High energy density dielectrics in lead-free $Bi_{0.5}Na_{0.5}TiO_3$–$NaNbO_3$–$Ba(Zr_{0.2}Ti_{0.8})O_3$ ternary system with wide operating temperature. J Mater Sci Mater Electron 2016;27:6526–34.
[103] Qiao X, Wu D, Zhang F, Niu M, Chen B, Zhao X, et al. Enhanced energy density and thermal stability in relaxor ferroelectric $Bi_{0.5}Na_{0.5}TiO_3$–$Sr_{0.7}Bi_{0.2}TiO_3$ ceramics. J Eur Ceram Soc 2019;39:4778–84.
[104] Pan Z, Hu D, Zhang Y, Liu J, Shen B, Zhai J. Achieving high discharge energy density and efficiency with NBT-based ceramics for application in capacitors. J Mater Chem C 2019;7:4072–8.
[105] Qiao X, Wu D, Zhang F, Chen B, Ren X, Liang P, et al. $Bi_{0.5}Na_{0.5}TiO_3$-based relaxor ferroelectric ceramic with large energy density and high efficiency under a moderate electric field. J Mater Chem C 2019;7:10514–20.
[106] Huang N, Liu H, Hao H, Yao Z, Cao M, Xie J. Energy storage properties of MgO-doped 0.5 $Bi_{0.5}Na_{0.5}TiO_3$-0.5$SrTiO_3$ ceramics. Ceram Int 2019;45:14921–7.
[107] Zhou X, Qi H, Yan Z, Xue G, Luo H, Zhang D. Large energy density with excellent stability in fine-grained ($Bi_{0.5}Na_{0.5}$)TiO_3-based lead-free ceramics. J Eur Ceram Soc 2019;39:4053–9.
[108] Qiao X, Zhang F, Wu D, Chen B, Zhao X, Peng Z, et al. Superior comprehensive energy storage properties in $Bi_{0.5}Na_{0.5}TiO_3$-based relaxor ferroelectric ceramics. Chem Eng J 2020;388:124158.
[109] Hu D, Pan Z, Zhang X, Ye H, He Z, Wang M, et al. Greatly enhanced discharge energy density and efficiency of novel relaxation ferroelectric BNT–BKT-based ceramics. J Mater Chem C 2020.
[110] Yan F, Huang K, Jiang T, Zhou X, Shi Y, Ge G, et al. Significantly enhanced energy storage density and efficiency of BNT-based perovskite ceramics via A-site defect engineering. Energy Storage Mater 2020.
[111] Bai W, Wang L, Zhao X, Zheng P, Wen F, Li L, et al. Tailoring frequency-insensitive large field-induced strain and energy storage properties in ($Ba_{0.85}Ca_{0.15}$)($Zr_{0.1}Ti_{0.9}$)O_3-modified ($Bi_{0.5}Na_{0.5}$)TiO_3 lead-free ceramics. Dalton Trans 2019;48:10160–73.
[112] Huang Y, Li F, Hao H, Xia F, Liu H, Zhang S. ($Bi_{0.51}Na_{0.47}$)TiO_3 based lead free ceramics with high energy density and efficiency. J Materiomics 2019;5:385–93.
[113] Hu D, Pan Z, He Z, Yang F, Zhang X, Li P, et al. Significantly improved recoverable energy density and ultrafast discharge rate of $Na_{0.5}Bi_{0.5}TiO_3$-based ceramics. Ceram Int 2020.
[114] Zhou X, Qi H, Yan Z, Xue G, Luo H, Zhang D. Superior thermal stability of high energy density and power density in domain-engineered $Bi_{0.5}Na_{0.5}TiO_3$–$NaTaO_3$ relaxor ferroelectrics. ACS Appl Mater Interfaces 2019;11:43107–15.
[115] Zannen M, Lahmar A, Kutnjak Z, Belhadi J, Khemakhem H, El Marssi M. Electrocaloric effect and energy storage in lead free $Gd_{0.02}Na_{0.5}Bi_{0.48}TiO_3$ ceramic. Solid State Sci 2017;66:31–7.
[116] Pu Y, Zhang L, Cui Y, Chen M. High energy storage density and optical transparency of microwave sintered homogeneous ($Na_{0.5}Bi_{0.5}$)$_{(1-x)}$ $Ba_xTi_{(1-y)}Sn_yO_3$ Ceramics. ACS Sustain. Chem Eng 2018;6:6102–9.
[117] Duan R, Wang J, Jiang S, Lv Y, Li J, Song A, et al. Sr^{2+} doping to enhanced energy-storage properties of ($Na_{0.5}Bi_{0.5}$)0.94$Ba_{0.06}TiO_3$ lead-free ferroelectric ceramics. J Mater Sci Mater Electron 2018;29:13952–6.
[118] Yang L, Kong X, Cheng Z, Zhang S. Ultra-high energy storage performance with mitigated polarization saturation in lead-free relaxors. J Mater Chem A 2019;7:8573–80.
[119] Zhang L, Pu X, Chen M, Bai S, Pu Y. Influence of $BaSnO_3$ additive on the energy storage properties of $Na_{0.5}Bi_{0.5}TiO_3$-based relaxor ferroelectrics. J Eur Ceram Soc 2018;38:2304–11.
[120] Sui J, Fan H, Peng H, Ma J, Yadav AK, Chao W, et al. Enhanced energy-storage performance and temperature-stable dielectric properties of (1–x) [($Na_{0.5}Bi_{0.5}$)$_{0.95}Ba_{0.0}$]0.98$La_{0.02}TiO_3$–x$K_{0.5}Na_{0.5}NbO_3$ lead-free ceramics. Ceram Int 2019;45:20427–34.
[121] Zhang L, Pu Y, Chen M. Ultra-high energy storage performance under low electric fields in $Na_{0.5}Bi_{0.5}TiO_3$-based relaxor ferroelectrics for pulse capacitor applications. Ceram Int 2020;46:98–105.
[122] Yang Z, Yuan Y, Cao L, Li E, Zhang S. Relaxor ferroelectric ($Na_{0.5}Bi$ $_{0.5}$)$_{0.4}Sr_{0.6}TiO_3$-based ceramics for energy storage application. Ceram Int 2020.
[123] Lin Y, Li D, Zhang M, Yang H. ($Na_{0.5}Bi_{0.5}$)$_{0.7}Sr_{0.3}TiO_3$ modified by Bi($Mg_{2/3}Nb_{1/3}$)O_3 ceramics with high energy-storage properties and an ultrafast discharge rate. J Mater Chem C 2020 8;:2258–64.
[124] Ma W, Fan P, Salamon D, Kongparakul S, Samart C, Zhang T, et al. Fine-grained BNT-based lead-free composite ceramics with high energy-storage density. Ceram Int 2019;45:19895–901.
[125] Wang J, Fan H, Hu B, Jiang H. Enhanced energy-storage performance and temperature-stable dielectric properties of (1–x)(0.94 $Na_{0.5}Bi_{0.5}TiO_3$–0.06$BaTiO_3$)–xNa0.73$Bi_{0.09}NbO_3$ ceramics. J Mater Sci Mater Electron 2019;30:2479–88.
[126] Li Q, Wang C, Yadav AK, Fan H. Large electrostrictive effect and energy storage density in $MnCO_3$ modified $Na_{0.325}Bi_{0.395}Sr_{0.245}\square_{0.035}TiO_3$ lead-free ceramics. Ceram Int 2020;46:3374–81.
[127] Liu G, Dong J, Zhang L, Yu L, Wei F, Li Y, et al. $Na_{0.25}Sr_{0.5}Bi_{0.25}TiO_3$ relaxor ferroelectric ceramic with greatly enhanced electric storage property by a B-site ion doping. Ceram Int 2020.
[128] Zhang L, Pu Y, Chen M. Influence of $BaZrO_3$ additive on the energy-storage properties of 0.775$Na_{0.5}Bi_{0.5}TiO_3$-0.225$BaSnO_3$ relaxor ferroelectrics. J Alloys Compd 2019;775:342–7.
[129] Zhou M, Liang R, Zhou Z, Dong X. Achieving ultrahigh energy storage density and energy efficiency simultaneously in sodium niobate-based lead-free dielectric capacitors via microstructure modulation. Inorg Chem Front 2019;6:2148–57.
[130] Zhang L, Pu Y, Chen M, Wei T, Peng X. Novel $Na_{0.5}Bi_{0.5}Ti_{0.5}O_3$ based, lead-free energy storage ceramics with high power and energy density and excellent high-temperature stability. Chem Eng J 2020;383:123154.
[131] Zhang L, Pu Y, Chen M, Wei T, Keipper W, Shi R, et al. High energy-storage density under low electric fields and improved optical transparency in novel sodium bismuth titanate-based lead-free ceramics. J Eur Ceram Soc 2020;40:71–7.
[132] Liu B, Wang X, Zhao Q, Li L. Improved energy storage properties of fine-crystalline $BaTiO_3$ ceramics by coating powders with Al_2O_3 and SiO_2. J Am Ceram Soc 2015;98:2641–6.
[133] Huang YH, Wu YJ, Qiu WJ, Li J, Chen XM. Enhanced energy storage density of $Ba_{0.4}Sr_{0.6}TiO_3$–MgO composite prepared by spark plasma sintering. J Eur Ceram Soc 2015;35:1469–76.
[134] Zhou L, Vilarinho PM, Baptista JL. Dependence of the structural and dielectric properties of $Ba_{1-x}Sr_xTiO_3$ ceramic solid solutions on raw material processing. J Eur Ceram Soc 1999;19:2015–20.
[135] Shen Z, Wang X, Luo B, Li L. $BaTiO_3$–$BiYbO_3$ perovskite materials for energy storage applications. J Mater Chem A 2015;3:18146–53.
[136] Hu Q, Jin L, Wang T, Li C, Xing Z, Wei X. Dielectric and temperature stable energy storage properties of 0.88$BaTiO_3$–0.12Bi($Mg_{1/2}Ti_{1/2}$)O_3 bulk ceramics. J Alloys Compd 2015;640:416–20.
[137] Wang T, Jin L, Li C, Hu Q, Wei X. Relaxor ferroelectric $BaTiO_3$–Bi ($Mg_{2/3}Nb_{1/3}$)O_3 ceramics for energy storage application. J Am Ceram Soc 2015;98:559–66.
[138] Wu L, Wang X, Li L. Lead-free $BaTiO_3$–Bi($Zn_{2/3}Nb_{1/3}$)O_3 weakly coupled relaxor ferroelectric materials for energy storage. RSC Adv 2016;6:14273–82.
[139] Yuan Q, Yao F, Wang Y, Ma R, Wang H. Relaxor ferroelectric 0.9$BaTiO_3$–0.1Bi($Zn_{0.5}Zr_{0.5}$)O_3 ceramic capacitors with high energy density and temperature stable energy storage properties. J Mater Chem C 2017;5:9552–8.
[140] Yuan Q, Li G, Yao FZ, Cheng SD, Wang Y, Ma R, et al. Simultaneously achieved temperature-insensitive high energy density and efficiency in domain engineered $BaTiO_3$-Bi($Mg_{0.5}Zr_{0.5}$)O_3 lead-free relaxor ferroelectrics. Nano Energy 2018;52:203–10.
[141] Zhou M, Liang R, Zhou Z, Dong X. Novel $BaTiO_3$-based lead-free ceramic capacitors featuring high energy storage density, high power density, and excellent stability. J Mater Chem C 2018;6:8528–37.

[142] Huang J, Zhang J, Yu H, Wei M, Chen H, Yang C. Improvement of dielectric and energy storage properties in $BaTiO_3$ ceramics with $BiNbO_4$ modified. Ferroelectrics 2017;510:8–15.
[143] Li WB, Zhou D, Xu R, Pang LX, Reaney IM. $BaTiO_3$–Bi $(Li_{0.5}Ta_{0.5})O_3$, Lead-Free Ceramics, and Multilayers with High Energy Storage Density and Efficiency. ACS Appl Energy Mater 2018;1:5016–23.
[144] Si F, Tang B, Fang Z, Li H, Zhang S. Enhanced energy storage and fast charge-discharge properties of (1–x)$BaTiO_3$-xBi$(Ni_{½}Sn_{1/2})O_3$ relaxor ferroelectric ceramics. Ceram Int 2019;45:17580–90.
[145] Si F, Tang B, Fang Z, Zhang S. Structural and dielectric relaxor properties of (1–x)$BaTiO_3$–xBi$(Zn_{1/2}Zr_{1/2})O_3$ ceramics for energy storage applications. J Mater Sci Mater Electron 2019;30:2772–82.
[146] Jiang X, Hao H, Zhang S, Lv J, Cao M, Yao Z, et al. Enhanced energy storage and fast discharge properties of BaTiO3 based ceramics modified by Bi$(Mg_{½}Zr_{1/2})O_3$. J Eur Ceram Soc 2019;39:1103–9.
[147] Si F, Tang B, Fang Z, Li H, Zhang S. A new type of $BaTiO_3$-based ceramics with Bi$(Mg_{1/2}Sn_{1/2})O_3$ modification showing improved energy storage properties and pulsed discharging performances. J Alloys Compd 2020;819:153004.
[148] Li X, Chen X, Sun J, Zhou M, Zhou H. Novel lead-free ceramic capacitors with high energy density and fast discharge performance. Ceram Int 2020;46:3426–32.
[149] Hu Q, Tian Y, Zhu Q, Bian J, Jin L, Du H, et al. Achieve ultrahigh energy storage performance in $BaTiO_3$–Bi $(Mg_{½}Ti_{½})O_3$ relaxor ferroelectric ceramics via nano-scale polarization mismatch and reconstruction. Nano Energy 2020;67:104264.
[150] Dong X, Chen H, Wei M, Wu K, Zhang J. Structure, dielectric and energy storage properties of $BaTiO_3$ ceramics doped with $YNbO_4$. J Alloys Compd 2018;744:721–7.
[151] Lin Y, Li D, Zhang M, Zhan S, Yang Y, Yang H, et al. Excellent energy-storage properties achieved in $BaTiO_3$-based Lead-free relaxor ferroelectric ceramics via domain engineering on the nanoscale. ACS Appl Mater Interfaces 2019;11:36824–30.
[152] Liu G, Li Y, Gao J, Li D, Yu L, Dong J, et al. Structure evolution, ferroelectric properties, and energy storage performance of $CaSnO_3$ modified $BaTiO_3$-based Pb-free ceramics. J Alloys Compd 2020;826:154160.
[153] Huang Y, Zhao C, Wu B, Wu J. Multifunctional BaTiO3-based relaxor ferroelectrics toward excellent energy storage performance and electrostrictive strain benefiting from crossover region. ACS Appl Mater Interfaces 2020.
[154] Li F, Zhou M, Zhai J, Shen B, Zeng H. Novel barium titanate based ferroelectric relaxor ceramics with superior charge-discharge performance. J Eur Ceram Soc 2018;38:4646–52.
[155] Chen X, Li X, Sun J, Sun C, Shi J, Pang F, et al. Simultaneously achieving ultrahigh energy storage density and energy efficiency in barium titanate based ceramics. Ceram Int 2020;46:2764–71.
[156] Chen X, Li X, Sun J, Sun C, Shi J, Pang F, et al. Achieving ultrahigh energy storage density and energy efficiency simultaneously in barium titanate based ceramics. Appl Phys A 2020;126:146.
[157] Li F, Kwok KW. $K_{0.5}Na_{0.5}NbO_3$-Based Lead-Free Transparent electro-optic ceramics prepared by pressureless sintering. J Am Ceram Soc 2013;96:3557–62.
[158] Qu B, Du H, Yang Z. Lead-free relaxor ferroelectric ceramics with high optical transparency and energy storage ability. J Mater Chem C 2016;4:1795–803.
[159] Du H, Zhou W, Luo F, Zhu D, Qu S, Li Y, et al. Design and electrical properties' investigation of $(K_{0.5}Na_{0.5})NbO_3$–$BiMeO_3$ lead-free piezoelectric ceramics. J Appl Phys 2008;104:034104.
[160] Kosec M, Bobnar V, Hrovat M, Bernard J, Malic B, Holc J. New lead-free relaxors based on the $K_{0.5}Na_{0.5}NbO_3$–$SrTiO_3$ solid solution. J Mater Res 2004;19:1849–54.
[161] Cheng H, Zhou W, Du H, Luo F, Zhu D, Jiang D, et al. Enhanced dielectric relaxor properties in (1–x) $(_{K0.}5N_{a0.}5)Nb_O3$–x $(B_{a0.}6S_{r0.}4)$ $0.7B_{i0.}2Ti_O3$ lead-free ceramic. J Alloys Compd 2013;579:192–7.
[162] Qiao X, Zhang X, Wu D, Chao X, Yang Z. Influence of Bi nonstoichiometry on the energy storage properties of 0.93KNN–0.07Bi_xMN relaxor ferroelectrics. J Adv Dielectr 2018;8:1830006.
[163] Chai Q, Yang D, Zhao X, Chao X, Yang Z. Lead-free (K, Na) NbO_3-based ceramics with high optical transparency and large energy storage ability. J Am Ceram Soc 2018;101:2321–9.
[164] Zhang M, Yang H, Li D, Lin Y. Excellent energy density and power density achieved in $K_{0.5}Na_{0.5}NbO_3$-based ceramics with high optical transparency. J Alloys Compd 2020:154565.
[165] Chen B, Tian Y, Lu J, Wu D, Qiao X, Liang P, Du H, Peng Z, Ren X, Chao X, Yng, Z. Ultrahigh storage density achieved with (1-x)KNN-xBZN ceramics. J. Eur. Ceram. Soc. 2020.
[166] Li Y, Zhen Y, Wang W, Fang Z, Jia Z, Zhang J, et al. Enhanced energy storage density and discharge efficiency in potassium sodium niobite-based ceramics prepared using a new scheme. Soc: J. Eur. Ceram; 2020.
[167] Hu QG, Shen ZY, Li YM, Wang ZM, Luo WQ, Xie ZX. Enhanced energy storage properties of dysprosium doped strontium titanate ceramics. Ceram Int 2014;40:2529–34.
[168] Yang H, Yan F, Lin Y, Wang T, He L, Wang F. A lead free relaxation and high energy storage efficiency ceramics for energy storage applications. J Alloys Compd 2017;710.
[169] Yan F, Yang H, Lin Y, Wang T. Dielectric and ferroelectric properties of $SrTiO_3$–$Bi_{0.5}Na_{0.5}TiO_3$–$BaAl_{0.5}Nb_{0.5}O_3$ lead-free ceramics for high-energy-storage applications. Inorg Chem 2017;56:13510–6.
[170] Yang H, Yan F, Lin Y, Wang T. Improvement of dielectric and energy storage properties in $SrTiO_3$-based lead-free ceramics. J Alloys Compd 2017;728:780–7.
[171] Yang H, Yan F, Lin Y, Wang T. Novel strontium titanate-based lead-free ceramics for high-energy storage applications. ACS Sustain Chem Eng 2017;5:10215–22.
[172] Yang H, Yan F, Lin Y, Wang T. Enhanced recoverable energy storage density and high efficiency of $SrTiO_3$-based lead-free ceramics. Appl Phys Lett 2017;111:253903.
[173] Cui C, Pu Y, Gao Z, Wan J, Guo Y, Hui C, et al. Structure, dielectric and relaxor properties in lead-free ST-NBT ceramics for high energy storage applications. J Alloys Compd 2017;711:319–26.
[174] Jan A, Liu H, Hao H, Yao Z, Emmanuel M, Pan W, et al. Enhanced dielectric breakdown strength and ultra-fast discharge performance of novel $SrTiO_3$ based ceramics system. J Alloys Compd 2020;154611.
[175] Wang B, Pu Y, Yuan Q, Cui C, Shen G. Improvements of microstructures and energy storage properties of $Sr_{0.8}(Na_{0.5}Bi_{0.5})_{0.2}TiO_3$ ceramics via microwave sintering. J Mater Sci Mater Electron 2019;30:12950–5.
[176] Zhao P, Tang B, Si F, Yang C, Li H, Zhang S. Novel Ca doped $Sr_{0.7}$ $Bi_{0.2}TiO_3$ Lead-Free Relaxor Ferroelectrics with High Energy Density and Efficiency. J Eur Ceram Soc 2020;5:1938–46.
[177] Zhang, L., Wang, Z., Li, Y., Chen, P., Cai, J., Yan, Y., Zhou, Y., Wang, D. and Liu, G., 2019. Enhanced energy storage performance in Sn doped $Sr_{0.6}(Na_{0.5}Bi_{0.5})$ $0.4TiO_3$ lead-free relaxor ferroelectric ceramics. J. Eur. Ceram. Soc. 2020; 39; 3057-3063.
[178] Kong X, Yang L, Cheng Z, Zhang S. Bi-modified $SrTiO_3$-based ceramics for high-temperature energy storage applications. J Am Ceram Soc 2020;103:1722–31.
[179] Kong X, Yang L, Cheng Z, Zhang S. Ultrahigh energy storage properties in $(Sr_{0.7}Bi_{0.2})TiO_3$-Bi$(Mg_{0.5}Zr_{0.5})O_3$ lead-free ceramics and potential for high-temperature capacitors. Materials 2020;13:180.
[180] Liu N, Liang R, Zhao X, Zhang Y, Zhou Z, Tang X, et al. Tailoring domain structure through manganese to modify the ferroelectricity, strain and magnetic properties of lead-free $BiFeO_3$-based multiferroic ceramics. J Alloys Compd 2018;740:470–6.
[181] Liu N, Liang R, Liu Z, Zhou Z, Xu C, Wang G, et al. Large remanent polarization and enhanced magnetic properties in non-quenched Bi(Fe, Ga)O3-(Ba, Ca)(Zr, Ti)O3 multiferroic ceramics. Appl Phys Lett 2017;110:112902.
[182] Liu N, Liang R, Zhou Z, Dong X. Designing lead-free bismuth ferrite-based ceramics learning from relaxor ferroelectric behavior for simultaneous high energy density and efficiency under low electric field. J Mater Chem C 2018;6:10211–7.

[183] Zheng D, Zuo R, Zhang D, Li Y. Novel $BiFeO_3$–$BaTiO_3$–Ba $(Mg_{1/3}Nb_{2/3})O_3$ lead-free relaxor ferroelectric ceramics for energy-storage capacitors. J Am Ceram Soc 2015;98:2692–5.
[184] Zheng D, Zuo R. Enhanced energy storage properties in La (Mg1/2Ti1/2) O3-modified $BiFeO_3$-$BaTiO_3$ lead-free relaxor ferroelectric ceramics within a wide temperature range. J Eur Ceram Soc 2017;37:413–8.
[185] Liu N, Liang R, Zhao X, Xu C, Zhou Z, Dong X. Novel bismuth ferrite-based lead-free ceramics with high energy and power density. J Am Ceram Soc 2018;101: 3259–65.
[186] Chen Z, Bai X, Wang H, Du J, Bai W, Li L, et al. Achieving high-energy storage performance in 0.67 Bi1-xSmxFeO3-0.33 BaTiO3 lead-free relaxor ferroelectric ceramics. Ceram Int 2020;46:11549–55.
[187] Li F, Zhai J, Shen B, Zeng H, Jian X, Lu S. Multifunctionality of lead-free BiFeO3-based ergodic relaxor ferroelectric ceramics: High energy storage performance and electrocaloric effect. J Alloys Compd 2019;803:185–92.
[188] Sun H, Wang X, Sun Q, Zhang X, Ma Z, Guo M, Sun B, Zhu X, Liu Q, Lou X. Large energy storage density in $BiFeO_3$-$BaTiO_3$-$AgNbO_3$ lead-free relaxor ceramics. J. Eur. Ceram. Soc. 2020.
[189] Dabas S, Kumar M, Chaudhary P, Thakur OP. Enhanced magneto-electric coupling and energy storage analysis in Mn-modified lead free $BiFeO_3$-$BaTiO_3$ solid solutions. J Appl Phys 2019;126:134102.
[190] Chen Z, Bai X, Wang H, Du J, Bai W, Li L, et al. Achieving high-energy storage performance in $0.67Bi_{1-x}Sm_xFeO_3$-$0.33BaTiO_3$ lead-free relaxor ferroelectric ceramics. Ceram Int 2020.
[191] Yang H, Qi H, Zuo R. Enhanced breakdown strength and energy storage density in a new $BiFeO_3$-based ternary lead-free relaxor ferroelectric ceramic. J Eur Ceram Soc 2019;39:2673–9.
[192] Fan Y, Zhou Z, Liang R, Dong X. Designing novel lead-free $NaNbO_3$-based ceramic with superior comprehensive energy storage and discharge properties for dielectric capacitor applications via relaxor strategy. J Eur Ceram Soc 2019;39:4770–7.
[193] Lai D, Yao Z, You W, Gao B, Guo Q, Lu P, et al. Modulating the energy storage performance of $NaNbO_3$-based lead-free ceramics for pulsed power capacitors. Ceram Int 2020;9:13511–6.
[194] Chen X, Li X, Zhou H, Sun J, Li X, Yan X, et al. Simultaneously achieved high energy density and excellent thermal stability of lead-free barium titanate-based relaxor ferroelectric under low electric field. J Mater Sci Mater Electron 2019;30:15912–22.
[195] Li D, Lin Y, Zhang M, Yang H. Achieved ultrahigh energy storage properties and outstanding charge–discharge performances in $(Na_{0.5}Bi_{0.5})_{0.7}Sr_{0.3}TiO_3$-based ceramics by introducing a linear additive. Chem Eng J 2019:123729.
[196] Zhou M, Liang R, Zhou Z, Dong X. Developing a novel high performance $NaNbO_3$-based lead-free dielectric capacitor for energy storage applications. Sustain Energy Fuels 2020;4:1225–33.
[197] Shi R, Pu Y, Wang W, Guo X, Li J, Yang M, et al. A novel lead-free $NaNbO_3$–$Bi(Zn_{0.5}Ti_{0.5})O_3$ ceramics system for energy storage application with excellent stability. J Alloys Compd 2020:815 152356.
[198] Liu G, Li Y, Wang Z, Zhang L, Chen P, Wei F, et al. Dielectric, ferroelectric and energy storage properties of lead-free $(1–x)Ba_{0.9}Sr_{0.1}TiO_3$-$xBi(Zn_{0.5}Zr_{0.5})O_3$ ferroelectric ceramics sintered at lower temperature. Ceram Int 2019;45:15556–65.
[199] Silva JPB, Queirós EC, Tavares PB, Sekhar KC, Kamakshi K, Moreira JA, et al. Ferroelectric phase transitions studies in $0.5Ba(Zr_{0.2}Ti_{0.8})O_3$–$0.5(Ba_{0.7}Ca_{0.3})TiO_3$ ceramics. J Electroceramics 2015;35:135–40.
[200] Jayakrishnan AR, Alex KV, Kamakshi K, Silva JPB, Sekhar KC, Gomes MJM. Enhancing the dielectric relaxor behavior and energy storage properties of $0.6Ba(Zr_{0.2}Ti_{0.8})O_3$–$0.4(Ba_{0.7}Ca_{0.3})TiO_3$ ceramics through the incorporation of paraelectric $SrTiO_3$. J Mater Sci Mater Electron 2019;30:19374–82.
[201] Guo J, Berbano SS, Guo H, Baker AL, Lanagan MT, Randall CA. Cold sintering process of composites: bridging the processing temperature gap of ceramic and polymer materials. Adv Funct Mater 2016;26:7115–21.
[202] Yan F, Zhou X, He X, Bai H, Wu S, Shen B, et al. Superior energy storage properties and excellent stability achieved in environment-friendly ferroelectrics via composition design strategy. Nano Energy 2020;105012.
[203] Huang Y, Zhao C, Wu B, Wu J. Multifunctional $BaTiO_3$-based relaxor ferroelectrics toward excellent energy storage performance and electrostrictive strain benefiting from crossover region. ACS Appl Mater Interfaces 2020;12:23885–95.
[204] Zhao P, Fang Z, Zhang X, Chen J, Shen Y, Zhang X, An Q, Yang C, Gao X, Zhang S, Tang B. Aliovalent doping engineering for A-and B-sites with multiple regulatory mechanisms: a strategy to improve energy storage properties of $Sr_{0.7}Bi_{0.2}TiO_3$-based lead-free relaxor ferroelectric ceramics. ACS Appl. Mater. Interfaces; 13; 24833-24855.
[205] Wang K, Yao FZ, Jo W, Gobeljic D, Shvartsman VV, Lupascu DC, et al. Temperature-insensitive (K, Na) NbO_3-based lead-free piezoactuator ceramics. Adv Funct Mater 2013;23:4079–86.
[206] Ziebert C, Schmitt H, Krüger JK, Sternberg A, Ehses KH. Grain-size-induced relaxor properties in nanocrystalline perovskite films. Phys Rev B 2004;69:214106.
[207] Jayakrishnan AR, Yadav PVK, Silva JPB, Sekhar KC. Microstructure tailoring for enhancing the energy storage performance of $0.98[0.6Ba(Zr_{0.2}Ti_{0.8})O_3$–$0.4(Ba_{0.7}Ca_{0.3})TiO_3]$-0.02 $BiZn_{½}Ti_{½}O3$ ceramic capacitors. J Sci: Adv Mater Devices 2020;5:119–24.
[208] Binesh B, Aghaie-Khafri M. RUE-based semi-solid processing: Microstructure evolution and effective parameters. Mater Des 2016;95:268–86.
[209] Nie S, Gao B, Wang X, Cao Z, Guo E, Wang T. The influence of holding time on the microstructure evolution of Mg–10Zn–6.8 Gd–4Y alloy during semi-solid isothermal heat treatment. Metals 2019;9:420.
[210] Liu Z, Zhang A, Xu S, Lu J, Xie B, Guo K, et al. Mediating the confliction of polarizability and breakdown electric-field strength in BNST relaxor ferroelectric for energy storage applications. J Alloys Compd 2020;153772.
[211] Tao CW, Geng XY, Zhang J, Wang RX, Gu ZB, Zhang ST. $Bi_{0.5}$ $Na_{0.5}TiO_3$-$BaTiO_3$-$K_{0.5}Na_{0.5}NbO_3$: ZnO relaxor ferroelectric composites with high breakdown electric field and large energy storage properties. J Eur Ceram Soc 2018;38:4946–52.
[212] Zhang J, Pan Z, Guo FF, Liu WC, Ning H, Chen YB, et al. Semiconductor/relaxor 0–3 type composites without thermal depolarization in $Bi_{0.5}Na_{0.5}TiO_3$-based lead-free piezoceramics. Nat Commun 2015;6:1–10.
[213] Li F, Hou X, Wang J, Zeng H, Shen B, Zhai J. Structure-design strategy of 0–3 type $(Bi_{0.32}Sr_{0.42}Na_{0.20})TiO_3$/MgO composite to boost energy storage density, efficiency and charge-discharge performance. J Eur Ceram Soc 2019;39:2889–98.
[214] Jayakrishnan AR, Silva JPB, Kamakshi K, Annapureddy V, Mercioniu IF, Sekhar KC. Semiconductor/relaxor 0–3 type composites as a novel strategy for energy storage capacitors. J Sci: Adv Mater Devices 2020.
[215] Shi J, Chen X, Li X, Sun J, Sun C, Pang F, et al. Realizing ultrahigh recoverable energy density and superior charge–discharge performance in $NaNbO_3$-based lead-free ceramics via a local random field strategy. J Mater Chem C 2020;8:3784–94.
[216] Liu G, Fan H, Xu J, Liu Z, Zhao Y. Colossal permittivity and impedance analysis of niobium and aluminum co-doped TiO_2 ceramics. Rsc Adv 2016;6:48708–14.
[217] Qi H, Xie A, Tian A, Zuo R. Superior energy-storage capacitors with simultaneously giant energy density and efficiency using nanodomain engineered $BiFeO_3$-$BaTiO_3$-$NaNbO_3$ lead-free bulk ferroelectrics. Adv Energy Mater 2020;10:1903338.
[218] Cai Z, Zhu C, Wang H, Zhao P, Yu Y, Li L, et al. Giant dielectric breakdown strength together with ultrahigh energy density in ferroelectric bulk ceramics via layer-by-layer engineering. J Mater Chem A 2019;7:17283–91.
[219] Sun Z, Ma C, Liu M, Cui J, Lu L, Lu J, et al. Ultrahigh energy storage performance of lead-free oxide multilayer film capacitors via interface engineering. Adv Mater 2017;29:1604427.
[220] Wang D, Fan Z, Zhou D, Khesro A, Murakami S, Feteira A, et al. Bismuth ferrite-based lead-free ceramics and multilayers with high recoverable energy density. J Mater Chem A 2018;6:4133–44.
[221] Wang G, Li J, Zhang X, Fan Z, Yang F, Feteira A, et al. Ultrahigh energy storage density lead-free multilayers by controlled electrical homogeneity. Energy Environ Sci 2019;12:582–8.
[222] Murakami S, Wang D, Mostaed A, Khesro A, Feteira A, Sinclair DC, et al. High strain (0.4%) $Bi(Mg_{2/3}Nb_{1/3})O_3$-$BaTiO_3$-$BiFeO_3$ lead-free piezoelectric ceramics and multilayers. J Am Ceram Soc 2018;101:5428–42.
[223] Cumming DJ, Sebastian T, Sterianou I, Rödel J, Reaney IM. Bi (Me) O_3–$PbTiO_3$ high TC piezoelectric multilayers. Mater Technol 2013;28:247–53.

[224] Cai Z, Zhu C, Wang H, Zhao P, Chen L, Li L, et al. High-temperature lead-free multilayer ceramic capacitors with ultrahigh energy density and efficiency fabricated via two-step sintering. J Mater Chem A 2019;7:14575–82.

[225] Wang H, Zhao P, Chen L, Wang X. Effects of dielectric thickness on energy storage properties of $0.87BaTiO_3$-$0.13Bi(Zn_{2/3}(Nb_{0.85}Ta_{0.15})_{1/3})O_3$ multilayer ceramic capacitors. J Eur Ceram Soc 2020;40:1902–8.

[226] Ji H, Wang D, Bao W, Lu Z, Wang G, Yang H, et al. Ultrahigh energy density in short-range tilted NBT-based lead-free multilayer ceramic capacitors by nanodomain percolation. Energy Storage Mater 2021;38:113–20.

[227] Feng JX, Ye SH, Wang AL, Lu XF, Tong YX, Li GR. Flexible cellulose paper-based asymmetrical thin film supercapacitors with high-performance for electrochemical energy storage. Adv Funct Mater 2014;24:7093–101.

[228] Zhao J, Xu S, Tschulik K, Compton RG, Wei M, O'Hare D, et al. Molecular-scale hybridization of clay monolayers and conducting polymer for thin-film supercapacitors. Adv Funct Mater 2015;25:2745–53.

[229] Zhang WY, Ye Q, Fu DW, Xiong RG. Optoelectronic duple bistable switches: A bulk molecular single crystal and unidirectional ultraflexible thin film based on imidazolium fluorochromate. Adv Funct Mater 2017;27:1603945.

[230] Pan H, Li F, Liu Y, Zhang Q, Wang M, Lan S, et al. Ultrahigh–energy density lead-free dielectric films via polymorphic nanodomain design. Science 2019;365:578–82.

[231] Silva JP, Silva JM, Oliveira MJ, Weingärtner T, Sekhar KC, Pereira M, et al. High-performance ferroelectric–dielectric multilayered thin films for energy storage capacitors. Adv Funct Mater 2019;29:1807196.

[232] Lv P, Yang C, Qian J, Wu H, Huang S, Cheng X, et al. Flexible lead-free Perovskite oxide multilayer film capacitor based on $(Na_{0.8}K_{0.2})_{0.5}Bi_{0.5}TiO_3$/$Ba_{0.5}Sr_{0.5}(Ti_{0.97}Mn_{0.03})O_3$ for High-Performance Dielectric Energy Storage. Adv Energy Mater 2020;10:1904229.

[233] Sun N, Li Y, Zhang Q, Hao X. Giant energy-storage density and high efficiency achieved in $(Bi_{0.5}Na_{0.5})TiO_3$–$Bi(Ni_{0.5}Zr_{0.5})O_3$ thick films with polar nanoregions. J Mater Chem C 2018;6:10693–703.

[234] Yang C, Lv P, Qian J, Han Y, Ouyang J, Lin X, et al. Fatigue-free and bending-endurable flexible Mn-doped $Na_{0.5}Bi_{0.5}TiO_3$-$BaTiO_3$-$BiFeO_3$ film capacitor with an ultrahigh energy storage performance. Adv Energy Mater 2019;9:1803949.

[235] Yang C, Qian J, Han Y, Lv P, Huang S, Cheng X, et al. Design of an all-inorganic flexible $Na_{0.5}Bi_{0.5}TiO_3$-based film capacitor with giant and stable energy storage performance. J Mater Chem A 2019;7:22366–76.

[236] Liang Z, Ma C, Shen L, Lu L, Lu X, Lou X, et al. Flexible lead-free oxide film capacitors with ultrahigh energy storage performances in extremely wide operating temperature. Nano Energy 2019;57:519–27.

[237] Liang Z, Liu M, Shen L, Lu L, Ma C, Lu X, et al. All-inorganic flexible embedded thin-film capacitors for dielectric energy storage with high performance. ACS Appl Mater Interfaces 2019;11:5247–55.

[238] Song B, Wu S, Li F, Chen P, Shen B, Zhai J. Excellent energy storage density and charge–discharge performance of a novel $Bi_{0.2}Sr_{0.7}TiO_3$–$BiFeO_3$ thin film. J Mater Chem C 2019;7:10891–900.

[239] Kursumovic A, Li WW, Cho S, Curran PJ, Tjhe DHL, MacManus-Driscoll JL. Lead-free relaxor thin films with huge energy density and low loss for high temperature applications. Nano Energy 2020;71:104536.

[240] Sun N, Li Y, Liu X, Hao X. High energy-storage density under low electric field in lead-free relaxor ferroelectric film based on synergistic effect of multiple polar structures. J Power Sources 2020;448:227457.

[241] Fan Y, Zhou Z, Chen Y, Huang W, Dong X. A novel lead-free and high-performance barium strontium titanate-based thin film capacitor with ultrahigh energy storage density and giant power density. J Mater Chem C 2020;8:50–7.

[242] Yang C, Qian J, Lv P, Wu H, Lin X, Wang K, et al. Flexible lead-free BFO-based dielectric capacitor with large energy density, superior thermal stability, and reliable bending endurance. J Materiomics 2020;6:200–8.

[243] Qian J, Han Y, Yang C, Lv P, Zhang X, Feng C, et al. Energy storage performance of flexible NKBT/NKBT-ST multilayer film capacitor by interface engineering. Nano Energy 2020;104862.

[244] Chen J, Tang Z, Yang B, Zhao S. Ultra-high energy storage performances regulated by depletion region engineering sensitive to the electric field in PNP-type relaxor ferroelectric heterostructural films. J Mater Chem A 2020;8:8010–9.

[245] Yang C, Han Y, Feng C, Lin X, Huang S, Cheng X, et al. Toward multifunctional electronics: flexible NBT-based film with a large electrocaloric effect and high energy storage property. ACS Appl Mater Interfaces 2020;12:6082–9.

[246] Yang X, Li W, Zhang Y, Qiao Y, Yang Y, Fei W. High energy storage density achieved in Bi3+-Li+ co-doped $SrTi_{0.99}Mn_{0.01}O_3$ thin film via ionic pair doping-engineering. J Eur Ceram Soc 2020;40:706–11.

[247] Sun Y, Zhang L, Wang H, Guo M, Lou X, Wang D. Composition-driven inverse-to-conventional transformation of electrocaloric effect and large energy storage density in strontium modified $Ba(Zr_{0.1}Ti_{0.9})O_3$ thin films. J Mater Chem C 2020;8:1366–73.

[248] Tian X, Zhou K, Song L, Huang Y, Nie Z, Chen T. The role of PN-like junction effects in the energy storage performances for Ag_2O nanoparticles dispersed lead-free $K_{0.5}Na_{0.5}NbO_3$–$BiMnO_3$ films. Nanoscale 2020;12:7399–415.

[249] Hu T, Ma C, Dai Y, Fan Q, Liu M, Jia C. Enhanced Energy Storage Performance of Lead-Free Capacitor in Ultra-widen Temperature range via Engineering Paraferroelectric and Relaxor Ferroelectric Multilayer Film, ACS Appl. Mater Interfaces 2020.

[250] Silva JPB, Silva JMB, Sekhar KC, Palneedi H, Istrate MC, Negrea RF, et al. Energy storage performance of ferroelectric ZrO_2 film capacitors: effect of HfO_2:Al_2O_3 dielectric insert layer. J Mater Chem A 2020;8:14171–7.

[251] Park MH, Kim HJ, Kim YJ, Moon T, Kim KD, Hwang CS. Thin $Hf_xZr_{1-x}O_2$ films: a new lead-free system for electrostatic supercapacitors with large energy storage density and robust thermal stability. Adv Energy Mater 2014;4:1400610.

[252] Kozodaev MG, Chernikova AG, Khakimov RR, Park MH, Markeev AM, Hwang CS. La-doped $Hf_{0.5}Zr_{0.5}O_2$ thin films for high-efficiency electrostatic supercapacitors. Appl Phys Lett 2018;113:123902.

[253] Kun W, Ouyang J, Wuttig M, Zhao Y, Cheng H, Zhang Y, et al. Xiangli Zhong, Fei Zeng. Superparaelectric $(Ba_{0.95}, Sr_{0.05})(Zr_{0.2}, Ti_{0.8})O_3$ ultracapacitors. Adv Energy Mater 2020;10:2001778.

[254] Hao P, Lan S, Xu S, Zhang Q, Yao H, Liu Y, et al. Ultrahigh energy storage in superparaelectric relaxor ferroelectrics. Science 2021;374:100–4.

[255] Hava AM, Ayhan U, Aban VV, September. A DC bus capacitor design method for various inverter applications. In *2012 IEEE Energy Conversion Congress and Exposition (ECCE)*. 2012; 4592-4599.

[256] Stewart J, Neely J, Delhotal J, Flicker J. DC link bus design for high frequency, high temperature converters. IEEE Applied Power Electronics Conference and Exposition 2017:809–15.

[257] Silva JP, Sekhar KC, Pan H, MacManus-Driscoll JL, Pereira M. Advances in dielectric thin films for energy storage applications, revealing the promise of group IV binary oxides. ACS Energy Lett 2021;6:2208–17.